

# Model-based Design Development and Control of a Wind Resistant Multirotor UAV

Christian Månsson  
Daniel Stenberg



**LUNDS**  
UNIVERSITET

Department of Automatic Control

MSc Thesis  
ISRN LUTFD2/TFRT--5947--SE  
ISSN 0280-5316

Department of Automatic Control  
Lund University  
Box 118  
SE-221 00 LUND  
Sweden

© 2014 by Christian Månsson  
Daniel Stenberg. All rights reserved.  
Printed in Sweden by Media-Tryck.  
Lund 2014

# Abstract

Multirotor UAVs have in recent years become a trend among academics, engineers and hobbyists alike due to their mechanical simplicity and availability. Commercial uses range from surveillance to recreational flight with plenty of research being conducted in regards to design and control.

With applications towards search and rescue missions in mind, the main objective of this thesis work is the development of a mechanical design and control algorithm aimed at maximizing wind resistance. To these ends, an advanced multirotor simulator, based on helicopter theory, has been developed to give an accurate description of the flight dynamics. Controllers are then designed and tuned to stabilize the attitude and position of the UAV followed by a discussion regarding disturbance attenuation.

In order to study the impact of different design setups, the UAV model is constructed so that physical properties can be scaled. Parameter influence is then investigated for a specified wind test using a *Design of Experiments* methodology. These results are combined with a concept generation process and evaluated with a control engineering approach. It was concluded that the proposed final design should incorporate a compact three-armed airframe with six rotors configured coaxially.



# Acknowledgments

The authors of this thesis would like to thank their supervisors, Simon Yngve at Combine Control Systems and Professor Rolf Johansson at the Department of Automatic Control LTH, for their guidance and support.



# Contents

<b>List of Figures</b>	<b>9</b>
<b>List of Symbols and Abbreviations</b>	<b>12</b>
<b>1. Introduction</b>	<b>18</b>
1.1 Background . . . . .	18
1.2 Related work . . . . .	19
1.3 Aims of the thesis . . . . .	19
1.4 Autonomous flight regulations . . . . .	21
<b>2. Modeling</b>	<b>22</b>
2.1 Multicopter dynamics . . . . .	22
Basic flight control maneuvers . . . . .	22
6-DoF coordinate systems . . . . .	24
Rigid body equations . . . . .	25
2.2 DC motors . . . . .	26
2.3 Rotor dynamics . . . . .	29
Rotor motion . . . . .	29
Simplified rotor model . . . . .	31
Aerodynamic forces and moments . . . . .	32
Induced inflow model . . . . .	35
Rotor model validation . . . . .	37
2.4 Airframe dynamics . . . . .	41
2.5 Atmospheric model . . . . .	44
Wind model . . . . .	44
Air density . . . . .	47
<b>3. Control</b>	<b>48</b>
3.1 Overview . . . . .	48
3.2 PID control . . . . .	50
Cascaded control . . . . .	51
Attitude control . . . . .	51
Position control . . . . .	57
3.3 Control allocation . . . . .	61
3.4 Disturbance analysis . . . . .	62

<b>4. Multifactor analysis</b>	<b>65</b>
4.1 Design of experiments . . . . .	66
Screening . . . . .	68
Optimization . . . . .	76
<b>5. Design development</b>	<b>84</b>
5.1 Rotor and airframe assessment . . . . .	84
Rotor configurations . . . . .	85
Airframe configurations . . . . .	100
5.2 Concept evaluation . . . . .	107
Design criteria . . . . .	107
Results . . . . .	114
5.3 Proposed design . . . . .	114
<b>6. Performance comparison</b>	<b>117</b>
<b>7. Summary and conclusions</b>	<b>120</b>
<b>8. Future work</b>	<b>123</b>
<b>Bibliography</b>	<b>124</b>
<b>A. 6-DoF Kinematics</b>	<b>128</b>
<b>B. Geometric and inertia calculations</b>	<b>130</b>
B.1 Mass . . . . .	131
B.2 Moment of inertia . . . . .	131
B.3 Geometry . . . . .	132
<b>C. Aerodynamic theory</b>	<b>134</b>
C.1 Momentum theory . . . . .	134
C.2 Blade element theory . . . . .	140
C.3 Blade flapping . . . . .	144
C.4 Coaxial rotors . . . . .	148



# List of Figures

2.1	Thrust actuation. . . . .	23
2.2	Roll actuation. . . . .	23
2.3	Pitch actuation. . . . .	24
2.4	Yaw actuation. . . . .	24
2.5	Roll, pitch and yaw $\phi - \theta - \psi$ orientation angles. . . . .	25
2.6	Rotor blade motion. . . . .	30
2.7	Incident velocity distribution in hover and forward flight. . . . .	31
2.8	Rotor types generally used for multirotors. . . . .	32
2.9	Thrust, horizontal force and drag moment acting on a flapping rotor. . . . .	33
2.10	Definition of the sideslip angle. . . . .	34
2.11	Aerodynamic forces and moments expressed in $P_i, x_w, y_w, z_w$ . . . . .	34
2.12	Schematic overview of the rotor modeling, implemented in Simulink. . . . .	35
2.13	Induced velocity solution. . . . .	38
2.14	APC 10x4.7 Slowflyer propeller. . . . .	38
2.15	Wind tunnel test setup. . . . .	39
2.16	Chord length. . . . .	39
2.17	Blade twist. . . . .	39
2.18	Rotor model validation for CT and CQ. . . . .	41
2.19	Body drag force. . . . .	43
2.20	Centroid to center of gravity distance. . . . .	43
2.21	Wind gust. . . . .	45
3.1	The closed-loop multirotor system. . . . .	48
3.2	A generalized control problem. . . . .	49
3.3	The cascaded PID control structure. . . . .	51
3.4	Roll/pitch reference and disturbance step response. . . . .	53
3.5	$G_{cl}^{\phi\theta}$ Bode plot. . . . .	54
3.6	$S_u^{\phi\theta}$ Bode plot. . . . .	54
3.7	Yaw reference and disturbance step response. . . . .	56
3.8	$G_{cl}^{\psi}$ Bode plot. . . . .	56
3.9	$S_u^{\psi}$ Bode plot. . . . .	57
3.10	Position reference and disturbance step response. . . . .	59

## List of Figures

3.11	$G_{cl}^x$ Bode plot. . . . .	59
3.12	$S_u^x$ Bode plot. . . . .	60
3.13	Dryden wind PSD. . . . .	63
4.1	COST approach optimization. . . . .	65
4.2	Design of experiments optimization. . . . .	66
4.3	Wind test design. . . . .	68
4.4	Full factorial design. . . . .	71
4.5	Fractional factorial design. . . . .	71
4.6	Qualitative center points. . . . .	72
4.7	Linear regression coefficients for $e_{max}$ . . . . .	73
4.8	Linear regression coefficients for $P_{mean}$ . . . . .	73
4.9	Linear regression validation for $e_{max}$ . . . . .	74
4.10	Linear regression validation for $P_{mean}$ . . . . .	74
4.11	Student chart for $e_{max}$ . . . . .	74
4.12	Student chart for $P_{mean}$ . . . . .	75
4.13	Workspace in modeFRONTIER. . . . .	77
4.14	Central composite designs. . . . .	78
4.15	Quadratic regression coefficients for $e_{max}$ . . . . .	79
4.16	Quadratic regression coefficients for $P_{mean}$ . . . . .	79
4.17	Quadratic regression validation for $e_{max}$ . . . . .	79
4.18	Quadratic regression validation for $P_{mean}$ . . . . .	79
4.19	Student chart for $e_{max}$ . . . . .	80
4.20	Student chart for $P_{mean}$ . . . . .	80
4.21	Pareto-frontier from the optimization run. . . . .	81
4.22	The best designs with respect to wind resistance. . . . .	81
4.23	The best designs with respect to efficiency. . . . .	81
5.1	Equilibrium angle explanation. . . . .	86
5.2	Equilibrium angle and power loading for the APC 10x4.7 sf. . . . .	87
5.3	Design of experiments for the propeller simulations. . . . .	87
5.4	Design of experiments result: $\theta_{eq}$ . . . . .	88
5.5	Design of experiments result: $PL$ . . . . .	89
5.6	Three-bladed propeller comparison. . . . .	90
5.7	Scaled three-bladed propeller comparison. . . . .	91
5.8	Implementation of a variable pitch propeller. . . . .	92
5.9	Coaxial rotor comparison. . . . .	94
5.10	Scaled coaxial rotor comparison. . . . .	95
5.11	Ducted fan implementation. . . . .	96
5.12	Quadrotor: I4 config. . . . .	100
5.13	Quadrotor: X4 config. . . . .	100
5.14	Quadrotor: H4 config. . . . .	100
5.15	Quadrotor: V-Tail config. . . . .	101

5.16	Tricopter: Y3 config. . . . .	102
5.17	Tricopter: T3 config. . . . .	103
5.18	Hexacopter: X6 config. . . . .	104
5.19	Octorotor: I8 config. . . . .	105
5.20	Octorotor: V8 config. . . . .	106
5.21	X4 concept. . . . .	109
5.22	Y6 concept. . . . .	110
5.23	X6 concept. . . . .	111
5.24	X4S concept. . . . .	112
5.25	Y6 and X4S fusion concept. . . . .	115
5.26	Y6 configuration shown in the graphical interface of SimMechanics. .	116
6.1	Wind performance test. . . . .	118
6.2	Wind performance. . . . .	119
C.1	Momentum theory for hover. . . . .	135
C.2	Momentum theory for ascent flight. . . . .	137
C.3	Momentum theory for descent flight. . . . .	138
C.4	Momentum theory for forward flight [19]. . . . .	139
C.5	Aerodynamic environment at a typical blade element. . . . .	141
C.6	Momentum theory model for a coaxial rotor in hover. . . . .	148

# List of Symbols and Abbreviations

## Symbols

$A$	Rotor disk area [m <sup>2</sup> ]
$A$	Airframe reference area [m <sup>2</sup> ]
$A_{\infty}$	Vena contracta area [m <sup>2</sup> ]
$a_0$	Coning angle [rad]
$a_{1s}$	Longitudinal flapping angle [rad]
$A_x$	Projected surface area perpendicular to the $x$ -axis [m <sup>2</sup> ]
$A_{xy}$	Projected surface area perpendicular to the $x$ - and $y$ -axes [m <sup>2</sup> ]
$A_y$	Projected surface area perpendicular to the $y$ -axis [m <sup>2</sup> ]
$A_z$	Projected surface area perpendicular to the $z$ -axis [m <sup>2</sup> ]
$b_{1s}$	Lateral flapping angle [rad]
$b$	Thrust coefficient [Ns <sup>2</sup> ]
$c$	Chord length [m]
<b>C</b>	Centroid [m]
$C_d$	Drag coefficient [–]
$C_d$	Local drag coefficient [–]
$C_H$	Nondimensional horizontal force coefficient [–]
$C_l$	Local lift coefficient [–]
$C_{l\alpha}$	2-D lift-curve-slope of the airfoil section [rad <sup>–1</sup> ]
$C_P$	Nondimensional power coefficient [–]
$C_Q$	Nondimensional drag moment coefficient [–]
$C_T$	Nondimensional thrust coefficient [–]
<b>G</b>	Center of gravity [m]
$d$	Drag coefficient [Nms <sup>2</sup> ]
$d_m$	Gust length [m]
$dC_H$	Infinitesimal horizontal force coefficient [–]
$dC_Q$	Infinitesimal drag moment coefficient [–]

$dC_T$	Infinitesimal thrust coefficient [—]
$dD$	Infinitesimal drag force [N]
$dF_x$	Infinitesimal force parallel to the rotor disk [N]
$dF_z$	Infinitesimal force perpendicular to the rotor disk [N]
$dH$	Infinitesimal horizontal force [N]
$dL$	Infinitesimal lift force [N]
$dQ$	Infinitesimal drag moment [Nm]
$dT$	Infinitesimal thrust force [N]
$e(t)$	Control error signal [—]
$e$	Flapping hinge offset [m]
$e$	Distance error [m]
$e_{max}$	Maximum position error [m]
$F_{aero}$	Input force disturbance [N]
$F_d$	Drag force [N]
$F_{dx}, F_{dy}, F_{dz}$	Drag force body frame components [N]
$F_{xi}, F_{yi}, F_{zi}$	Force components expressed in $P_i, x, y, z$ [N]
$f_{xi}, f_{yi}, f_{zi}$	Force components expressed in $P_i, x_w, y_w, z_w$ [N]
$F_{xy}$	Horizontal force component expressed in $P_i, x, y, z$ [N]
$g$	Gravitational acceleration [ $m/s^2$ ]
$F_r(s)$	Reference to control signal transfer function [—]
$F_y(s)$	Measurement to control signal transfer function [—]
$G_{cl}(s)$	Reference closed-loop transfer function [—]
$h$	Flight altitude [m]
$H$	Horizontal force [N]
$h_a$	Height of the arm [m]
$h_c$	Height of the center [m]
$\mathbf{H}_B^I$	Direction Cosine Matrix
$h_m$	Height of the motor [m]
$h_s$	Height of the shaft [m]
$H_u(s), H_v(s), H_w(s)$	Dryden linear filters [N]
$\mathbf{i}, \mathbf{j}, \mathbf{k}$	unit vectors for $P_i, x, y, z$
$\mathbf{i}_w, \mathbf{j}_w, \mathbf{k}_w$	unit vectors for $P_i, x_w, y_w, z_w$
$I$	Norm of the inertia tensor [ $kgm^2$ ]
$I$	Current [A]
$I_{XX}$	$x$ -axis moment of inertia [ $kgm^2$ ]
$I_{yb}$	Blade moment of inertia around the flapping hinge [ $kgm^2$ ]
$I_{YY}$	$y$ -axis moment of inertia [ $kgm^2$ ]
$I_{ZZ}$	$z$ -axis moment of inertia [ $kgm^2$ ]
$J$	Rotational inertia experienced by the motor [ $kgm^2$ ]
$J_p$	Rotational inertia of the propeller [ $kgm^2$ ]

## List of Symbols and Abbreviations

$J_r$	Rotational inertia of the rotor [kgm <sup>2</sup> ]
$J_s$	Rotational inertia of the shaft [kgm <sup>2</sup> ]
$k_\beta$	Torsional spring constant [Nm/rad]
$K_c$	Induced inflow distribution slope [—]
$K_e$	Back-emf constant [V/(rad/s)]
$K_P, K_I, K_D$	Proportional, integral and derivative control parameters [—]
$K_s$	Geometrical scaling factor [—]
$K_t$	Motor torque constant [Nm/A]
$l$	Arm length [m]
$L$	Armature inductance [H]
$L_u, L_v, L_w$	Turbulence scale lengths [m]
$l_a$	Arm length [m]
$\mathbf{L}_B^1$	Rotation Cosine Matrix
$\dot{m}$	Mass flow rate [kg/s]
$m_a$	Arm mass [kg]
$m_c$	Center mass [kg]
$m_p$	Propeller mass [kg]
$m_s$	Shaft mass [kg]
$m_{tot}$	Total mass [kg]
$M_d$	Drag moment [Nm]
$M_{xi}, M_{yi}, M_{zi}$	Moment components expressed in $P_i, x, y, z$ [Nm]
$m_{xi}, m_{yi}, m_{zi}$	Moment components expressed in $P_i, x_w, y_w, z_w$ [Nm]
$N$	Gear box reduction ratio [—]
$N$	Control-loop tuning factor [—]
$n_a$	Number of arms [—]
$N_b$	Number of blades [—]
$n_r$	Number of rotors [—]
$p, q, r$	Body-frame rotational velocities [rad/s]
$p, q, r$	Rotational wind turbulence components [rad/s]
$P_{mean}$	Mean power [W]
$P_i, x, y, z$	Local coordinate system for rotor i
$P_i, x_w, y_w, z_w$	Local wind coordinate system for rotor i
$PL$	Power loading [N/W]
$p_w, q_w$	Airframe angular velocities expressed in $P_i, x_w, y_w, z_w$ [rad/s]
$q$	Dynamic pressure [N/m <sup>2</sup> ]
$Q$	Drag moment [Nm]
$R$	Rotor radius [m]
$R$	Armature resistance [ $\Omega$ ]
$r(t)$	Reference signal [—]
$r_0$	Distance between the blade root and the rotational axis [m]

$r_c$	Radius of the center [m]
$\mathbf{r}_d$	Centroid to CoG distance vector [m]
$\mathbf{r}_{dx}, \mathbf{r}_{dy}, \mathbf{r}_{dz}$	Centroids in the $x$ , $y$ and $z$ directions [m]
$r_{Gb}$	Flapping hinge and blade CoG distance [m]
$r_m$	Radius of the motor [m]
$r_s$	Radius of the shaft [m]
$S(s)$	Sensitivity transfer function [—]
$S_u(s)$	Input sensitivity transfer function [—]
$T$	Thrust [N]
$T(s)$	Complementary sensitivity transfer function [—]
$t_0$	Wind disturbance start time [s]
$t_f$	Wind disturbance final time [s]
$T_{max}$	Maximum thrust [N]
$u(t)$	Control signal [—]
$u, v, w$	Body frame translational velocities [m/s]
$u, v, w$	Translational wind turbulence components [m/s]
$U$	Resultant air flow speed [m/s]
$U_1$	Thrust force, control input [N]
$U_2$	Roll moment, control input [Nm]
$U_3$	Pitch moment, control input [Nm]
$U_4$	Yaw moment, control input [Nm]
$U_P$	Vertical air flow speed component [m/s]
$U_T$	Horizontal air flow speed component [m/s]
$v$	Fluid onset velocity [m/s]
$V$	Voltage [V]
$V$	Mean-wind relative airspeed [m/s]
$V_c$	Climb velocity [m/s]
$v_h$	Induced velocity in hover [m/s]
$v_i$	Induced velocity [m/s]
$v_l$	Lower rotor induced velocity in a coaxial configuration [m/s]
$v_M$	Wind gust magnitude [m/s]
$v_u$	Upper rotor induced velocity in a coaxial configuration [m/s]
$v_w$	Wind speed [m/s]
$v_{wg}$	Wind gust speed [m/s]
$v_{wm}$	Wind mean speed [m/s]
$v_{wt}$	Wind turbulence speed [m/s]
$V_\infty$	Wind magnitude [m/s]
$w$	Induced vena contracta velocity [m/s]
$W$	Weight force [N]
$W_{20}$	Specific wind speed 20 ft above the ground [m/s]

## List of Symbols and Abbreviations

$w_a$	Width of the arm [m]
$x, y, z$	Inertial frame position [m]
$y(t)$	Measurement signal [—]
$z$	Vertical deflection [m]
$z_a$	Vertical distance for the CoG of the arm [m]
$z_{CG}$	Vertical distance between the CoG and the centroid [m]
$z_m$	Vertical distance for the CoG of the motor [m]
$z_{PG}$	Vertical distance between the CoG and the rotor plane [m]
$z_s$	Vertical distance for the CoG of the shaft [m]
$\alpha$	Rotor disk angle of attack [rad]
$\beta$	Blade flapping angle [rad]
$\beta$	Thrust margin [—]
$\beta_{SS}$	Sideslip angle [rad]
$\varepsilon$	Convergence error [—]
$\theta$	Blade twist [rad]
$\theta_0$	Propeller blade twist at the root of the blade [rad]
$\theta_{eq}$	Equilibrium angle [rad]
$\theta_{tw}$	Linear slope of the propeller blade twist [rad]
$\kappa$	Measured induced power factor [—]
$\lambda$	Motor damping coefficient [Nm/(rad/s)]
$\lambda$	Rotor inflow ratio [rad <sup>-1</sup> ]
$\lambda_h$	Inflow ratio during hover [rad <sup>-1</sup> ]
$\lambda_i$	Induced inflow ratio [rad <sup>-1</sup> ]
$(\lambda_i)_{local}$	Locally induced inflow ratio [rad <sup>-1</sup> ]
$\lambda_c$	Climb inflow ratio [rad <sup>-1</sup> ]
$\mu$	Rotor advance ratio [rad <sup>-1</sup> ]
$\sigma$	Rotor solidity [—]
$\sigma_u, \sigma_v, \sigma_w$	Turbulence intensities [—]
$\tau$	Time constant [s]
$\tau_{aero}$	Input moment disturbance [Nm]
$\tau_{load}$	External motor load torque [Nm]
$\rho$	Air density [kg/m <sup>3</sup> ]
$\phi, \theta, \psi$	Roll, pitch and yaw Euler angles [rad]
$\phi$	Induced angle [rad]
$\Phi_u, \Phi_v, \Phi_w$	Power spectral density functions [—]
$\Psi$	Azimuth angle [rad]
$\Omega$	Rotor rotational speed [rad/s]



## **Abbreviations**

BET	Blade Element Theory
CAD	Computer-Aided Design
CCC	Central Composite Circumscribed
CCF	Central Composite Face-centered
CCI	Central Composite Inscribed
CFD	Computational Fluid Dynamics
COESA	U.S. Committee On Extension to the Standard Atmosphere
CoG	Center of Gravity
DC	Direct Current
DCM	Direction Cosine Matrix
DOE	Design Of Experiments
DoF	Degree of Freedom
EASA	European Aviation Safety Agency
EPFL	École Polytechnique Fédérale de Lausanne
ETH	Eidgenössische Technische Hochschule
GPS	Global Positioning System
HP	Hub Plane
LTH	Lunds Tekniska Högskola
MOGA	Multi Objective Genetic Algorithm
MT	Momentum Theory
PID	Proportional Integral Derivative
PSD	Power Spectral Density
RSM	Response Surface Methodology
TPP	Tip Path Plane
TWS	Turbulent Wake State
UAV	Unmanned Aerial Vehicle
UIUC	University of Illinois at Urbana-Champaign
VRS	Vortex Ring State
VTOL	Vertical Take-Off and Landing
WBS	Windmill Brake State

# 1

## Introduction

### 1.1 Background

Small scale unmanned aerial vehicles (UAV) with vertical take-off and landing (VTOL) capabilities have produced increased interest in recent years. One of the most common concepts is the multirotor, which, as its name suggests, is an aircraft based on utilizing several propellers. The multirotor provides a simple platform to achieve flight control while delivering high levels of maneuverability without the complex mechanics of a conventional helicopter. Not only are their properties studied in the commercial and academical spheres, but they have also intrigued the public with growing communities of hobbyists. There are a number of designs and configurations available on the market, and whereas some have distinct qualities, many are simply designed for entertainment.

Normally, a store-bought multirotor will include a radio controller requiring a pilot on the ground to control the flight path. For more advanced applications and possibly more accurate flight, the aircraft is often made to act in a more autonomous fashion. It is common to make the UAV adhere to preplanned flight trajectories and even make logical decisions based on sensor input. Such flight puts extra requirements on the control setup and algorithms as well as the onboard equipment to ensure safe and steady flight in varying conditions.

Perhaps the largest areas of application of the multirotor is within the photography and surveillance industries. Possible tasks include surveying of buildings, border patrol or aerial filming of events, each with specific requirements on design specifications and control performance. An application of great interest to this thesis is the use of multirotors to assist in search and rescue missions. Outfitting a multirotor with a thermal camera may provide significant aid in locating missing people and thus becoming a valuable tool for search parties. In fact, Swedish law enforcement are currently investigating the possibility of using UAVs for surveillance and search applications, indicating a genuine interest for applying UAV technology to the aforementioned ends [26, 27]. To ensure reliable performance of such multirotor UAVs, providing a design able to cope with challenging wind conditions is of major interest and will be the main focus of this thesis.

## 1.2 Related work

A number of master's thesis projects concerning multirotors have previously been conducted at Combine Control Systems AB. The first project was conducted in cooperation with Chalmers University of Technology where Niklas Ohlsson and Martin Ståhl presented an autonomous multirotor prototype with the ability to navigate with computer vision [31]. Since then, Johan Fogelberg has performed a sensor fusion project for GPS-deprived environments [13] and Sara Gustafzelius based her thesis on navigation with an onboard camera. Another thesis is currently running in parallel at Combine's Gothenburg office where optimal search algorithms are being developed for multirotors acting as a flock.

A great number of articles and reports regarding multirotors is easily accessible thanks to the huge interest during recent years. Inspiration has been found in various work from control and aerospace departments at institutions such as EPFL in Lausanne, ETH in Zürich, Cranfield University, Australian National University and Lund University. In addition, publications from organizations such as the Institute of Electrical and Electronics Engineers (IEEE), the American Institute of Aeronautics and Astronautics (AIAA), the American Helicopter Society (AHS) and the National Aeronautics and Space Administration (NASA) have been reliable sources of information. Dedicated robotics research groups have shown a lot of interest towards multirotors, contributing with innovative research resulting in numerous publications. Two of the most prominent are the D'Andrea Group, lead by Professor D'Andrea at ETH Zürich, and the Kumar Lab Group, lead by Professor Vijay Kumar at the University of Pennsylvania. Both of these have been sources of fascination and inspiration to the authors.

The extensive modeling in this thesis project has mainly been inspired by the works of Martínez [21] and Pounds [33], reinforced by helicopter theory based on Leishman's *Principles of Helicopter Aerodynamics* [19] and Prouty's *Helicopter Performance, Stability and Control* [35]. Control analysis and design has been performed using methods and conventions presented in Glad and Ljung's *Reglerteori - Flervariabla och olinjära metoder*. Inspiration on different control strategies has primarily been found in Bouabdallah's extensive work [3]. In the proceeding design work, the multifactor analysis has been performed in accordance to data analysis company Umetric's book *Design of Experiments* [11].

## 1.3 Aims of the thesis

In control analysis and design, it is often the case that a physical process is predetermined with very little ability to influence its core functionality and characteristics. Any adjustments to the actual plant, with the intent to increase control capability, are therefore generally limited. Here, however, modeling and control based design

development is put to practice with the ability to alter and test physical designs in a simulated environment. Control and mechanical design can thus be developed in tandem, aided by simulation and optimization software along with design development methodology.

With application towards search and rescue missions in mind, the main goal of this thesis work is to create a favorable multirotor design for flight in windy conditions. This is seen as a major requirement in order to guarantee mission performance and reliability in a larger range of external conditions. In order to reach this goal, several milestone objectives must be performed to create an environment where designs can be evaluated with sufficient accuracy. These objectives represent the main contributions of this thesis work and are summarized in the list below.

- **Multirotor modeling:** The development of a realistic model describing multirotor flight conditions and external phenomena with accuracy is highly important in enabling design evaluation. This includes research of motor dynamics as well as rotor and airframe aerodynamics. Hence, a lot of attention is paid to this, whereas in other multirotor control projects much simpler models are often sufficient. Implementation of the deduced model in a simulator environment, where it is possible to configure various dimension and mass properties, enables analysis of parameter influence. A realistic simulator can also provide a more realistic testing platform, on which further work concerning control and design can be conducted.
- **Wind modeling:** Modeling of typical wind characteristics to include in the model simulator is important to add realism to the magnitude and variations of forces caused by the onset of wind. Using this, suitable wind test cases can be created to enable evaluation of design and control performance.
- **Control algorithm development:** Developing a suitable control algorithm to control the multirotor during flight is essential. Since it is presumed that a search and rescue mission will be performed by trajectory planning, possibly following a search algorithm, the control architecture must provide positional control. Also, a control theory analysis is performed on how external disturbances enter the system and what effects they might have.
- **Multifactor analysis:** An extensive evaluation of a generic multirotor is performed by studying the influence of parameters such as geometrical dimensions and mass properties in a multifactor analysis methodology. This is performed by running the simulator with different parameter combinations while the performance is evaluated.
- **Design development:** The design development concerns the strategy of how to reach a suitable multirotor design. This is achieved by evaluating current

multirotor configurations and assessing their properties and uses for the aims of this thesis work. The research is broken down into study of airframes and rotor configurations separately. To reach a final design, a set of performance criteria is assembled and given a relative weighting according to their rated importance. Utilizing the conclusions drawn from the multifactor analysis and design assessments, a few candidate concepts are put together and given a score for each criteria according to their anticipated performance.

Considering all of the topics of research mentioned above makes the task of multirotor design a multi-faceted one, requiring knowledge and research in a variety of engineering branches. It should be noted that this thesis work is done at a conceptual level and, although the physical model is aimed at being as realistic as possible, many other realism effects and implementation aspects are neglected (such as real-time constraints and sensor readings). The final design results and performance evaluations may be seen as a fore-study to a continuation of multirotor UAV control and implementation for search and rescue missions.

## 1.4 Autonomous flight regulations

For search and rescue applications, it is desirable to have multirotors act autonomously according to predetermined flight paths. In order to operate an aircraft autonomously in Sweden for scientific, commercial or non-recreational purposes, permission must be granted by the Swedish Transport Agency (Transportstyrelsen) [43]. Different types of UAVs are categorized into different classes depending on their take-off weight, maximum kinetic energy and operational premises. Classes 1A (0-1.5 kg) and 1B (1.5-7 kg) are for lighter UAVs, which will most likely be the weight region of the UAV designed in this thesis. These classes, however, only concern UAVs operated within the line of sight of the operator. Class 3 classification concerns those UAVs which may operate beyond the line of sight which is likely for search and rescue missions.

Class 3 UAVs need to be certified by the European Aviation Safety Agency (EASA) before flight permission may be granted by the Swedish Transport Agency. It is also possible to apply for special permission for occasional flight or flight in specific areas. Among a list of things, the operator must be able to override the automatic control at all times and in the event of communication failure the aircraft must be disabled safely. A full report on UAV regulations from the Swedish Transport Agency can be downloaded from their website [43]. In a practical implementation of UAVs operating in those application areas mentioned in this thesis, these regulations will have to be considered and adhered to.

# 2

## Modeling

The importance of accurate modeling of a multirotor for a variety of flight conditions is seen as critical for a successful design development process. Hence, in this chapter an advanced multirotor model is presented considering motors, rotors, airframe and wind dynamics. The modeled multirotor system has six degrees of freedom, where each type of movement is associated with a number of forces and moments. Derivation of the aerodynamic forces and moments has been made with well regarded helicopter rotor theory primarily based on the works of Leishman [19] and Prouty [35]. An adaption to the small scale multirotor case is inspired by the extensive thesis work made by Martínez [21].

The model presented in this chapter has been implemented in MATLAB's simulation environment to create a multirotor simulator, enabling analysis and evaluation of control and design. MATLAB is a numerical computation software developed by Mathworks, providing a block-programming simulation environment known as Simulink. Within Simulink [24], the Simscape toolboxes SimMechanics and SimElectronics have been used extensively. These environments provide useful tools to implement mechanical and electronic systems. A graphical 3D environment is also provided by SimMechanics, where the simulation results can be visualized.

### 2.1 Multirotor dynamics

#### Basic flight control maneuvers

In a multirotor UAV, there are four principal means of control actuation to achieve desired movement — thrust, roll, pitch and yaw. Since any aircraft operates in a six degrees of freedom (6-DoF) space, the system is underactuated. This basically means that the vehicle will not be able to fully control all of the translational and rotational movements at the same time. It is however, possible to indirectly control the position by determining the thrust and its direction so that a desired flight trajectory can be achieved.

Below, the four means of actuation, thrust force and moments, are listed and described. The accompanying figures illustrate the resulting movements for a simple

quadrotor structure with coordinates fixed to the vehicle's body. The circles beside each  $\Omega_i$ ,  $i = 1, \dots, 4$  indicate the propeller speeds of each rotor, where a larger circle means higher speed. The force created at each rotor is indicated by a vertical arrow.

- **Thrust force -  $U_1$ .**

The thrust force is generated by increasing or decreasing the speed of the multirotor propellers. The force from each rotor contributes to a total thrust force directed upwards in an body coordinate frame. For a common quadrotor configuration, Figure 2.1 shows the applied thrust due to the rotational speed of the rotors.

- **Roll moment -  $U_2$ .**

A rolling moment is achieved by altering the rotational speeds of the rotors around the body  $x$ -axis. Rotors to the left of the  $x$ -axis contribute to a positive moment. The generation of a roll maneuver is shown in Figure 2.2.

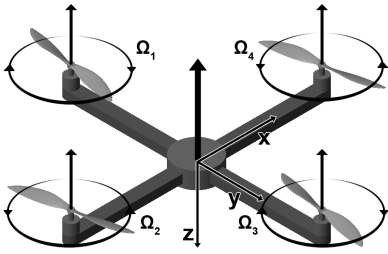


Figure 2.1: Thrust actuation.

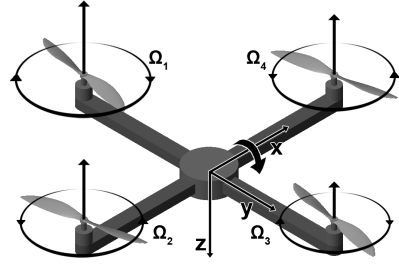


Figure 2.2: Roll actuation.

- **Pitch moment -  $U_3$**

A pitch moment is achieved by altering the rotational speeds of the rotors around the body  $y$ -axis. Rotors to the left of the  $y$ -axis contribute to a positive moment. Figure 2.3 shows how a pitch maneuver is performed.

- **Yaw moment -  $U_4$**

The rotation of the rotors encounter a drag force when rotating in the air. This results in a reaction moment on the airframe directed in the opposite direction of a rotors' rotational direction. Figure 2.4 shows how yaw movement is achieved by altering the propellers' individual speeds depending on if they rotate in a clockwise or counter-clockwise direction. For a multirotor to control its yaw orientation it is important that half of its propellers rotate clockwise and the other half counter clockwise. Thus, a large part of any unwanted yaw moment is eliminated for most flight cases.

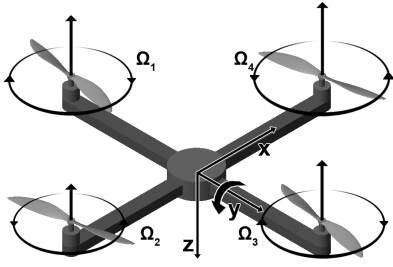


Figure 2.3: Pitch actuation.

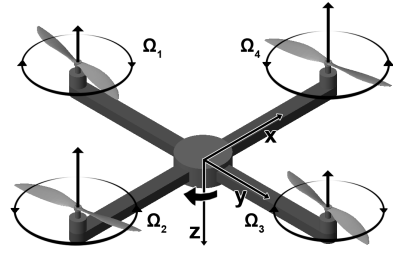


Figure 2.4: Yaw actuation.

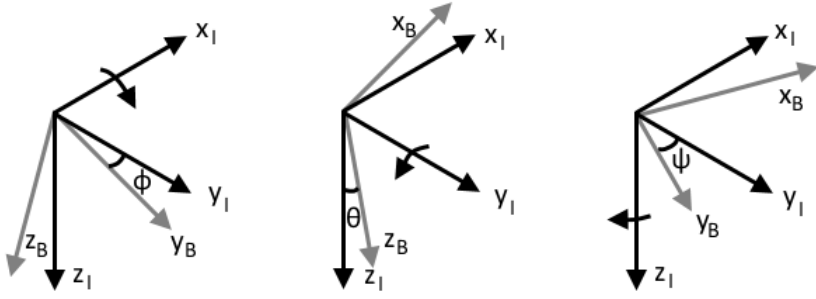
## 6-DoF coordinate systems

In flight applications, an aircraft's movement is typically expressed by six basic types of movement or degrees of freedom (6-DoF). In an inertial (fixed) coordinate system, these are the three translational movements along the  $x - y - z$  directions as well as the rotational angles  $\phi - \theta - \psi$ , commonly known as roll, pitch and yaw angles. These three angles represent the attitude of the aircraft and are defined as the aircraft's rotated angles around each of the inertial axes. coordinate system. The flight dynamics conventions presented in this section follow the theory of Robert F. Stengel [39].

It is often convenient to describe an aircraft's dynamics in a body-fixed coordinate system with the origin placed at the center of gravity. Good reasons for this includes that the actuation of forces and moments are decoupled, and thus more easily described, in such a coordinate system. Some of the sensor readings are also typically expressed in the body frame. Also, the moment of inertia tensor does not change with the body frame orientation since the body coordinates follow the rotational motion of the aircraft. The orientation of the body frame with respect to the inertial frame is illustrated in Figure 2.5 below. According to the DIN 9300 standard [1], the vertical  $z$ -axis should be pointing in the "downwards" direction in aerospace applications. This convention will be followed in this thesis work.

To express translational and rotational movement in both coordinate systems, transformation matrices between them are used. For translational motion the matrix  $\mathbf{H}_B^I$  in (2.1), often called the *direction cosine matrix*, is used to transform velocity and acceleration from the body to the inertial frame. Likewise, angular velocity and angular acceleration in the body frame can be transformed to equivalences in the inertial frame using  $\mathbf{L}_B^I$  (2.2). For instance, velocity measured in the body frame  $\mathbf{v}_B$  can be represented in the inertial frame by the transformation  $\mathbf{v}_I = \mathbf{H}_B^I \mathbf{v}_B$ . In order to represent a quantity measured in the inertial frame in the body frame, the inverses of  $\mathbf{H}_B^I$  and  $\mathbf{L}_B^I$  are used. Reusing the example for the linear velocity, but instead transforming from the inertial frame, the expression  $\mathbf{v}_B = (\mathbf{H}_B^I)^{-1} \mathbf{v}_I$  yields



Figure 2.5: Roll, pitch and yaw  $\phi - \theta - \psi$  orientation angles.

the corresponding velocity in the body frame.

$$\mathbf{H}_B^I = \begin{bmatrix} \cos \theta \cos \psi & \sin \phi \sin \theta \cos \psi - \sin \psi \cos \phi & \cos \phi \sin \theta \cos \psi + \sin \phi \sin \psi \\ \cos \theta \sin \psi & \sin \phi \sin \theta \sin \psi + \cos \phi \cos \psi & \cos \phi \sin \theta \sin \psi - \sin \phi \cos \psi \\ -\sin \theta & \sin \phi \cos \theta & \cos \phi \cos \theta \end{bmatrix} \quad (2.1)$$

$$\mathbf{L}_B^I = \begin{bmatrix} 1 & \sin \phi \tan \theta & \cos \phi \tan \theta \\ 0 & \cos \phi & -\sin \phi \\ 0 & \sin \phi / \cos \theta & \cos \phi / \cos \theta \end{bmatrix} \quad (2.2)$$

The direction cosine matrix (2.1) is orthogonal, which makes its inverse equal to its transpose,  $(\mathbf{H}_B^I)^{-1} = (\mathbf{H}_B^I)^T$ . It is, however, important to note that  $(\mathbf{L}_B^I)^{-1} \neq (\mathbf{L}_B^I)^T$ .

## Rigid body equations

The rigid body kinematics for the multirotor dynamical system will here be described using Newton-Euler formalism in the body coordinate system. For a 6-DoF rigid body, such as the multirotor aircraft, this takes the generalized form of (2.3) below. In the system description  $\mathbf{I}_{3 \times 3}$  is a  $3 \times 3$  identity matrix,  $\mathbf{0}_{3 \times 3}$  a  $3 \times 3$  containing only zeros,  $\mathbf{I}$  is the  $3 \times 3$  inertia tensor matrix,  $\mathbf{v}_B$  is the body frame translational velocity and  $\omega_B$  is the body frame rotational velocity. Finally,  $\mathbf{F}_B$  and  $\tau_B$  are the forces and moments acting on the body described in the body frame. The derivations made in this section follow the methods presented by Stengel [39] and Bresciani [6].

$$\begin{bmatrix} \mathbf{I}_{3 \times 3} & \mathbf{0}_{3 \times 3} \\ \mathbf{0}_{3 \times 3} & \mathbf{I} \end{bmatrix} \begin{bmatrix} \dot{\mathbf{v}}_B \\ \dot{\omega}_B \end{bmatrix} + \begin{bmatrix} \omega_B \times (m \mathbf{v}_B) \\ \omega_B \times (\mathbf{I} \omega_B) \end{bmatrix} = \begin{bmatrix} \mathbf{F}_B \\ \tau_B \end{bmatrix} \quad (2.3)$$

As previously mentioned, it has been assumed that the body coordinate system has its origin at the center of gravity and that the axes coincide with the principal inertia axes (so that  $\mathbf{I}$  is diagonal). This results in an easier description of the forces and moments applied to the system as well as that the inertia tensor  $\mathbf{I}$  is a diagonal matrix, which further simplifies the system description. Henceforth, the notations for the body frame velocities and inertia tensor components are shown in Equations (2.4) and (2.5).

$$\mathbf{v}_B = [u \quad v \quad w]^T \quad \boldsymbol{\omega}_B = [p \quad q \quad r]^T \quad (2.4)$$

$$\mathbf{I} = \begin{bmatrix} I_{XX} & 0 & 0 \\ 0 & I_{YY} & 0 \\ 0 & 0 & I_{ZZ} \end{bmatrix}^T \quad (2.5)$$

Using these notations, the dynamics in (2.3) can be written as a system of equations, which can be seen in (2.6). It can be seen clearly that the system is nonlinear with coupled terms between the translational and rotational velocities. The expressions for the forces and moments are kept in a generalized form for now, but more nonlinearities enter with them.

$$\left\{ \begin{array}{l} \dot{u} = \quad \quad \quad vr - wq \quad + \quad \frac{1}{m} F_x \\ \dot{v} = \quad \quad \quad wp - ur \quad + \quad \frac{1}{m} F_y \\ \dot{w} = \quad \quad \quad uq - vp \quad + \quad \frac{1}{m} F_z \\ \dot{p} = \quad \frac{I_{YY} - I_{ZZ}}{I_{XX}} qr \quad + \quad \frac{1}{I_{XX}} \tau_x \\ \dot{q} = \quad \frac{I_{ZZ} - I_{XX}}{I_{YY}} pr \quad + \quad \frac{1}{I_{YY}} \tau_y \\ \dot{r} = \quad \frac{I_{XX} - I_{YY}}{I_{ZZ}} pq \quad + \quad \frac{1}{I_{ZZ}} \tau_z \end{array} \right. \quad (2.6)$$

## 2.2 DC motors

The DC motors are the actuators of the multirotor propellers. Rotational motion is achieved by running a current through the coils where the resulting magnetic field is cyclically attracted and repelled by the stator magnet. Resulting rotational speeds are transmitted from the motors to the propellers to generate an upward thrust. There

are a number of constants that define a common DC motor's characteristics, which are listed in Table 2.1 below. It is common to equip DC motors with some kind of transmission that adjusts the torque and the rotational speed of the load. For multirotors, this can be needed to find a suitable operational range for the specific propeller.

Parameter	Notation	Unit
Armature inductance	$L$	H
Armature resistance	$R$	$\Omega$
Rotational inertia	$J$	$\text{kgm}^2$
Damping coefficient	$\lambda$	$\text{Nm}/(\text{rad/s})$
External load torque	$\tau_{load}$	Nm
Back-emf constant	$K_e$	$\text{V}/(\text{rad/s})$
Motor torque constant	$K_t$	$\text{Nm/A}$
Gear reduction ratio	$N$	-

Table 2.1: List of motor parameters.

**Motor torque and back-emf constants**  $K_e$  and  $K_t$  associate voltage and current with output torque and speed of the motor. In SI-units, they take the same numerical values although they are associated with different phenomena. Henceforth,  $K$  will be used for both ( $K = K_e = K_t$ ).

**Gear reduction ratio** The gear reduction ratio  $N$  determines the ratio between motor and propeller torques and rotational speeds  $\Omega_M = N\Omega_P$ . It is chosen such that the propeller operates in a desirable and safe speed range.

**Rotational inertia** The rotor is connected to the propeller and its shaft through the motor gear. The rotor rotational inertia  $J_r$  around the propeller shaft axis is described by (2.7), where the contributions of the shaft  $J_s$  and propeller  $J_p$  are added. Assuming an idealized motor, with zero internal rotational inertia, the the total inertia  $J$  experienced by the motor is described by the right-hand equation in (2.7).

$$J_r = J_s + J_p \quad J = \frac{1}{N} J_r \quad (2.7)$$

**Damping** The damping of the DC motor is often very hard to estimate and is generally very small. Therefore, the coefficient  $\lambda$  will be approximated to zero in this thesis work.

## Motor dynamics

The mathematical model of a DC motor is obtained using Kirchoff's voltage law and Newton's second law. The system equations for a general DC motor are shown below in (2.8). This section has largely been inspired by the DC motor theory presented by Javier R. Movellan [29] but include some alterations.

$$\begin{aligned} V &= L \frac{dI}{dt} + RI + K\Omega_M \\ J \frac{d\Omega_M}{dt} &= KI - \lambda\Omega_M - \tau_{load} \end{aligned} \quad (2.8)$$

Considering the expressions derived above, as well as neglecting the very fast transient effects due to the inductance as well as the damping, the resulting equation for the DC motor is presented in Equation (2.9). Note that the external inertia as well as the external load torque are divided by  $N$ . The load torque for a multirotor is the drag moment caused by the rotation of the propeller. It has a quadratic dependence on the rotational speed of the propeller,  $\tau_{load} = d\Omega_P^2$ .

$$\begin{aligned} V &= RI + K\Omega_M \\ \frac{1}{N} J_r \dot{\Omega}_M &= -\frac{K^2}{R} \Omega_M - \frac{d}{N^3} \Omega_M + \frac{K}{R} V \end{aligned} \quad (2.9)$$

Rewriting this equation for the propeller speed results in the dynamic equation below (2.10).

$$J_r \dot{\Omega}_P = -\frac{K^2 N^2}{R} \Omega_P - d\Omega_P^2 + \frac{KN}{R} V \quad (2.10)$$

**Steady state analysis** When the motors have been running with a constant input voltage for a short amount of time, the rotational speed of the motor has reached a steady state. In general, the time constants of the motors are very fast. This is due to the low electrical inductance and rather low rotational inertia in the kind of motors and propellers used in multirotor applications. This means that the rotational accelerations  $\dot{\Omega}_M$  will be zero in the motor system equations (2.8) almost instantaneously for a given input voltage  $V$ . The steady state equations for the DC motors take the form of (2.11), after some rearranging.

$$\begin{aligned} \Omega_M^2 + \frac{K^2 N^3}{Rd} \Omega_M - \frac{KN^3}{Rd} V &= 0 \\ \Omega_P^2 + \frac{K^2 N^2}{Rd} \Omega_P - \frac{KN}{Rd} V &= 0 \end{aligned} \quad (2.11)$$

Conversely, the required voltage needed to reach a specific speed can easily be obtained from the polynomials above. Since the motor dynamics are fast, these expressions will be used to calculate the input voltage to the motor from a desired propeller speed when actuating control output in the simulator. The expression used to obtain a certain steady state propeller speed is given below in (2.12).

$$V = \frac{Rd}{KN}\Omega_P^2 + KN\Omega_P \quad (2.12)$$

**Transient behavior** Since the dynamic equation in (2.10) is non-linear, due to the load torque's quadratic dependence on the rotational speed. The time constant of the motor can therefore not be deduced directly from this equation. For zero load torque ( $d = 0$ ) on the motor, the time constant becomes  $\tau = JR/(K^2N^2)$ , which for the modeled motor and propeller configuration becomes  $\tau \approx 0.03$  s. Since  $d$  will be relatively small, no significant increase in the time constant will be imminent. It should be noted that the time constant identified by Fogelberg [13] for a similar motor as the one modeled here was much larger. It is, however, believed that there are some unwanted system delays in the previously used hexacopter at Combine.

## 2.3 Rotor dynamics

The aim of this section is to develop a realistic model of a conventional rotor. Different rotor phenomena will be discussed, and the aerodynamic forces and moments acting on the rotor will be derived. Rotors can be modeled in many ways and the choice of method is determined by a compromise between accuracy and effort, depending on which is more important for the task at hand. It was decided to use a theoretical model for this project because of the possibility to provide information about how different propeller parameters affect the behavior of the rotor. Additionally, an empirical model would be limited to the specific rotor that would be used during necessary identification tests. During this project, a combination of *blade element theory* (BET) and *momentum theory* (MT) have been used. These methods have frequently been used for helicopter studies [19, 35], and more recently for multirotor modeling where satisfying results have been achieved by Martínez and others [21, 2, 3]. There are more complex computational methods available such as solving the Navier-Stokes equations or using different wake methods, but this requires a tremendous amount of effort and doesn't fit into the time frame of this thesis work.

### Rotor motion

Aerodynamic forces and moments are generated when a rotor is propelled through the surrounding air. Thrust is the lift force which is produced by rotating the rotor blades at a certain velocity  $\Omega$ . This rotation will also cause a drag moment around

the rotational axis which will oppose the DC motor. In addition to the rotation, the blades will also experience three different types of motion which are called feathering, blade flapping and lagging, which can be seen in Figure 2.6. These motions affect the flight characteristics of the multirotor and are all dependent on the stiffness of the propeller.

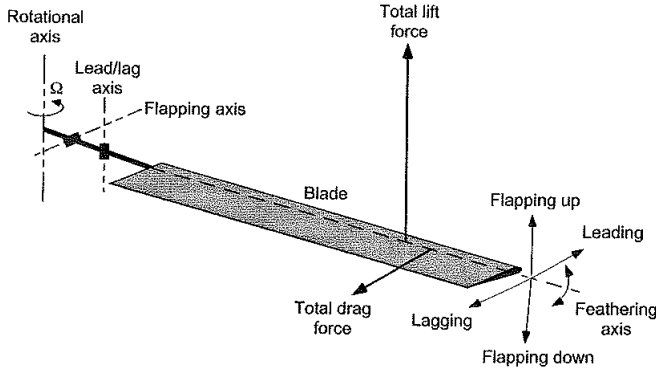


Figure 2.6: Rotor blade motion [19].

Feathering is the angular motion around the longitudinal axis of the blade and is caused by the aerodynamic moment acting on the blade around this axis. This motion will affect the blades aerodynamic angle of attack which is important for the flight dynamics of the multirotor. The feathering motion was not deemed important enough for the objectives of this project, considering the time it would take to model this accurately.

Blade flapping motion is caused by an uneven incident velocity distribution along the length of the blade which can be seen to the left in Figure 2.7. This will, in turn, cause an uneven lift force which is responsible for the flapping motion. To the right in Figure 2.7, it can be seen that during forward flight, the incident velocity normal to the propeller blade are no longer constant during a revolution. This means that the advancing and retreating blades will have non equal flapping angles which will slightly tilt the direction of the aerodynamic forces and moments.

Lagging motion is caused by the Coriolis force since the distance to the rotational axis for each blade element is changed when the the blade is flapping and rotating at the same time. Because of this motion, the center of gravity of the rotor can deviate from the rotational axis resulting in vibrations. The lagging motion doesn't affect the control of the multirotor according to Martínez [21] and will therefore not be modeled in this report.

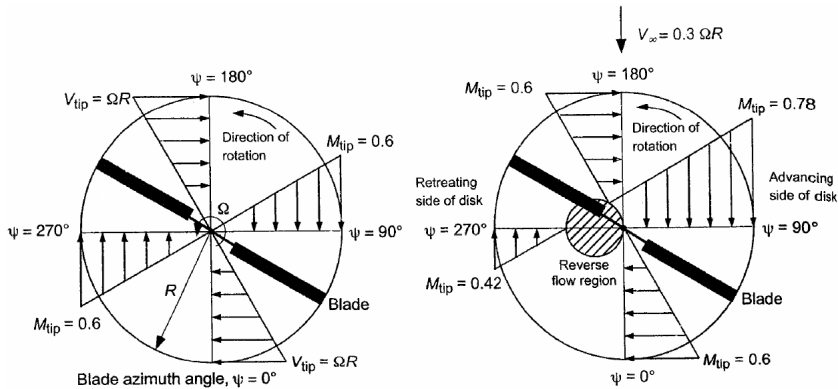


Figure 2.7: Incident velocity distribution in hover and forward flight [19].

### Simplified rotor model

There are several types of rotors that are designed to accommodate the described blade motions. For helicopters there are generally four types of rotors [19]:

- **Teetering rotor:** The teetering rotor uses a single hinge which is placed along the rotational axis, to accommodate the flapping and lagging motion. In addition, feathering bearings are used to allow cyclic and collective pitch capability which is needed for the roll and pitch actuation in helicopters.
- **Articulated rotor:** Articulated rotors use separate flapping and lagging hinges for each blade in addition to the feathering bearings.
- **Hingeless rotor:** Hingeless rotors uses flextures to accommodate the flapping and lagging in addition to the feathering bearings.
- **Bearingless rotor:** The motion of the blades in a bearingless rotor is solely controlled by bending, flexing and twisting the hub structure.

The roll and pitch actuation for multirotors are not controlled by cyclic and collective pitch which eliminates the need for feathering bearings. Multirotor rotors are also much smaller which reduces the structural demands. Multirotors generally use one of the three rotor types shown in Figure 2.8 where the flexural blade is the most commonly used option.

However, simulating a flexible blade is complicated and too time consuming for a project such as this. A simplified model is therefore needed. It was decided to use rigid rotor blades with spring loaded hinge offsets. The spring stiffness and the

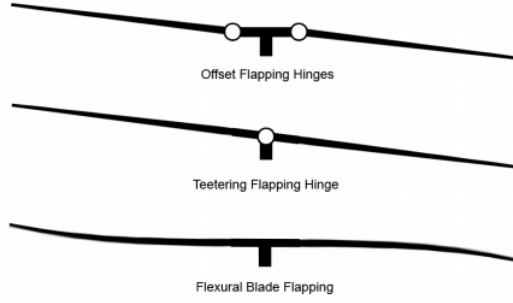


Figure 2.8: Rotor types generally used for multirotors [33].

hinge offset are then determined so that the characteristics match that of the real flexible blade. There have also been a number of other simplifications during this section such as neglecting the reverse flow region, which can be seen in Figure 2.7, the potential stalling of the propeller blades and the so called tip losses [19]. Additional simplifications will be described in Appendix C.2.

### Aerodynamic forces and moments

A rotor mainly generates three types of forces and moments while rotating; the thrust force, the horizontal force and the drag moment which can be seen in Figure 2.9. The thrust force  $T$  is acting perpendicularly to the *tip path plane* (TPP) whose boundary is described by the blade tips. The expressions for  $T$  can be seen in (2.13).

$$T = C_T \rho A R^2 \Omega^2 \quad (2.13)$$

The horizontal force  $H$  is the rotor drag force which is parallel to the TPP. The horizontal force is nonexistent during hover and axial flight. The expressions for  $H$  can be seen in (2.14).

$$H = C_H \rho A R^2 \Omega^2 \quad (2.14)$$

The drag moment  $Q$  is also acting perpendicularly to the TPP, but the direction is determined by the rotation of the rotor. The expressions for  $Q$  can be seen in (2.15).

$$Q = C_Q \rho A R^3 \Omega^2 \quad (2.15)$$

The nondimensional coefficients  $C_T$ ,  $C_H$  and  $C_Q$  depends on a number of different variables such as the inflow and advance ratios of the rotor, several parameters



that describe the geometry of the propeller, the flapping angles as well as the induced inflow velocity which will be discussed in Section 2.3. The expressions for the nondimensional coefficients have originally been developed for helicopters by Prouty [35] and was later modified by Martínez [21] to make them more suitable for multirotors. This was accomplished with the blade element theory which is explained in more detail in Appendix C.2.

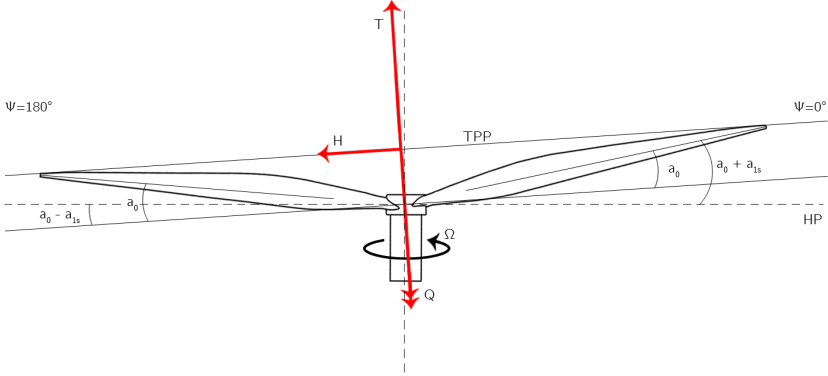


Figure 2.9: Thrust, horizontal force and drag moment acting on a flapping rotor.

The thrust, horizontal force and the drag moment are either parallel or perpendicular to the TPP, but ultimately we want to express the forces and moments produced by the rotor in a coordinate system which is aligned with the body frame of the multirotor, but has its origin in the resulting center of gravity of the rotor blades. This coordinate system will be called  $P_i, x, y, z$ . It is assumed that the CoG of the rotor blades remain at a fixed distance from the CoG of the entire multirotor.

To achieve the necessary force and moment transformations it is convenient to introduce yet another coordinate system. This coordinate system will also have its origin at the center of gravity for the rotor blades, but instead the x-axis will be aligned with the air velocity component contained in the hub plane (HP) which is perpendicular to the rotational axis. This coordinate system will be called  $P_i, x_w, y_w, z_w$ . The relation between these two newly introduced coordinate systems are defined by the sideslip angle  $\beta_{SS}$ , which can be seen in Figure 2.10.

As defined by Martínez [21], the relationship between the forces and moments, expressed in the different coordinate systems, are defined by the expressions in (2.16).

$$\begin{aligned} \mathbf{F}_i &= F_{xi}\mathbf{i} + F_{yi}\mathbf{j} + F_{zi}\mathbf{k} = -f_{xi}\mathbf{i}_w + f_{yi}\mathbf{j}_w - f_{zi}\mathbf{k}_w \\ \mathbf{M}_i &= M_{xi}\mathbf{i} + M_{yi}\mathbf{j} + M_{zi}\mathbf{k} = m_{xi}\mathbf{i}_w + m_{yi}\mathbf{j}_w + m_{zi}\mathbf{k}_w \end{aligned} \quad (2.16)$$

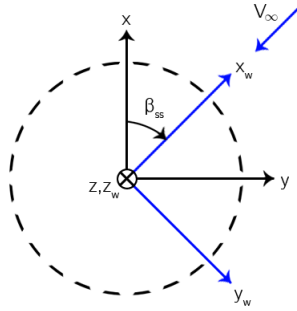


Figure 2.10: Definition of the sideslip angle.

The  $F$  and  $M$  variables corresponds to forces and moments expressed in  $P_i, x, y, z$  while  $f$  and  $m$ , which can be seen in Figure 2.11, corresponds to forces and moments expressed in  $P_i, x_w, y_w, z_w$ .

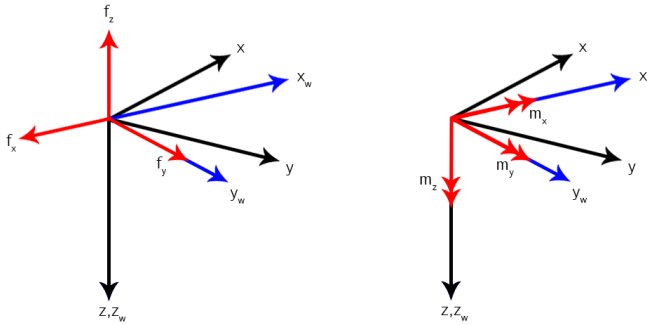


Figure 2.11: Aerodynamic forces and moments expressed in the coordinate system which is defined by the air velocity component contained in the HP.

The expressions in (2.17) are then obtained by combining the definition of the sideslip angle  $\beta_{SS}$  with (2.16)

$$\begin{cases} F_{xi} = -f_{xi} \cos \beta_{SSi} - f_{yi} \sin \beta_{SSi} \\ F_{yi} = -f_{xi} \sin \beta_{SSi} + f_{yi} \cos \beta_{SSi} \\ F_{zi} = -f_{zi} \end{cases} \begin{cases} M_{xi} = m_{xi} \cos \beta_{SSi} + m_{yi} \sin \beta_{SSi} \\ M_{yi} = m_{xi} \sin \beta_{SSi} + m_{yi} \cos \beta_{SSi} \\ M_{zi} = m_{zi} \end{cases} \quad (2.17)$$

The final step is to transform the thrust, horizontal force and drag moment to the  $P_i, x_w, y_w, z_w$  coordinate system which has been done by Martínez [21]. The relations can be seen in (2.18), where  $T$ ,  $H$  and  $Q$  are the absolute values of the thrust,

horizontal force and drag moment. the  $\pm$  sign is determined by the rotation of the rotor:

- $\pm = +$  if the rotor is turning counter clockwise.
- $\pm = -$  if the rotor is turning clockwise.

$$\begin{cases} f_x = H \cos a_{1s} + \frac{T \tan a_{1s}}{\sqrt{1 + \tan^2 a_{1s} + \tan^2 (\pm b_{1s})}} \\ f_y = \frac{T \tan (\pm b_{1s})}{\sqrt{1 + \tan^2 a_{1s} + \tan^2 (\pm b_{1s})}} \\ f_z = -H \sin a_{1s} + \frac{T}{\sqrt{1 + \tan^2 a_{1s} + \tan^2 (\pm b_{1s})}} \end{cases} \quad \begin{cases} m_x = -\frac{\pm Q \tan a_{1s}}{\sqrt{1 + \tan^2 a_{1s} + \tan^2 (\pm b_{1s})}} \\ m_y = \frac{\pm Q \tan (\pm b_{1s})}{\sqrt{1 + \tan^2 a_{1s} + \tan^2 (\pm b_{1s})}} \\ m_z = \frac{\pm Q}{\sqrt{1 + \tan^2 a_{1s} + \tan^2 (\pm b_{1s})}} \end{cases} \quad (2.18)$$

An overview of the rotor modeling can be seen in Figure 2.12, where the theory from this section has been implemented in Simulink.

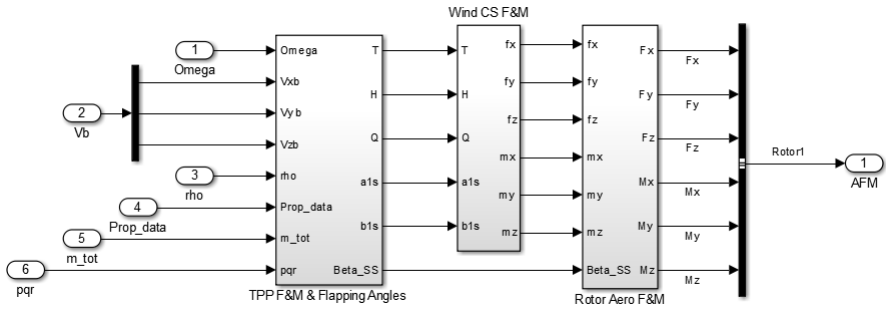


Figure 2.12: Schematic overview of the rotor modeling, implemented in Simulink.

## Induced inflow model

The aerodynamic forces and moments that are acting on the rotor blades have been derived in the previous section, but there is still one variable which cannot be determined by the blade element theory alone. During the derivation of the expressions in (2.13-2.15), Pruty [35] used Glauert's inflow model. This suggests a linear solution for the local induced inflow ratio, which can be seen in (2.19). In this equation,  $K_c$  is a constant that determines the slope of the inflow distribution and  $\lambda_i$  is the average induced velocity ratio, which is typically given by the uniform inflow solution from the momentum theory [19].

$$(\lambda_i)_{local} = \lambda_i \left( 1 + \frac{r}{R} K_c \cos \Psi \right) \quad (2.19)$$

The proposed strategy is to combine the two expressions for the thrust coefficient in (2.20), which have been derived in the Appendixes C.1 and C.2 for MT and BET respectively.

$$\begin{cases} C_T = \frac{C_{l\alpha}\sigma}{4} \left(1 - \frac{e}{R}\right) \left( \left(\frac{2}{3} + \mu^2\right) \theta_0 + \frac{1}{2}(1 + \mu^2) \theta_{tw} - \lambda \right) \\ C_T = 2(\lambda - \mu \tan \alpha) \sqrt{\mu^2 + \lambda^2} \\ \lambda = \lambda_c + \lambda_i \end{cases} \quad (2.20)$$

By doing so, a new equation (2.21) is obtained where the inflow ratio is the only unknown variable.

$$\lambda = \left( \left(\frac{2}{3} + \mu^2\right) \theta_0 + \frac{1}{2}(1 + \mu^2) \theta_{tw} \right) - \frac{8(\lambda - \mu \tan \alpha) \sqrt{\mu^2 + \lambda^2}}{\sigma C_{l\alpha} \left(1 - \frac{e}{R}\right)} \quad (2.21)$$

Equations for the inflow ratio are normally solved numerically and the approach that was used during this project is inspired by Leishman [19]. It was decided to use the *Newton-Rhapson method* because of the relatively fast convergence time, despite the necessity of a fairly accurate initial condition. The expression in Equation (2.22) is solved repeatedly until the error  $\varepsilon < 0.0005$  for which it is assumed that convergence has been reached.

$$\lambda_{n+1} = \lambda_n - \left[ \frac{f(\lambda)}{f'(\lambda)} \right]_n \quad \varepsilon = \left\| \frac{\lambda_{n+1} - \lambda_n}{\lambda_{n+1}} \right\| \quad (2.22)$$

The expressions for  $f(\lambda)$  and  $f'(\lambda)$  are derived from (2.21) and can be viewed in (2.23).

$$\begin{aligned} f(\lambda) &= \lambda - \left( \left(\frac{2}{3} + \mu^2\right) \theta_0 + \frac{1}{2}(1 + \mu^2) \theta_{tw} \right) + \frac{8(\lambda - \mu \tan \alpha) \sqrt{\mu^2 + \lambda^2}}{\sigma C_{l\alpha} \left(1 - \frac{e}{R}\right)} \\ f'(\lambda) &= 1 + \frac{8(\mu^2 + 2\lambda^2 - \lambda \mu \tan \alpha)}{\sigma C_{l\alpha} \left(1 - \frac{e}{R}\right) \sqrt{\mu^2 + \lambda^2}} \end{aligned} \quad (2.23)$$

The proposed method will determine the induced inflow ratio, but there are unfortunately some major limitations. The reason being that MT is based on the assumption that there is a well-defined airflow direction. This is not the case when there is an

upward velocity component  $-2v_i \leq V_\infty \sin \alpha \leq 0$  through the rotor disk, which typically happens during descent flight. According to Leishman there are four different types of working states during axial flight [19]:

- Normal working state.
- Vortex ring state (VRS).
- Turbulent wake state (TWS).
- Windmill brake state (WBS).

MT is only valid in the normal working state where the air flow is passing down through the rotor in a well defined slipstream, and in the Windmill Brake State where the air is flowing in the opposite direction. The air flow is very chaotic in between these two states and, hence, it is not possible to predict the induced inflow analytically during the vortex ring state or the turbulent wake state. Instead, a continuous approximation in the form of a quartic curve can be used [19]. This approximation, shown in Equation, (2.24), is based on a large number of experiments from flight tests and wind tunnel measurements, and it is valid for the entire range of  $-2v_i \leq V_\infty \sin \alpha \leq 0$ . In this equation,  $\kappa$  is the measured induced power factor and  $k_1 = -1.125$ ,  $k_2 = -1.372$ ,  $k_3 = -1.718$ ,  $k_4 = -0.655$ .

$$\frac{v_i}{v_h} = \kappa + k_1 \left( \frac{V_c}{v_h} \right) + k_2 \left( \frac{V_c}{v_h} \right)^2 + k_3 \left( \frac{V_c}{v_h} \right)^3 + k_4 \left( \frac{V_c}{v_h} \right)^4 \quad (2.24)$$

The approximated curve can be seen in Figure 2.13 together with the solution produced by the momentum theory. Note that there is a nonphysical solution to the MT which predicts the induced velocity fairly well until a certain limit where the quartic function drops off to meet the MT solution for descent flight.

In summary, the current working state has to be detected during the simulation. A suitable method for determining the inflow ratio is then decided i.e. the quartic curve is used in the range of  $-2v_i \leq V_\infty \sin \alpha \leq 0$ , while the MT and BET combination is used for the rest of the flight envelope. Momentum theory is used to test whether  $V_\infty \sin \alpha \geq -2v_i$  even if the solution for  $v_i$  isn't quite theoretically sound in the specified range.

## Rotor model validation

Although the structure of the rotor model is presented in previous section, there are still a few constants missing whose values depend on the design of the rotor.

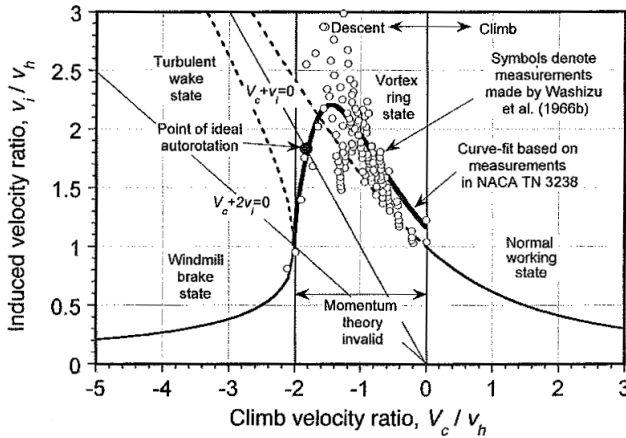


Figure 2.13: Solution for the induced velocity across the four working states [19].

To completely validate the proposed model a large number of experiments would be required, both in axial and forward flight. Because of the time constraints, it was decided to limit the scope of this thesis to only one type of propeller, the APC 10x4.7 Slowflyer [25] which can be seen in Figure 2.14.



Figure 2.14: Rendered picture of an APC 10x4.7 Slowflyer propeller, modeled in Solidworks [40].

This propeller has been used for the previous master thesis projects conducted at Combine Control Systems [31, 13] and its dimensions are suitable for this project as well. It was also decided to use experimental data for the nondimensional coefficients of thrust  $C_T$  and power  $C_P \equiv C_Q$  to further reduce the effort needed for this part of the project. This information is available at the UIUC Propeller Database from the University of Illinois [4]. Unfortunately this means that the rotor model will only be validated for axial flight. The experiments have been conducted for different angular velocities ranging from 420 – 680 rad/s while the propeller was exposed to winds of varying magnitudes. The corresponding inflow ratios  $\lambda_c = V/(\Omega R)$  were increased until zero thrust was generated, which for the APC 10x4.7 sf translated into roughly  $0.12 \text{ rad}^{-1}$ . The experimental setup can be seen in Figure 2.15.



Figure 2.15: Experimental setup for the wind tunnel test conducted by [5].

The UIUC Propeller Database [4] also provides geometrical data for the tested propellers. In Figure 2.16, the chord length is plotted as a function of the position along the length of the blade. Remember that the rotor has been modeled as having a constant chord length. The green line represents the true average of the chord length, while the red line is the chord length at 70% of the blade length which was used during the simulations. According to Martínez [21] it is common practice to use this value since it will be fairly representative for the whole blade, and thus leads to the most accurate results. The twist variation along the length of the blade can be seen in Figure 2.17. The green line represents the linearly fitted function while the red line represents the modified function which was tuned to get a better overall model accuracy.

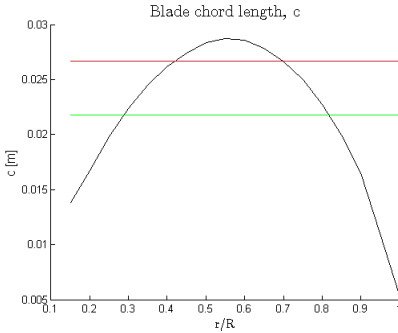


Figure 2.16: Chord length.

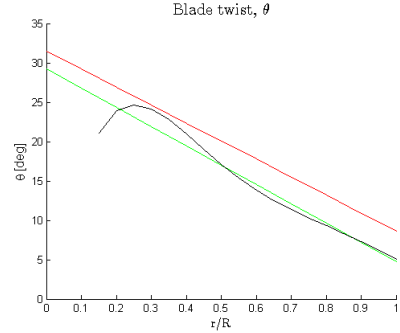


Figure 2.17: Blade twist.

There are several more propeller parameters that are needed for the proposed rotor model. All of the parameters are listed in Table 2.2 together with the values that were used during the simulations.

Parameter	Notation	Value	Unit
Chord length	$c$	0.0267	m
Linear slope of the propeller blade twist	$\theta_{tw}$	-0.4	rad
Propeller blade twist at the root of the blade	$\theta_0$	0.55	rad
Rotor radius	$R$	0.1270	m
Propeller mass	$m_p$	0.0116	kg
Blade moment of inertia around the flapping hinge	$I_{yb}$	$2.6275 \cdot 10^{-5}$	kgm <sup>2</sup>
Flapping hinge and blade center of gravity distance	$r_{Gb}$	0.0629	m
2-D lift-curve-slope of the airfoil section	$C_{l\alpha}$	$2\pi$	rad <sup>-1</sup>
Sectional drag coefficient	$C_d$	0.025	-
Torsional spring constant	$k_\beta$	1.14	Nm/rad

Table 2.2: Propeller parameters

$I_{yb}$  and  $r_{Gb}$  were determined from a CAD model, originally made by Nathan Kau [18], which is based on the geometrical dimensions provided by [4] as well as the weight of the propeller. The sectional drag coefficient was tuned based on the experimental data for  $C_Q$ . The torsional spring constant for the propeller  $k_\beta$  was determined by applying a vertical load  $F$  at the tip of a real APC 10x4.7Sf propeller blade while measuring the vertical deflection  $z$ . The spring constant was then calculated according to 2.25.

$$k_\beta = \frac{FR}{\arctan\left(\frac{z}{R}\right)} \left[ \frac{\text{Nm}}{\text{rad}} \right] \quad (2.25)$$

Interpolated values based on the experimental data have been divided by the values calculated by the proposed model to obtain compliance ratios for  $C_T$  and  $C_Q$ . These ratios can be viewed in Figure 2.18.

**Conclusions** The model has shown relatively satisfying results for the majority of the tested flight envelope. Some of the propeller parameters such as the linear twist coefficients had to be slightly tuned to improve the overall accuracy. The highly transient “notches” at around 525 and 420 rad/s are caused by irregularities in the interpolated data as well as a potential decrease in model accuracy for higher inflow ratios. The model accuracy is also seemingly decreased for rotational velocities above 650 rad/s which, considering the maximum recommended velocity of 680 rad/s, might be caused by structural phenomenas such as increased vibrations. The validation in this section doesn’t cover descent or forward flight, but it is assumed that the model is accurate enough to base further conclusions upon.



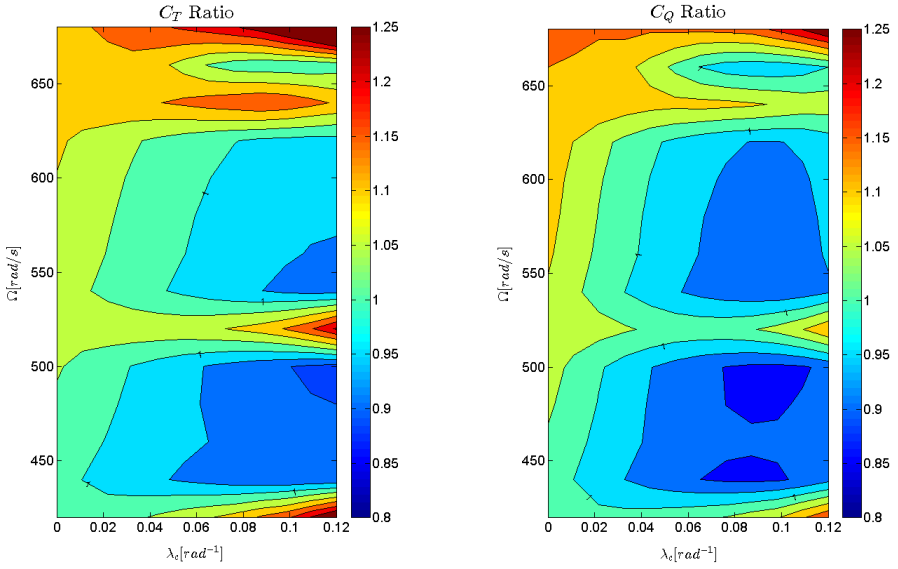


Figure 2.18: Rotor model validation for CT and CQ.

## 2.4 Airframe dynamics

Any rigid body that moves through a field of viscous fluid, such as gases or liquids, is affected by a fluid friction often known as drag force. This force is proportional to the squared velocity  $v$  of the onsetting fluid. Calculating the drag force acting on an arbitrary body is, however, a complicated task. The fluid exerts a pressure on the exposed reference surface  $A$ , which results in a net force on the body scaled by the drag coefficient  $C_d$ . In this thesis, the reference surface is seen as the projected surface area. To determine the drag force to full accuracy, complete knowledge of a body's projected surface area and drag coefficient in all directions must therefore be known. The general form of the drag equation is shown in (2.26).

$$F_d = \frac{1}{2} C_d \rho A v^2 \quad (2.26)$$

The onset of airflow resulting from a multirotor's movement through the air as well as from applied wind are the sources of aerodynamic drag. Realistically, rotational movement of the aircraft will also cause drag moments, but these will not be modeled here because of the calculation complexity. A relative airspeed  $V_\infty$  in the body frame, fully described by its magnitude together with its sideslip angle  $\beta_{SS}$  and angle of attack  $\alpha$ , will create a drag force according to (2.27). In (2.27),  $C_d$  is the drag coefficient and  $A$  is the projected surface area in the airspeed direction, which both

depend on the direction of  $V_\infty$ , i.e.  $\beta_{SS}$  and  $\alpha$ . Since the wind speed is described in the inertial frame, this velocity must first be transformed using the DCM matrix (2.1) before being added to the body frame velocity to create the relative airspeed  $V_\infty$ .

$$F_d = \frac{1}{2} \rho C_d(\beta_{SS}, \alpha) A(\beta_{SS}, \alpha) V_\infty^2 \quad (2.27)$$

Using the  $\beta_{SS}$  and  $\alpha$  angles, the force  $F_d$  in (2.27) can be described along the three body axes of the body frame as (2.28).

$$\mathbf{F}_d = \begin{cases} F_{dx} = F_d \cos \beta_{SS} \cos \alpha \\ F_{dy} = F_d \sin \beta_{SS} \cos \alpha \\ F_{dz} = F_d \sin \alpha \end{cases} \quad (2.28)$$

A multirotor airframe is typically quite complex, which makes it difficult to derive a general expression for the projected surface area  $A$  and the drag coefficient  $C_d$  for an arbitrary direction of  $V_\infty$ . Multiple arms and other parts partly obscuring each other depending on different  $\beta_{SS}$  and  $\alpha$  yields heavy geometrical calculations with many special cases. Considering this, some simplifications to how the projected surface area  $A$  is calculated from an arbitrary point of view is presented in (2.29), where the airframe may be seen as a rectangular cuboid with three different areas,  $A_x$ ,  $A_y$  and  $A_z$ . These areas are calculated in Appendix B and represent the surface areas in the principal body frame directions. This way, the areas may not be exactly correct, but at least an approximation is provided where the horizontal and vertical dimensions of the vehicle are given some representative relevance in regards to the wind direction. Anyhow, as will soon be discussed,  $C_d$  is highly uncertain, which decreases the importance of an absolutely accurate calculation of the surface area.

$$A \approx A_x \cos \beta_{SS} \cos \alpha + A_y \sin \beta_{SS} \cos \alpha + A_z \sin \alpha \quad (2.29)$$

The drag coefficient  $C_d$  is difficult to estimate even in the principal body frame directions  $x$ ,  $y$  and  $z$ . For it to be calculated accurately, CFD analysis or wind-tunnel testing is needed which are tools not available to this project. Even if they were, the situation is worsened by the fact that the coefficient is greatly affected by the spinning rotors' wake turbulence, possibly increasing the drag coefficient. It should also be noted that the airframe disrupts the inflow to the rotors, which could be viewed as additional drag. Accurately describing  $C_d$  is therefore not deemed possible in this thesis. However, testing the design for a range of reasonable values [42] gives an

indication of the importance of creating a streamlined airframe. In the simulator,  $C_d$  is assumed to be constant for every airflow direction.

The point of attack of  $\mathbf{F}_d$  will be in the centroid or the center of geometry  $\mathbf{C}$  from the relative airspeed's direction. It is a point calculated in similar fashion as the center of gravity, but using the projected two-dimensional areas in the airspeed direction instead. Since this point isn't necessarily located in the center of gravity  $\mathbf{G}$ , the force  $F_d$  will cause a rotation moment. The situation is described by Figure 2.19, which shows an arbitrary body from the airflow's point of view. The location of  $\mathbf{C}$  will be on the surface of the body, whereas  $\mathbf{G}$  will be inside. The angle  $\theta_d$  between  $\mathbf{F}_d$  and the distance vector  $\mathbf{r}_d$  will yield a distance component perpendicular to the surface, resulting in a drag moment. Viewing the problem from a cross section plane containing  $\mathbf{r}_d$  as in Figure 2.20, it is clear that there also is outward distance component that will not contribute toward any moment.

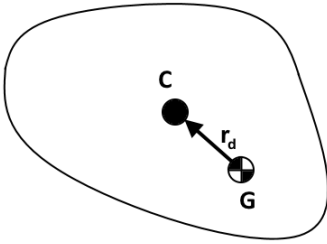


Figure 2.19: An arbitrary body seen from the airflow's point of view. The resulting drag force will act in the centroid  $\mathbf{C}$ , creating translational and rotational acceleration.

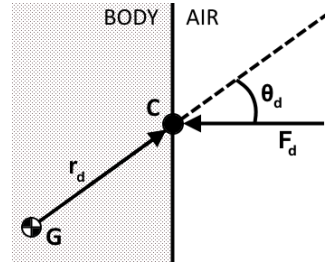


Figure 2.20: The distance of the centroid in relation to the center of gravity creates a lever for the drag force  $F_d$  resulting in a moment  $M_d$ .

Since the location of the centroid varies with the airspeed direction,  $\mathbf{r}_d = \mathbf{C} - \mathbf{G}$  will vary in magnitude and direction depending on  $\beta_{SS}$  and  $\alpha$ . A general description of the drag moment  $M_d$  is presented in (2.30).

$$\mathbf{M}_d = \mathbf{r}_d(\beta_{SS}, \alpha) \times \mathbf{F}_d \quad M_d = r_d(\beta_{SS}, \alpha) \sin \theta_d F_d \quad (2.30)$$

As previously explained, depending on the airspeed direction the location of the centroid will differ so  $\mathbf{C} = \mathbf{C}(\beta_{SS}, \alpha)$ . To simplify this matter, a similar approximation as for the surface area is performed here for the distance vector  $\mathbf{r}_d$ . This is then used to determine the moments  $\mathbf{M}_d$  in the simulator. The approximation is presented in (2.31), where  $\mathbf{r}_{dx}$ ,  $\mathbf{r}_{dy}$  and  $\mathbf{r}_{dz}$  are the distance vectors in each of the

body frame principal directions. How the centroid in each direction and the center of gravity  $\mathbf{G}$  are calculated is skipped here but is included in Appendix B.

$$\mathbf{r}_d \approx \mathbf{r}_{dx} \cos \beta_{SS} \cos \alpha + \mathbf{r}_{dy} \sin \beta_{SS} \cos \alpha + \mathbf{r}_{dz} \sin \alpha \quad (2.31)$$

To summarize, a number of simplifications have been made to the drag forces acting on the airframe. It should also be mentioned that possible lift force of the airframe has not been considered in the model, but is likely to be very small. The validity of the airframe model must be rated as relatively poor, especially in regards to the drag constant  $C_d$ . However, the main characteristics of wind will translate to forces and moments with relevant characteristics on the airframe. Even if the model has its flaws, it was still decided to include the drag force effect to obtain these characteristics in the simulator. Thus, the benefit of creating a streamlined and compact airframe may be shown.

## 2.5 Atmospheric model

For accurate description of external phenomena affecting multirotor flight, atmospheric conditions were modeled. This primarily concerned wind, but also variation in air density were considered. Since the thesis' main aim is to provide a multirotor design able to withstand windy conditions, a lot of attention was put into wind modeling. Using theory for wind characteristics presented in this section, specific wind scenarios were created to test different designs' ability to resist wind.

### Wind model

Wind is modeled as a stationary mean wind from a given direction to which gusts and turbulence are added according to (2.32). In the equation, the total wind is denoted  $v_w$  whereas its mean, gust and turbulence components are  $v_{wm}$ ,  $v_{wg}$  and  $v_{wt}$ . The wind modeling has largely been inspired by the work of Praceus' thesis work [34] and Mathworks content on aerospace modeling [23].

$$v_w = v_{wm} + v_{wg} + v_{wt} \quad (2.32)$$

The resulting wind from (2.32) is added to the ground speed of the multirotor to form the vehicle's relative airspeed in the inertial frame. Transforming it to the body frame yields  $V_\infty$ , which is used to obtain the aerodynamic forces and moments affecting the multirotor system.

**Wind gust model** A wind gust is a temporary increase in the mean wind speed. Its rate of increase is governed by the present wind speed, the vehicle airspeed and the

increase length of the gust. A gust is commonly modeled to have a "1-cosine" shape according to the the US Department of Defense Military Specification MIL-F-8785C [23]. The equation describing the gust is given by (2.33) where  $x$  is the distance into the gust,  $d_m$  the gust length and  $v_m$  the magnitude.

$$v_{wg} = \begin{cases} 0 & x < 0 \\ \frac{v_m}{2} \left( 1 - \cos \left( \frac{\pi x}{d_m} \right) \right) & 0 \leq x \leq d_m \\ v_m & x > d_m \end{cases} \quad (2.33)$$

Note that Equation (2.33) is not time-dependent and only describes the physical length of the gust. The duration of which an aircraft is exposed to the relative onset of a gust depends on the aircraft's current airspeed, where a faster airspeed will result in a quicker onset of the wind gust. Figure 2.21 shows a typical wind gust modeled with (2.33).

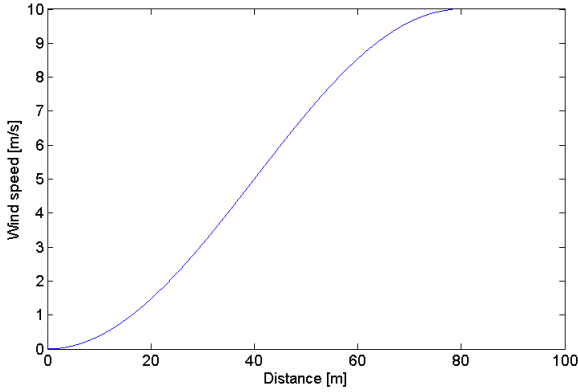


Figure 2.21: Wind gust with  $d_m = 80$  m and  $v_m = 10$  m/s.

**Dryden wind turbulence** The Dryden wind turbulence model is used to predict wind velocity turbulence, following the Military Specification MIL-F-8785C from the US Department of Defense [23]. The model takes *white noise* as an input and may be seen as a wide-sense stationary stochastic process, i.e. it is time-invariant. White noise is a completely uncorrelated stochastic process with equal PSD magnitude for the entire frequency range. The power spectral density (PSD) functions for the Dryden model (2.34) define the contributions towards the turbulence across the frequency range. The functions describe the spectral density for a given height  $h$ , mean-wind relative airspeed  $V$  as well as a specific wind speed 6 m (20 ft) above the ground  $W_{20}$ .

$$\begin{aligned}
 \Phi_u(\omega) &= \frac{2\sigma_u^2 L_u}{\pi V} \frac{1}{1 + \left(L_u \frac{\omega}{V}\right)} \\
 \Phi_v(\omega) &= \frac{\sigma_v^2 L_v}{\pi V} \frac{1 + 3 \left(L_v \frac{\omega}{V}\right)^2}{\left(1 + \left(L_v \frac{\omega}{V}\right)^2\right)^2} \\
 \Phi_w(\omega) &= \frac{\sigma_w^2 L_w}{\pi V} \frac{1 + 3 \left(L_w \frac{\omega}{V}\right)^2}{\left(1 + \left(L_w \frac{\omega}{V}\right)^2\right)^2}
 \end{aligned} \tag{2.34}$$

There are also PSD functions describing rotational wind velocity disturbances  $p$ ,  $q$  and  $r$ , resulting from an uneven wind distribution over the vehicle's body. Only the linear components in the  $u$  (longitudinal),  $v$  (lateral) and  $w$  (vertical) directions will, however, be modeled in this project. This simplification is made because the turbulence magnitudes of these are small and a small scale multirotor will be exposed to approximately the same wind over its airframe.

The parameters  $\sigma_i$  and  $L_i$ , where  $i = u, v, w$ , in (2.34) are the turbulence intensities and scale lengths. According to the MIL-F-8785C specifications, these can be calculated as (2.35) for altitudes below 300  $m$ , which will most likely cover the operating range of the UAVs studied and designed in this thesis.

$$\begin{aligned}
 L_w &= h & L_u &= L_v = \frac{h}{(0.177 + 0.000823)^{1.2}} \\
 \sigma_w &= 0.1W_{20} & \sigma_u &= \sigma_v = \frac{\sigma_w}{(0.177 + 0.000823)^{0.4}}
 \end{aligned} \tag{2.35}$$

To generate the turbulence, the transfer functions below 2.36 are fed with zero mean unit variance white noise. The turbulence obtained from the Dryden transfer functions are then added to the constant wind components to generate the total wind. Transfer functions  $H(i\omega)$  are related to their corresponding PSD functions  $\Phi(\omega)$  through  $\Phi(\omega) = |H(i\omega)|^2$ . This property has been used to obtain (2.36).

$$\begin{aligned}
H_u(s) &= \sigma_u \sqrt{\frac{2L_u}{\pi V}} \frac{1}{1 + \frac{L_u}{V}s} \\
H_v(s) &= \sigma_v \sqrt{\frac{L_v}{\pi V}} \frac{1 + \frac{\sqrt{3}L_v}{V}s}{\left(1 + \frac{L_u}{V}s\right)^2} \\
H_w(s) &= \sigma_w \sqrt{\frac{L_w}{\pi V}} \frac{1 + \frac{\sqrt{3}L_w}{V}s}{\left(1 + \frac{L_w}{V}s\right)^2}
\end{aligned} \tag{2.36}$$

### Air density

Air density for a given altitude is calculated using the COESA 1976 atmospheric model included in the Simulink Aerospace toolbox. It has no greater effect on the model since the quantity varies very slowly, especially when flight is conducted at a small range of altitudes. More information regarding atmospheric conditions according to the COESA 1976 standard can be found in [45].

# 3

## Control

In order to achieve the desired positional control, a suitable control algorithm must be implemented in the simulator. The development of this will be the main focus of this chapter, resulting in a proposed control structure along with a linear analysis of the closed-loop system. In addition, the controller's ability to reject external disturbances will be discussed. The design and analysis performed in this chapter follows the conventions and methods presented by Glad and Ljung [15].

### 3.1 Overview

The closed-loop problem of controlling the multirotor system through feedback can be visualized as in Figure 3.1. It is clear that there are no direct means of actuating the horizontal positions  $x$  and  $y$  directly. Since positional control is desired, the angular subsystem must be controlled by a positional controller in such a way that a desired position can be reached.

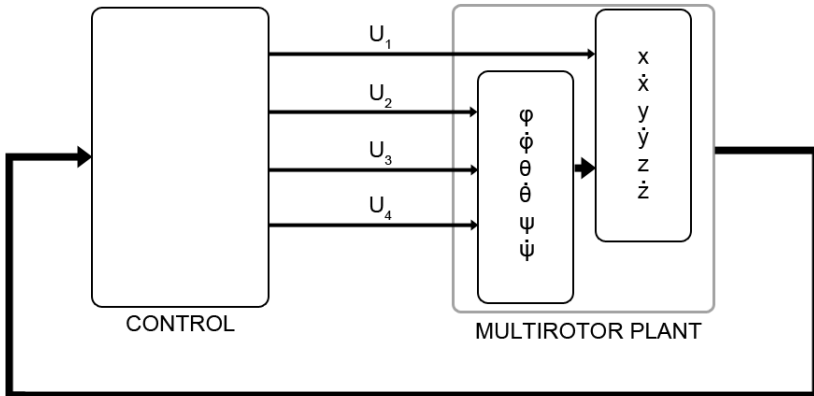


Figure 3.1: The closed-loop multirotor system.

The state vector  $\mathbf{x}$  of the multirotor system is given below in (3.1). These states correspond to translation and rotation described in the inertial frame. The control



signal vector  $\mathbf{U}$  to influence these states is shown in (3.2). Its contents correspond to the thrust force  $U_1$  as well as actuated roll, pitch and yaw moments,  $U_2$ ,  $U_3$  and  $U_4$ .

$$\mathbf{X} = [x \quad \dot{x} \quad y \quad \dot{y} \quad z \quad \dot{z} \quad \phi \quad \dot{\phi} \quad \theta \quad \dot{\theta} \quad \psi \quad \dot{\psi}]^T \quad (3.1)$$

$$\mathbf{U} = [U_1 \quad U_2 \quad U_3 \quad U_4]^T \quad (3.2)$$

Using the vectors in (3.1) and (3.2), the multirotor system in the inertial frame can be described compactly on the form (3.3). The full state-space equations for the system was previously described in Section 2.1, of which some simplifications will be made for the controller design.

$$\dot{\mathbf{X}} = f(\mathbf{X}, \mathbf{U}) \quad (3.3)$$

A generalized control problem can be schematically viewed as in Figure 3.2, with a generalized control law according to (3.4). Apart from the reference signal  $r$ , there are other input signals to the system representing different types of disturbances — input disturbance  $d_u$  and measurement disturbance  $n$ . External forces and moments due to aerodynamic flight effects enter the system as  $d_u$  and will be of central interest for this thesis. For satisfactory flight, it is important that these are sufficiently attenuated by the controller.

$$u(t) = F_r r(t) - F_y y(t) \quad (3.4)$$

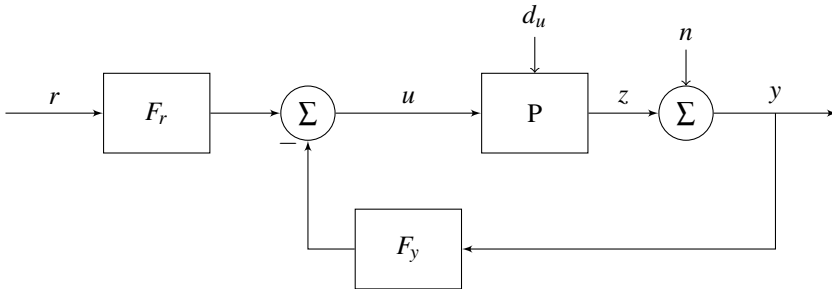


Figure 3.2: A generalized control problem.

In this generalized control problem, the process output  $z$  is defined by a series of transfer functions that map each input to  $z$ . The relation is shown in (3.5) with

relevant closed-loop transfer functions defined in (3.6). The transfer function  $G_{cl}$  describes the response from  $r$  to the  $z$ , whereas  $S_u$ , known as the *input sensitivity function*, describes the response from  $d_u$  to  $z$ . For effective attenuation of input disturbance  $d_u$ ,  $S_u$  should be made as small as possible across all frequencies in the Laplace domain.

$$z(t) = G_{cl}r(t) + S_u d_u(t) - Tn(t) \quad (3.5)$$

$$\begin{aligned} G_{cl} &= \frac{PF_r}{1 + PF_y} = T \frac{F_y}{F_r} & S_u &= \frac{P}{1 + PF_y} = PS \\ S &= \frac{1}{1 + PF_y} & T &= \frac{PF_y}{1 + PF_y} \end{aligned} \quad (3.6)$$

In (3.6), the  $S$  is the *sensitivity function* and  $T$  the *complementary sensitivity function*. The measurement disturbance  $n$  is mapped to  $z$  by  $T$ , whereas  $S$  maps  $n$  to the measured output  $y$ . Obviously,  $S_u = S = T = 0$  would be desirable, but will not be possible due to physical constraints and the limitation  $S + T = 1$ . Generally,  $S$  is kept low at low frequencies and  $T$  kept low at high frequencies to achieve desirable disturbance rejection and robustness to model uncertainty. More information on this topic can be read in Glad and Ljung [15].

In the proceeding control analysis, only the influence of the input disturbance  $d_u$  will be analyzed. This thesis work is performed at a conceptual level and therefore doesn't concern the real-world implementation aspect of sensor measurement noise. Thus, modification of  $G_{cl}$  and  $S_u$  to achieve satisfactory reference tracking and rejection of input disturbance are the main aims of the controller design.

## 3.2 PID control

The abbreviation PID stems from that the controller type employs proportional (P), integral (I) and derivative (D) control action. It is one of the most conventional and proven control strategies around and often proves sufficient in many applications. The controller aims to minimize the control error  $e(t)$  presented in (3.7). The signal  $r(t)$  constitutes the desired process output, also known as the *reference signal*, whereas  $y(t)$  is commonly known as the *measurement signal* and is the measured output from the system.

$$e(t) = r(t) - y(t) \quad (3.7)$$

The standard PID controller can be represented as shown below in (3.8). The constants  $K_P$ ,  $K_I$ ,  $K_D$  are chosen, or "tuned", to obtain satisfactory closed-loop response and performance.

$$u(t) = K_P e(t) + K_I \int e(t) dt + K_D \frac{d}{dt} e(t) \quad (3.8)$$

### Cascaded control

The multirotor system can be seen as two subsystems, one rotational (inner) and one translational (outer), and the cascaded control structure proposed in this section is therefore well-suited. PD controllers are designed to control the attitude ( $\phi$  and  $\theta$ ), whereas PID controllers are employed to control the position ( $x$ ,  $y$  and  $z$ ) as well as the yaw angle ( $\psi$ ). The proposed structure of the cascaded controller can be viewed in Figure 3.3.

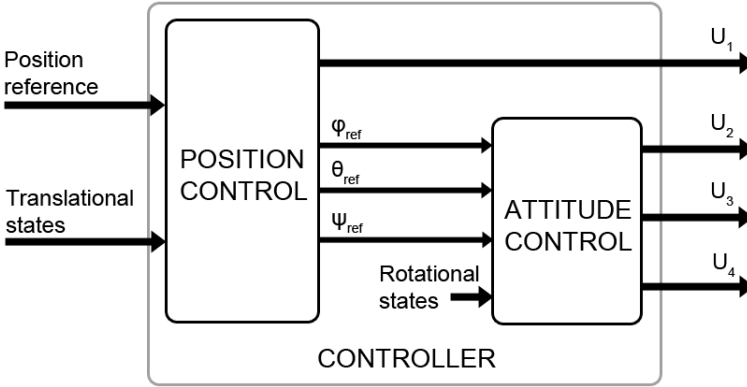


Figure 3.3: The cascaded PID control structure.

Viewing the system as an inner and outer control loop simplifies linear control analysis. When adjusting a cascaded PID controller one starts with the inner loop, which in this case is the rotational subsystem. It is tuned to desired performance. Moving on to the outer loop, which here is the translational control loop, its speed (time constant or bandwidth) will be limited by the inner loop. It is common practice to make it a factor  $N$  times slower than the inner loop, which makes it possible to view the inner loop as static from the outer loop's perspective. It was decided that the factor  $N$  will be at least four for the multirotor controller case.

### Attitude control

When designing the controller for the rotational loop and analyzing the system response, simplifications are made to the dynamical system in order to decouple the

control signals and to remove nonlinear terms. Thus, linear analysis can be applied instead of more complex analysis. The rotational velocity in the body and inertial frames are approximated as equal, i.e.  $[\dot{\phi} \ \dot{\theta} \ \dot{\psi}]^T \approx [p \ q \ r]^T$ , which has most validity at low rotational velocities. This is most common in near-hover flight. The simplified control model is presented in (3.9), in which  $U_2$ ,  $U_3$  and  $U_4$  constitute the moment control signals, and  $\tau_{aero}$  are the corresponding moment disturbances due to aerodynamic effects.

$$\begin{cases} \ddot{\phi} = \frac{1}{I_{XX}} U_2 + \frac{1}{I_{XX}} \tau_{aero}^{\phi} \\ \ddot{\theta} = \frac{1}{I_{YY}} U_3 + \frac{1}{I_{YY}} \tau_{aero}^{\theta} \\ \ddot{\psi} = \frac{1}{I_{ZZ}} U_4 + \frac{1}{I_{ZZ}} \tau_{aero}^{\psi} \end{cases} \quad (3.9)$$

**Roll and pitch control** The attitude control laws designed to control the  $\phi$  and  $\theta$  angles of the rotational subsystem are expressed in (3.10), where the error  $e(t)$  is the angle error. The derivative part has been modified, compared to a standard PD controller, to act as pure damping of the system. The control output  $u(t)$  is seen as an angular acceleration and is therefore multiplied by the moment of inertia around the appropriate axis to get the associated control moment. Since the positional PID controllers generate angle references for for the roll and pitch controllers, integral action was not deemed necessary to control these angles.

$$u(t) = K_P e(t) - K_D \frac{d}{dt} y(t) \quad (3.10)$$

In the Laplace domain, the transfer functions from reference and process disturbance to the output angle is shown for  $\phi$  in (3.11). These are analogous to the transfer functions for  $\theta$ . It is clear that two poles are present, which must be have negative real parts for the system to be stable.

$$\begin{aligned} \Phi(s) &= G_{cl}^{\phi}(s) \Phi_{ref}(s) + S_u^{\phi}(s) \tau_{aero}^{\phi}(s) \\ G_{cl}^{\phi}(s) &= \frac{K_P^{\phi}}{s^2 + K_D^{\phi} s + K_P^{\phi}} \Phi(s) & S_u^{\phi}(s) &= \frac{1}{I_{XX}} \frac{1}{s^2 + K_D^{\phi} s + K_P^{\phi}} \end{aligned} \quad (3.11)$$

The parameters in the proposed control laws in (3.10) are tuned such that the two system poles  $p_1$  and  $p_2$  in (3.11) are placed on the real axis and in the same point in the complex plane, so  $p = p_1 = p_2$ . To achieve this pole placement, the PD parameter expressions  $K_P^{\phi} = p^2$  and  $K_D^{\phi} = -2p$  are used. In Figure 3.4, step responses from

reference and disturbance signals can be viewed for controllers tuned for different performance. The blue line shows the response for poles placed in  $p = -10$ , green for  $p = -15$  and red for  $p = -20$ . The black dashed line shows the reference.

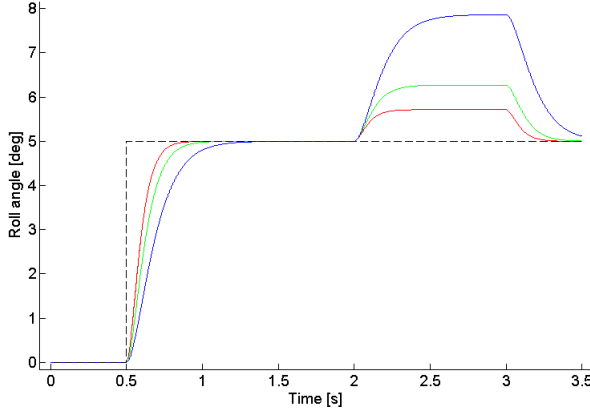


Figure 3.4: Roll/pitch reference and process disturbance step response for three different PD control settings. After 0.5 seconds, a reference step of 5 degrees is made. After two seconds, a moment input disturbance step of  $\tau_{aero}^{\phi} = 0.1$  Nm is made during one second on a multirotor with  $I_{XX} = 0.04$  kgm<sup>2</sup>.

As can be seen from Figure 3.4, there will be a steady state error due to the disturbance that a PD controller can not perfectly compensate for. The controller tuned with highest gain will have a faster reference response as well as significantly smaller error due to the disturbance. Another way of viewing the closed-loop performance is by looking at the Bode diagram of  $G_{cl}^{\phi\theta}$  and  $S_u^{\phi\theta}$ . The Bode diagrams can be viewed in Figures 3.5 and 3.6, where it can be seen that the faster controller yields a higher cut-off frequency in  $G_{cl}^{\phi\theta}$  and lower steady state gain in  $S_u^{\phi\theta}$ .

Although a faster control loop shows beneficial results, increasing it too much is ill-advised since it is limited by the speed of the motors. Because of this, it is concluded to tune the controller such as the closed-loop response of the rotational loop is at least a factor  $N$  times slower than the motor response, using similar reasoning as discussed for cascaded control loops. Thus, from the rotational loop's point of view, the motor dynamics may be seen as a static gain achieving a desired rotational speed instantaneously.

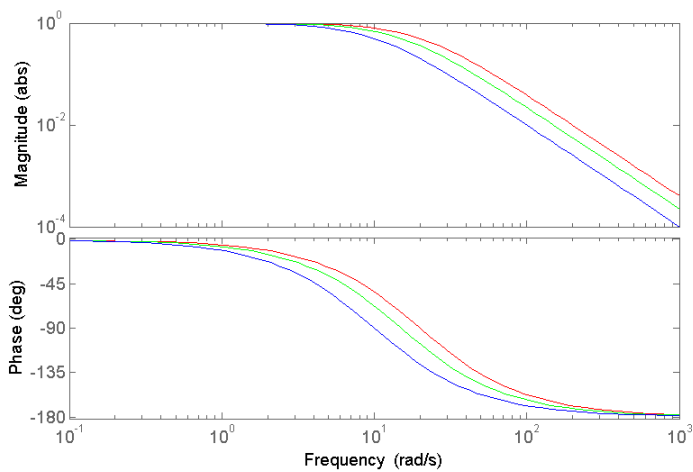


Figure 3.5: Bode plot of the  $G_{cl}^{\phi\theta}$  transfer function for roll/pitch with different controller settings.

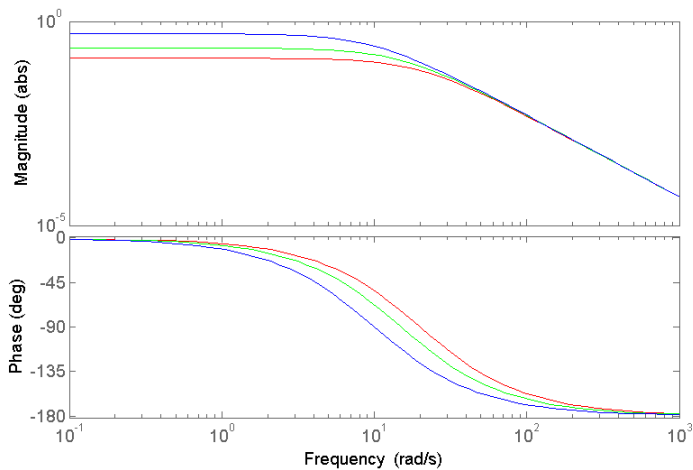


Figure 3.6: Bode plot of the  $S_u^{\phi\theta}$  transfer function for roll/pitch with different controller settings.

**Yaw control** In the proposed control structure, the position is controlled without use of the yaw angle  $\psi$ . It must, however, be stabilized to ensure flight performance. To achieve this, integral action must be employed since for this angle there is no outer controller generating references. Unwanted moment disturbance  $\tau_{aero}^\psi$  will, hence, create a steady state error. Such moments may come from the fact that in a real setting the motors and propellers may not be perfectly identical or they may experience local variations in conditions. For a coaxial rotor configuration the propellers above and below will produce different counter-moments on the air frame, which will create a situation where integral action is sorely needed. Thus, the yaw angle will be controlled by a PID controller (3.12), with  $U_4 = I_{ZZ}u(t)$ .

$$u(t) = K_P e(t) + K_I \int e(t) dt - K_D \frac{d}{dt} y(t) \quad (3.12)$$

Using this controller, the resulting transfer functions for the yaw system are presented in (3.13). The introduction of integral action introduces an additional pole, but since also a control constant  $K_I^\psi$  is added, pole-placement techniques may again be used to tune the system.

$$\begin{aligned} \Psi(s) &= G_{cl}^\psi(s) \Psi_{ref}(s) + S_u^\psi(s) \tau_{aero}^\psi(s) \\ G_{cl}^\psi(s) &= \frac{K_P^\psi s + K_I^\psi}{s^3 + K_D^\psi s^2 + K_P^\psi s + K_I^\psi} \Psi(s) \quad S_u^\psi(s) = \frac{1}{I_{ZZ}} \frac{s}{s^3 + K_D^\psi s^2 + K_P^\psi s + K_I^\psi} \end{aligned} \quad (3.13)$$

Arbitrarily placing the three poles yields the control parameters  $K_P = p_1 p_2 + p_1 p_3 + p_2 p_3$ ,  $K_I = -p_1 p_2 p_3$  and  $K_D = -p_1 - p_2 - p_3$ . The pole locations are chosen according to a *dominant pole placement* technique [46], where two poles are placed closer to the imaginary axis in the complex plane such that  $p_2 = p_1$ ,  $p_3 = 5p_1$ . The performance will thus mainly be defined by the two dominant poles  $p_1$  and  $p_2$ , somewhat approximating the system to second order with reduced overshoot. Figure 3.7 shows the reference and disturbance step responses for the yaw system with controllers designed for poles in  $p_1 = -1$  (blue line),  $p_1 = -2$  (green line) and  $p_1 = -3$  (red line). The dashed black line is the reference value.

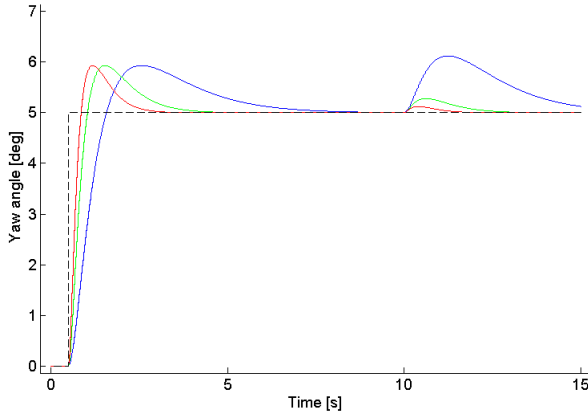


Figure 3.7: Yaw reference and disturbance step response for three different PID control settings. After 0.5 seconds, a reference step of 5 degrees is made. After 10 seconds, a moment input disturbance step of  $\tau_{aero}^{\psi} = 0.1$  Nm is made on a multirotor with  $I_{ZZ} = 0.08$  kgm<sup>2</sup>.

The Bode plots for the  $G_{cl}^{\psi}$  and  $S_u^{\psi}$  transfer functions can be viewed in Figures 3.8 and 3.9. Relating these to the step response plot (Figure 3.7), it is clear that the best performing controller has higher cut-off frequency (and hence faster response) as well as lower closed-loop gain for disturbances across the frequency range.

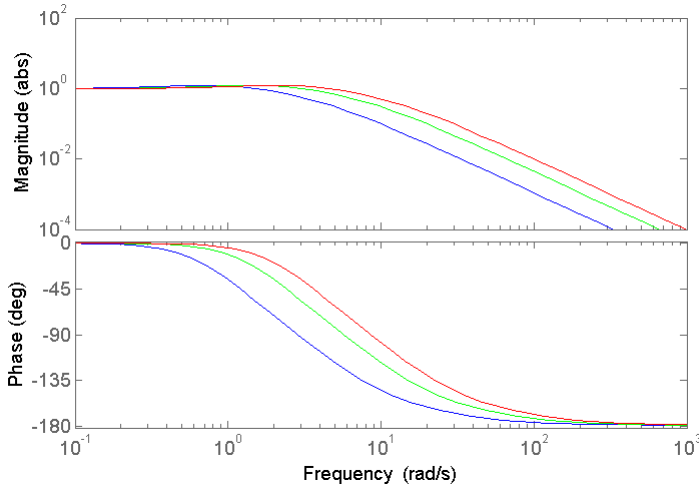


Figure 3.8: Bode plot of the  $G_{cl}^{\psi}$  transfer function for yaw with different controller settings.



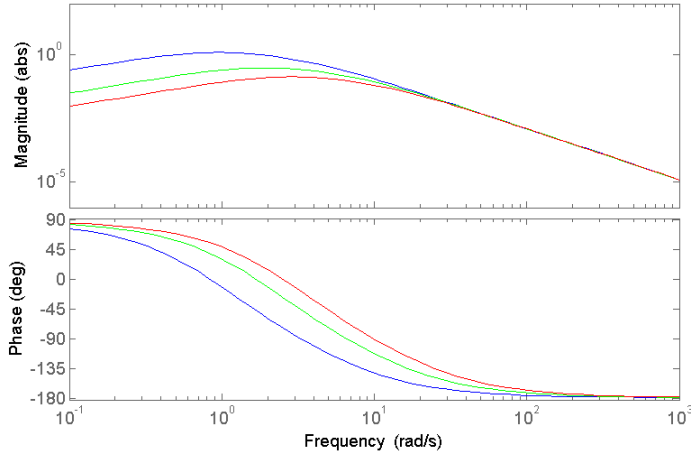


Figure 3.9: Bode plot of the  $S_u^\psi$  transfer function for yaw with different controller settings.

As for roll and pitch, the yaw controller can not be made arbitrarily fast. It must adhere to the constraints set by the motor actuators. The yaw reference will be zero in the proposed control setup since only the roll and pitch angles will be used for position control. Hence, the yaw controller will be tuned to provide at least a two times slower response than for the prioritized control of the roll and pitch angles.

### Position control

When considering the outer translational loop, similar model simplifications as for attitude are made to obtain the linear system (3.14). These simplifications yield a model that doesn't accurately describe all flight conditions, but may still be used for control analysis to give an indication of the closed-loop response characteristics. Simplifications include small angle approximations as well as neglecting the coupling between angular and translational velocity. This is done in order to decouple the control of the angular references.

$$\begin{cases} \ddot{x} = -\theta \frac{1}{m} U_1 + \frac{1}{m} F_{aero}^x \\ \ddot{y} = \phi \frac{1}{m} U_1 + \frac{1}{m} F_{aero}^y \\ \ddot{z} = g + \frac{1}{m} U_1 + \frac{1}{m} F_{aero}^z \end{cases} \quad (3.14)$$

The PID controllers designed to control the translational subsystem have the famil-

iar expression in (3.15), where the error  $e(t)$  is the position error. To ensure that no steady state position errors will be present, integral action of the controller is essential. Again, the derivative part has been modified to act as pure damping of the system.

$$u(t) = K_P e(t) + K_I \int e(t) dt - K_D \frac{d}{dt} y(t) \quad (3.15)$$

**Horizontal control** In horizontal control, reference tracking of desired  $x$  and  $y$  positions are considered. From the outer control loop's perspective the inner loop is static, achieving a desired attitude instantaneously. The controller output of the horizontal flight provides references for the pitch and roll controllers. The analysis in this section will be for control of the  $x$  position, but may be applied analogously to  $y$ .

Since there is no way to actuate the horizontal position directly, the control is dependent on the available thrust  $U_1$  and current attitude. To simplify analysis, the thrust will be approximated for near-hover flight as  $U_1 \approx mg$ . Since the horizontal position control sends angle references to the roll and pitch controllers, the input to the inner subsystem is  $\theta = u(t)/g$ .

$$\begin{aligned} X(s) &= G_{cl}^x(s) X_{ref}(s) + S_u^x(s) F_{aero}^x(s) \\ G_{cl}^x(s) &= \frac{K_P^x s + K_I^x}{s^3 + K_D^x s^2 + K_P^x s + K_I^x} \quad S_u^x(s) = \frac{1}{m} \frac{s}{s^3 + K_D^x s^2 + K_P^x s + K_I^x} \end{aligned} \quad (3.16)$$

The PID parameters are chosen such that all poles are placed on the real axis to prevent oscillation. For a given set of poles, the parameters are  $K_P = p_1 p_2 + p_1 p_3 + p_2 p_3$ ,  $K_I = -p_1 p_2 p_3$  and  $K_D = -p_1 - p_2 - p_3$ . Two poles  $p_1$  and  $p_2$  are placed in the same location and are the ones that have greatest impact on the response time. The last pole is placed a factor 5 further into the left half of the complex plane, which reduces the overshoot and makes the closed-loop system behave somewhat like a second order system. This dominant pole placement approach is similar to the one adopted for yaw control. In Figure 3.10, the reference and disturbance step responses are shown for three control settings. These controllers correspond to  $p_1 = -0.5$  (blue line),  $p_1 = -1$  (green line) and  $p_1 = -2$  (red line). The black dotted line is the reference signal.

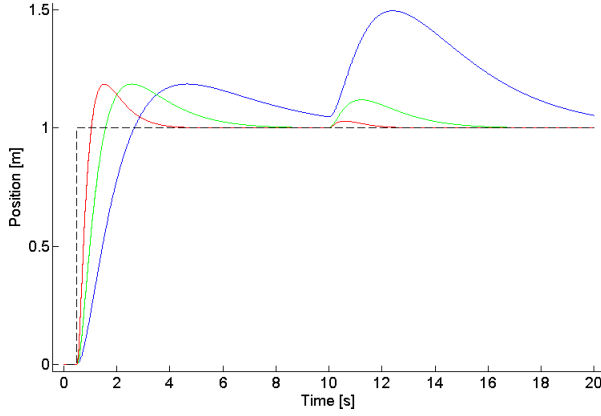


Figure 3.10: Position reference and disturbance step response for three different PID control settings. After 0.5 seconds, a reference step of 1 m is made. After 10 seconds, a force input disturbance step of  $F_{aero}^x = 1$  N is made on a multirotor with  $m = 1.2$  kg.

Analyzing the Bode diagrams in Figure 3.11 and 3.12 for these controller settings clearly shows differences in bandwidth and disturbance attenuation evident in the step responses from Figure 3.10.

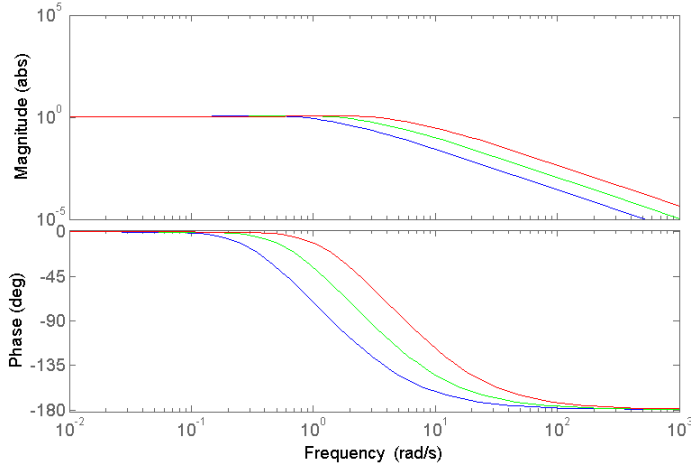


Figure 3.11: Bode plot of the  $G_{cl}^{xy}$  transfer function for  $x$  position with different controller settings.

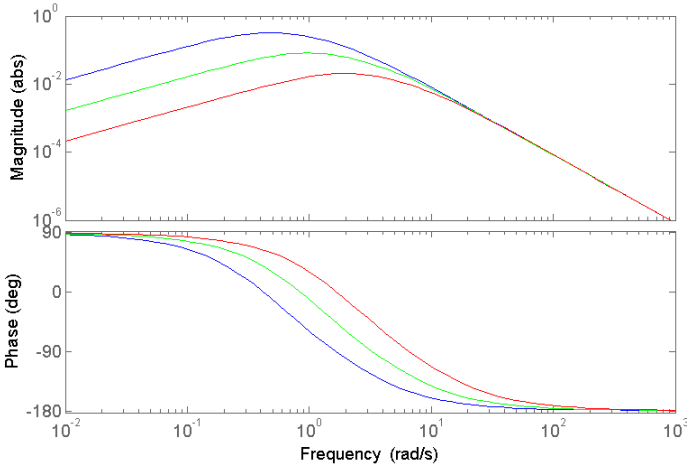


Figure 3.12: Bode plot of the  $S_u^x$  transfer function for  $x$  position with different controller settings.

**Altitude control** Starting with the linear expression for the altitude  $z$  in (3.14), system analysis is performed in similar fashion as for horizontal control. The PID controller is designed as before (3.15) and related to the system input  $U_1$  by  $U_1 = m(u(t) - g)$ . This way, the same transfer function structure as for the horizontal control is obtained for altitude (3.17). Note that the gravitational acceleration  $g$  is subtracted from the control signal since  $z$  points "downward" according to aerospace standards [1].

$$\begin{aligned} Z(s) &= G_{cl}^z(s)Z_{ref}(s) + S_u^z(s)F_{aero}^z(s) \\ G_{cl}^z(s) &= \frac{K_P^z s + K_I^z}{s^3 + K_D^z s^2 + K_P^z s + K_I^z} \quad S_u^z(s) = \frac{1}{m} \frac{s}{s^3 + K_D^z s^2 + K_P^z s + K_I^z} \end{aligned} \quad (3.17)$$

The system is tuned according to the same principles as for the horizontal system, making use of pole-placement technique, and will have an identical response in this linear approximation. Thus, step responses and Bode diagrams may be omitted here and Figures 3.10, 3.11 and 3.12 for the horizontal system may be applied to this altitude analysis as well.

When the controller is implemented in the multirotor system, an anti-windup scheme is employed to handle the problem of integrator windup due to saturation in attainable thrust. The limits are  $[0, T_{max}]$ , where the zero is obvious since rotors with fixed blades can not be controlled to provide any downward force.  $T_{max}$  is not

as straightforward since the available thrust will depend on the flight regime. The used anti-windup scheme is known as *back-calculation* [38], which subtracts the difference between the desired and actual control signal from the integral part of the control. Undesired effects when re-entering the non-saturated area are reduced or avoided that would otherwise cause large overshoots.

### 3.3 Control allocation

To actuate the system, the four physical control signals  $U_1$ ,  $U_2$ ,  $U_3$  and  $U_4$ , representing desired thrust force and moments (roll, pitch and yaw) respectively, must be recalculated to corresponding rotor speeds and voltages. These signals are stored in the control signal vector  $\mathbf{U}$  and are related to the squared rotor speeds  $\Omega^2$  according to (3.18). The matrix  $\mathbf{A}$  is here presented for the quadrotor case of two rotors ( $i = 1, 3$ ) spinning clockwise and two counter-clockwise ( $i = 2, 4$ ) with individual rotor speeds  $\Omega_i$ . In  $\mathbf{A}$ , the coefficients  $b = C_T \rho A R^2$  and  $d = C_Q \rho A R^3$  are the thrust and drag coefficients (which vary with the current flight conditions, see Section 2.3), whereas  $l$  is the arm length. Here, it is important to remember that the forces and moments are defined according to a coordinate system where the vertical axis points "downwards" [1].

$$\mathbf{U} = \begin{bmatrix} U_1 \\ U_2 \\ U_3 \\ U_4 \end{bmatrix} = \mathbf{A} \Omega^2 \quad \mathbf{A} = \begin{bmatrix} -b & -b & -b & -b \\ bl & bl & -bl & -bl \\ bl & -bl & -bl & bl \\ -d & d & -d & d \end{bmatrix} \quad (3.18)$$

The equation system (3.18) can be inverted in the quadrotor case to obtain the corresponding squared propeller speeds  $\Omega_i^2$  needed to actuate the desired forces and moments. The resulting solution is shown in (3.19) below.

$$\Omega^2 = \begin{bmatrix} \Omega_1^2 \\ \Omega_2^2 \\ \Omega_3^2 \\ \Omega_4^2 \end{bmatrix} = \mathbf{A}^{-1} \mathbf{U} = \begin{bmatrix} \frac{1}{4b} & \frac{1}{2bl} & \frac{1}{2bl} & -\frac{1}{4d} \\ \frac{1}{4b} & \frac{1}{2bl} & -\frac{1}{2bl} & -\frac{1}{4d} \\ \frac{1}{4b} & -\frac{1}{2bl} & \frac{1}{2bl} & \frac{1}{4d} \\ \frac{1}{4b} & -\frac{1}{2bl} & -\frac{1}{2bl} & -\frac{1}{4d} \end{bmatrix} \mathbf{U} \quad (3.19)$$

For other multirotor configurations, using additional rotors, an equivalent matrix  $\mathbf{A}$  will result in an over-determined equation system, yielding an infinite amount of possible solutions. A way to achieve a solution with an even control distribution on each rotor is to make use of the Moore-Penrose pseudo-inverse. The pseudo-inverse solution is given by  $\Omega^2 = (\mathbf{A}^T \mathbf{A})^{-1} \mathbf{A}^T \mathbf{U}$  [10]. Since the motor dynamics are very fast compared to the vehicle's motion, the calculated rotor speeds are used to calculate

the steady state motor voltages (2.12), which are then applied to the corresponding DC motors.

### 3.4 Disturbance analysis

Wind disturbances enter the system as forces and moments and will thereby cause translational and rotational acceleration. The drag force acts in the centroid, whereas the rotor forces act in each rotor plane. However, the resulting levers to the center of gravity will be quite small and thus rolling and pitching disturbance moments will not be of great significance. Hence, PD controllers were assumed sufficient for control of the roll and pitch angles, especially since these were connected to PID controllers in the outer loop. Since the drag moment  $Q$  affects the yaw angle and is susceptible to wind, it will benefit from integral action.

The forces have different dependence on the wind speed. Airframe drag, that has its point of attack in the airframe centroid, is proportional to the squared airspeed  $v$  according to  $F_d = \frac{1}{2}C_d\rho A v^2$ . The squared velocity dependence makes the airframe drag more prominent at high speeds and also yields faster attenuation of high frequency content. Rotor forces  $T$  and  $H$ , drag-moment  $Q$  and the tilting of rotor plane due to blade flapping have more intricate wind dependence. The advance ratio  $\mu$  and inflow ratio  $\lambda$  are both affected by the airspeed and contribute to variations of the proportionality variables  $C_T$ ,  $C_H$  and  $C_Q$ , for which expressions are given in Appendix C.2. These expressions depend linearly and quadratically on  $\mu$  and  $\lambda$  as well as the flapping angles. It has, however, been observed that the horizontal rotor forces have an approximately linear dependence on the wind speed.

#### Wind variation and turbulence

The Dryden wind turbulence model derived in Section 2.5 is used here to analyze the frequency content of wind disturbances. Note that the Power Spectral Densities (PSD) (2.34) and corresponding transfer functions' (2.36) bandwidth and magnitude changes with the relative airspeed  $V$  and the flight altitude  $h$ . Both the bandwidth and magnitude quantities decrease with the altitude and increase with the velocity.

Plotting the PSD for wind in each linear direction yields the diagrams in Figure 3.13, where the red line is for the longitudinal direction, green the lateral direction and red the vertical direction. The diagrams were created for an altitude of  $h = 10$  m, a mean relative airspeed of  $V = 20$  m/s and wind speed  $W_{20} = 15$  m/s at 6 m above the ground. The diagrams have been normalized relative to their respective maximum PSD. As can be seen, the lateral and longitudinal variations are attenuated at a much lower frequency (close to 1 rad/s for a factor 10 in the figure) than for the vertical turbulence.

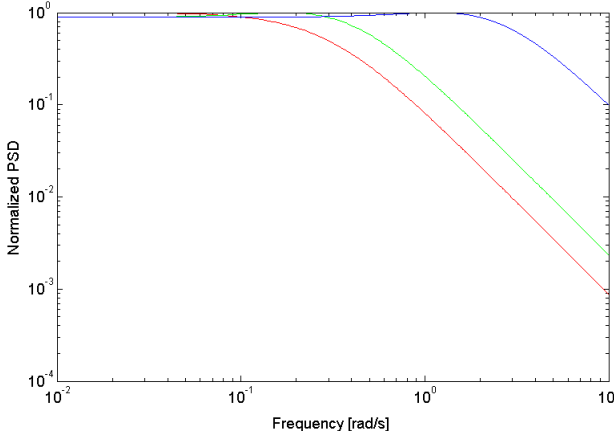


Figure 3.13: Longitudinal (red), lateral (green) and vertical (blue) Dryden wind turbulence normalized power spectral density diagrams.

With the previous discussion in mind regarding force and moment disturbance due to wind, it will be important that the controllers are designed in such a way that they respond well to these. To cope with the variations shown in the PSD diagrams in Figure 3.13 effectively, the positional controllers must be tuned such that the magnitude of  $S_u$  is small enough ( $\max(S_u) < 1$ ) and bandwidth of  $G_{cl}$  is high enough for these frequency ranges. As previously discussed, arbitrarily high control bandwidth is not possible to obtain due to physical limits and may not be desirable due to influence and amplification of measurement noise present in a real-life implementation. Thus, a trade-off is typically performed to achieve satisfactory performance.

## Wind magnitude and gusts

An increase of wind magnitude will not directly require high-performance control in terms of fast response (unless the onset of the wind is rapid). However, high enough wind speeds will challenge the physical limits of the control algorithms and actuators. For starters, enough thrust force must be available to counteract a wind in steady state in order for the UAV to hold its position. Saturation of motors running at their maximum voltage will be a problem. Also, if the UAV gets too far from its reference position (as a result of temporary onset of strong wind or saturation), the position error may become too large and yield undesirably aggressive control action. This, in turn, results in large pitching or rolling actions that may topple to multicopter. To amend for this, built-in saturation on control signals or reference set-pointing is appropriate.

## Lift and drag variations

Depending on the flight mode, the lift and drag coefficients  $b$  and  $d$  will vary. They are directly proportional to  $C_T$  and  $C_Q$  which depend on the advance ratio  $\mu$  and inflow ratio  $\lambda$ , increasing with  $\mu$  and decreasing with  $\lambda$ . This is explained in further detail in Appendix C.2. Not accounting for the variations of lift and drag coefficients when controlling the system has undesired effects to wind-robustness, making the multirotor unsteady in the vertical direction. Knowledge of these coefficients will help with both the control allocation as well as predicting the current motor load, which is needed to calculate appropriate input voltages. In this thesis, the mean value of these are assumed to be known at each instance, which isn't necessarily the case. For robust forward flight and wind-rejection, using a wind-estimating algorithm with an airflow sensor may significantly improve the performance, although responsive control may somewhat address the issue.



# 4

## Multifactor analysis

The aim of this chapter is to investigate how the performance of a multirotor is affected by different parameters. To achieve this, a large number of simulations have been conducted. A traditional and often intuitive approach is to test each parameter one at a time until the optimal performance is obtained for each parameter. This method is called the COST approach [11]. Unfortunately there are some major drawbacks with this method. The solution depends on the starting values and it doesn't guarantee that the found solution is the optimal design. The COST approach is also inefficient, especially when a lot of parameters are considered. In Figure 4.1, the COST approach is performed with two factors,  $X_1$  and  $X_2$ , that are increased separately until the performance is no longer improved and an optimum is believed to be found. From the plot, however, it is evident that this is not the case. It was therefore concluded that an alternative method is needed.

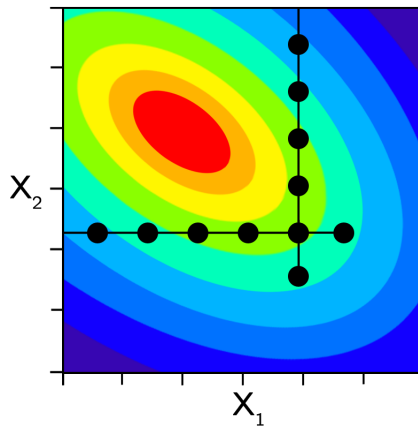


Figure 4.1: COST approach optimization.

## 4.1 Design of experiments

In *Design Of Experiments* (DOE), a carefully chosen set of experiments are conducted where all factors are varied simultaneously. The DOE approach is a reliable and efficient tool that is used in a lot of different industrial sectors such as the chemical industry, the car manufacturing industry and the food industry [11]. An example of this method can be seen in Figure 4.2, where it is applied to the same case as for the COST approach mentioned above. The design space is in this case made of a rectangular pattern, which means that a trend in the results can be identified. This will eventually lead to an optimal solution.

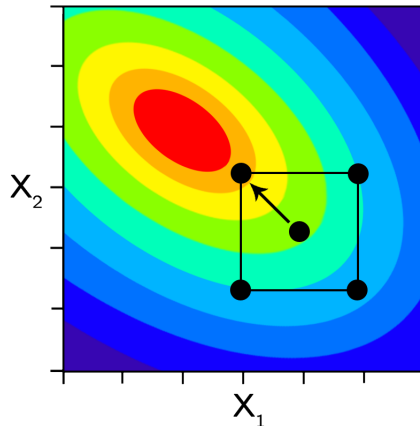


Figure 4.2: Design of experiments optimization.

Design of experiments can be used for a number of different phases during the development of a product. Familiarization, screening, optimization and robustness testing are examples of such phases. This report will only cover the screening and the optimization, but if the reader is interested, each of the experimental objectives are covered in [11].

For a multirotor, there are a vast number of different parameters which can potentially have an important effect on how the vehicle performs. Everything from dimensions and masses of all the individual parts to the number of propellers and their arrangements. It was concluded that it would not be possible to design a scalable multirotor model that can assume all possible design variations during the time frame of this thesis work. Therefore a number of limitations has been introduced in this chapter:

- The DOE evaluation will only deal with the quadrotor design which is the most common and basic multirotor concept.

- Only one type of propeller will be used.
- Only the cascaded PID controller will be used during the DOE evaluation. However, there will be a factor which represents either of two different PID parameters setups. This will give an indication of how much the responses are affected by software and physical characteristics respectively.

It should be noted that the multifactor analysis in this report is mainly aimed at investigating the influence of different parameters, and not so much at finding the optimal parameter combination which is usually the goal. The reason for this is that the exact values of each parameter are not likely to be valid for different airframe or propeller types, while the identified influence trends should be. The different steps of the analysis will nevertheless be called screening and optimization since the methods in each step will be the same.

### **DOE software**

It is possible to conduct a DOE without the aid of specialized software, but a lot of time can be saved by using such programs. There are several programs dedicated to design of experiments on the market today, but the alternatives for this report were narrowed down to the following two candidates:

1. MODDE by Umetrics [28].
2. modeFRONTIER by ESTECO [12].

Most of the theory in this section is based on the book developed by Umetrics [11]. However a number of different advantages spoke in the favor of modeFRONTIER which will be used during this project. The most notable advantages are listed below:

- The software is available at LTH.
- The authors of this report have some previous experience with the software.
- The software is compatible with MATLAB which means that each design in the DOE can be run sequentially without any manual interaction.

It should be noted that MATLAB has a set of functions based on design of experiments that could have been used for this project, but it was preferred to use modeFRONTIER which offers a more complete package.

## Experiment setup

A specified flight scenario is needed to be able to draw any conclusions about the performance of the quadrotor. It was decided to set the quadrotor in position hold while an external wind acts as a disturbance. A typical setup for the wind experiment includes choosing a mean wind speed and direction angle. Additional settings include turbulence and gust settings, which enhances the realism of the simulated experiment. The wind test that was used during the DOE simulations is shown in Figure 4.3. An initial mean wind of 8 m/s is used while a wind gust as well as variations predicted by the Dryden wind turbulence model is included. Section 2.5 gives a theoretical description of how these phenomena are modeled.

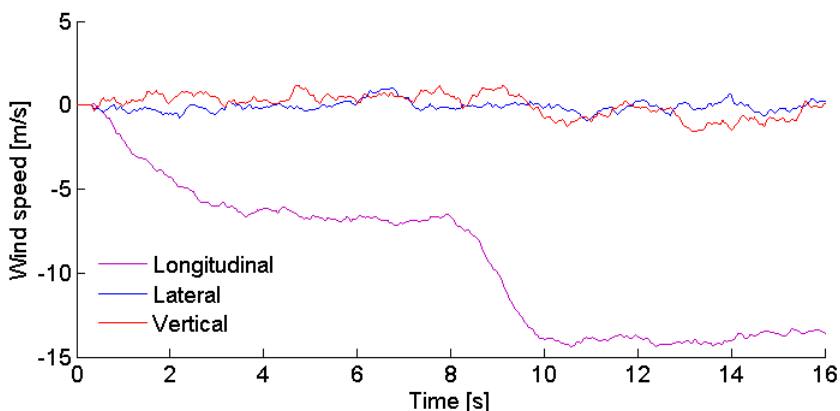


Figure 4.3: Typical wind test design which has been used for evaluation of the multirotor performance. The plots show wind speeds in the inertial longitudinal, lateral and vertical directions.

## Screening

During a screening process, the main goals are to detect the factors that have the most influence on the chosen responses, as well as finding the factor intervals in which the optimal design is most likely found. According to the Pareto principle, 20 % of the factors are responsible for roughly 80 % of the influence on the responses [11]. Therefore the most time efficient way of approaching an optimization problem is to exclude the factors which doesn't have any major impact on the final result as early in the process as possible. By doing so, more resources can be spent on tuning the factors that greatly affect the responses. It is also important to make sure that the ranges for the chosen factors includes the optimal design, or else that design won't be found during the optimization phase. The information which is gained from the screening is relatively easy to obtain, so the number of experiments needed per factor is quite low.

**Factors** Nine factors have been identified and used during the screening phase. These were chosen in the most general way possible so that the knowledge gained from the results could easily be applicable to different multirotor design concepts.

- $A_{xy}$  [0.02, 0.04] [m<sup>2</sup>]: The projected surface area that is perpendicular to the x- and y-axis. Because of the axisymmetric design, these areas are equal for the quadrotor.
- $A_z$  [0.04, 0.1] [m<sup>2</sup>]: The projected surface area that is perpendicular to the z-axis.
- $C_d$  [0.2, 0.4]: The drag coefficient of the airframe. This is normally a function of the relative airspeed direction. However, as mentioned above in Section 2.4, it was determined to use the same drag coefficient along the entire airframe.
- $I$  [0.048, 0.08] [kgm<sup>2</sup>]: The norm of the inertia tensor is defined as in (4.1), where  $I_{xx}$ ,  $I_{yy}$  and  $I_{zz}$  are the moments of inertia around the x-, y- and z-axes.:

$$I = \sqrt{I_{xx}^2 + I_{yy}^2 + I_{zz}^2} \quad (4.1)$$

- $l_a$  [0.3, 0.4] [m]: The arm length which is defined as the distance between the CoG of the quadrotor and the rotational axis for the propellers.
- $m_{tot}$  [1, 1.5] [kg]: The total mass of the quadrotor.
- $\tau$  {0.5825, 0.8737} [s]: The time constant of the positional control loop. This factor depends on the chosen control parameters, and it is therefore not straightforward to change this factor in a continuous way. With this in mind, it was decided to use the time constant as a qualitative factor with two different settings.
- $z_{CG}$  [-0.1, 0.1] [m]: The vertical distance between the CoG of the quadrotor and the centroid of the airframe.
- $z_{PG}$  [-0.1, 0.1] [m]: The vertical distance between the CoG of the quadrotor and the CoG of the propellers.

The factor ranges were mainly determined by rough estimations for what could be realistic limits with respect to the multirotor type and the chosen propellers. The most obvious example being that the total mass of the quadrotor is limited by the desired thrust margin. The quadrotor model consists of multiple body objects from the SimMechanics environment. There is no easy way of manipulating the characteristics of an entire multi-body system in SimMechanics, which means that

only masses and dimensions for the individual parts can be used as inputs to the simulation. An algorithm was therefore needed to translate the previously listed factors to compatible inputs. To simplify this algorithm it was decided to keep some of the geometrical dimensions constant in the mechanical sub-model. By doing so it was possible to determine the three different masses for the center, motors and arms based on the total mass, the inertia and the arm length. The projected surface areas were therefore only changed in the aerodynamic submodel, where the drag forces acting on the airframe were calculated. The correlation between  $I$ ,  $m_{tot}$  and  $l_a$  means that the intervals had to be carefully chosen so that the mass distribution would be realistic.

**Responses** This report is mainly focused on wind resistance, but it is also interesting to study how the flight time is affected by changing the different factors. The following responses were therefore chosen:

- Maximum position error,  $e_{max} = \max(e)$  [m]: The maximum distance that the quadrotor deviates from the desired position during the applied wind disturbance. The distance error  $e$  is defined as:

$$e = \sqrt{(x - x_{ref})^2 + (y - y_{ref})^2 + (z - z_{ref})^2} \quad (4.2)$$

- Mean power,  $P_{mean}$  [W]: The total mean electrical power during the applied wind disturbance is calculated as:

$$P_{mean} = \sum_{i=1}^4 \frac{1}{t_f - t_0} \int_{t_0}^{t_f} V_i I_i dt \quad (4.3)$$

It is worth noting that a decreased power isn't necessarily equivalent to a longer flight time. A quadrotor with an increased power, but higher thrust margin, could potentially equip more batteries which could result in a longer flight time. However, since accurate modeling of the battery was considered to be outside the scope of this report, it was concluded that the mean power is a strong indication of how the possible flight times are affected.

**Selection of regression model and DOE design** When the factors and responses have been chosen, it is time to choose a DOE design. There are a number of different designs of varying complexity and they are all more or less suited to specific problems. The choice of DOE design depends on which type of regressions model that is desired, but also on the number of factors that are being considered. The three most commonly used regression models are [11]:

- Linear:  $y = \beta_0 + \beta_1x_1 + \beta_2x_2 + \cdots + \varepsilon$
- Interaction:  $y = \beta_0 + \beta_1x_1 + \beta_2x_2 + \beta_{12}x_1x_2 + \cdots + \varepsilon$
- Quadratic:  $y = \beta_0 + \beta_1x_1 + \beta_2x_2 + \beta_{11}x_1^2 + \beta_{22}x_2^2 + \beta_{12}x_1x_2 + \cdots + \varepsilon$

The listed models are sorted after simplicity in descending order. If a more complex model is chosen, the potential to capture the behavior of the real process is improved, but such a model will also increase the number of experiments that needs to be conducted. A linear or interaction model is normally proposed for a screening process [11], depending on the number of factors. A linear model can be accomplished by a fractional factorial design while an interaction model needs a full factorial. In addition to these designs, there are also a number of other DOE designs that are suited for the screening process, such as Plackett-Burman, Rechtschaffner, L-design and D-optimal design. These are, however, considered to be outside the scope of this project.

The full factorial design is the most basic DOE design and therefore the most easily explained. It is common to define a standard experiment which serves as a reference. If the rest of the experiments are then symmetrically distributed around this center point, a full factorial design is obtained. A two-level full factorial design for three factors can be seen together with a reference point, also known as center point, in Figure 4.4. This means that the three factors are tested for two values each. In this report there have been nine different factors identified that may or may not have a significant impact on the responses. The full factorial design is mostly just relevant for up to five factors, after which the number of experiments are increased rapidly, see Table 4.1 [11]. It was therefore decided to use the fractional factorial which translates to 32 simulation runs, plus any number of center points that are being used. A two-level fractional factorial design for three factors can be seen together with a center point in Figure 4.5.

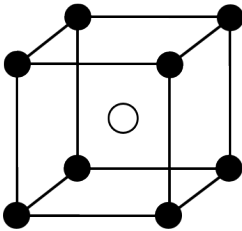


Figure 4.4: Full factorial design.

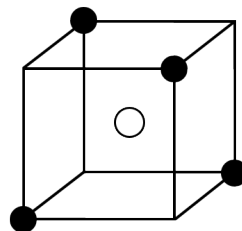


Figure 4.5: Fractional factorial design.

Number of investigated factors	Number of runs, Full factorial	Number of runs, Fractional factorial
2	4	—
3	8	4
4	16	8
5	32	16
6	64	16
7	128	16
8	256	16
9	512	32
10	1024	32

Table 4.1: Number of experiments needed for full and fractional factorials for a given number of investigated factors.

There are mainly two benefits of using center points in DOE [30]:

1. To provide a measure of process stability and inherent variability.
2. To check for curvature.

The experiments conducted in this project utilizes a simulated model with no variability, and hence there is no need for multiple simulations with the same center point. However, one center point can be useful to detect whether the relationship between a factor and a response is linear or not. Note that the time constant factor,  $\tau$ , is a qualitative factor which means that it is not possible to place a center point in the middle of the hypercube. Instead two different pseudo center points have to be used, one for each value of the qualitative factor. An example of how this can look for three factors is depicted in Figure 4.6.

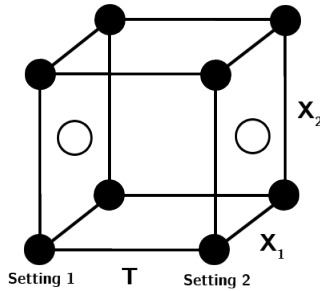


Figure 4.6: Center points for a full factorial with one qualitative factor.



**Results** When all of the experiments from the DOE has been run it is time to interpret and present the results from the simulations. There are numerous tools available in modeFRONTIER to help with this task. The RSM-tool automatically creates a regression analysis based on the raw data from the simulations. The coefficient of the linear regression models can be seen in Figure 4.7 and 4.8. Large coefficient values means that the response is largely influenced by the corresponding factor. Keep in mind that the coefficients have been normalized with respect to the factor intervals.

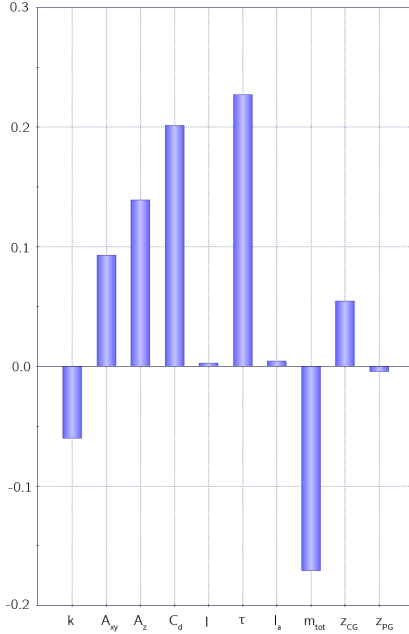


Figure 4.7: Linear regression coefficients for  $e_{max}$ .

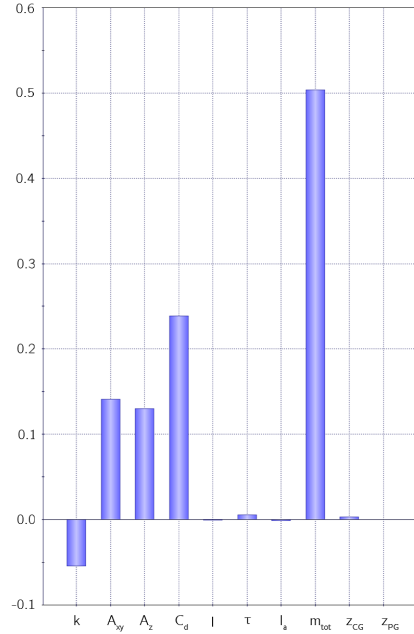


Figure 4.8: Linear regression coefficients for  $P_{mean}$ .

The difference between the simulated results and the predicted values from the linear regression model is presented in Figure 4.9 and 4.10. The blue dots are the values predicted by the regression model and the orange dots are the simulated values. The linear regression models are relatively poor, but this was to be expected since the quadrotor behavior is fairly complex. The average relative error is 35.3% for  $e_{max}$  and 5.53% for  $P_{mean}$ . Despite the questionable regression model, the collected data was still considered good enough for the screening phase, where the aim is only to roughly estimate the influence of the different factors.

An alternative method of presenting the information is to use a so-called student

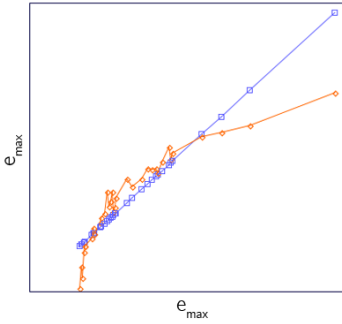


Figure 4.9: Linear regression validation for  $e_{max}$ .

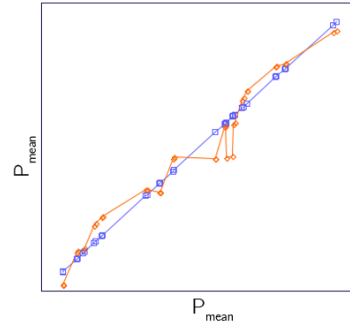


Figure 4.10: Linear regression validation for  $P_{mean}$ .

chart [12]. The influence of each factor is shown in Figure 4.11 and 4.12 for the maximum position error and the mean power respectively. The height of the bars is called effect size and shows the strength of the relationship between the output and the input values. It is calculated as the difference between  $M^-$  and  $M^+$  which are the mean values of the responses for the lower and upper ranges of the factor intervals. Low values indicate that there is not any detected relationship between the input and output variables. The transparency of the bars is a measure of a variables so-called significance. High transparency means that the effect size of that variable isn't very reliable. The red bars have a direct effect on the response. This means that an increased factor value will increase the response value. The blue bars have an inverse effect which consequently means that an increased factor value will decrease the response. One of the advantages of the student chart is that it is possible to see the certainty of the influence of each factor individually. The information is also presented in a more easily interpreted way, especially when higher order regression models are needed.

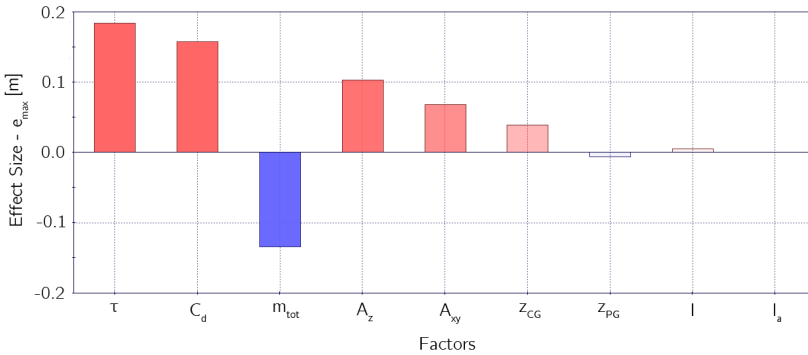
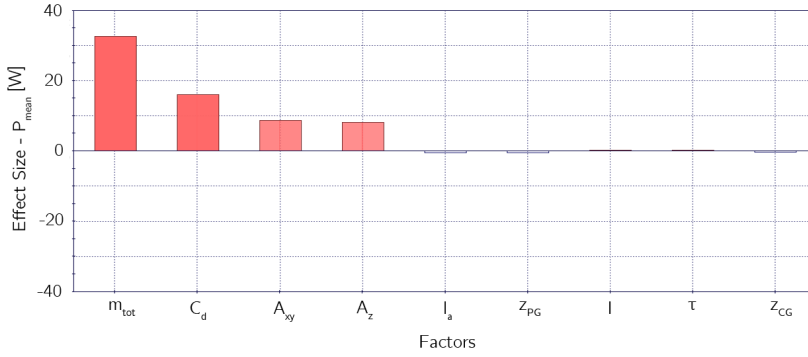


Figure 4.11: Student chart for  $e_{max}$ .

Figure 4.12: Student chart for  $P_{mean}$ .

**Conclusions** The aim of the screening phase is normally to eliminate any potential factors that don't have any influence over the responses. It is possible to distinguish a couple of factors which don't appear to have any influence over the responses by looking at the regression coefficients and the student charts.  $l_a$ ,  $I$  and  $z_{PG}$  don't affect neither the position error or the power in any significant way. The mean power isn't affected by  $\tau$  or  $z_{CG}$  either while the position error is somewhat influenced by  $z_{CG}$ , even if that information isn't completely reliable which is suggested by the transparent bar in Figure 4.11.

The arm length  $l_a$  determines the maximum attitude moments for a given actuator. The desired angular velocities of the quadrotor are determined by the control algorithm which takes the arm length into account. Hence, for a given set of control parameters, the length of the arm shouldn't have any impact on the position error. For a longer set of arms it would theoretically be possible to tune the attitude controller more aggressively which can be beneficial for the wind resistance potential. In reality, there is a strong correlation between the length of the arms and the projected surface areas which are preferably minimized according to 4.11. It is worth noting that because of the potential aerodynamic interference between different rotors, there is a lower limit to the length of the arms which is determined by the size of the propellers and the number of arms. If manual flight is considered, longer arms will generally make multirotors easier to control in a stable manner. This is caused by the fact that an increased arm length will make a certain angle error more apparent to the human eye.  $l_a$  will not be further studied in the optimization, but it would be interesting to study how the total drag and performance of the quadrotor is affected by having the rotors close to each other and closer to the rest of the equipment which is often situated at the center. This would however require more advanced modeling techniques than those covered in this report.

The inertia of the quadrotor determines the angular acceleration caused by a given

moment. This inertia is also taken into account by the controller which means that the inertia doesn't affect the maneuverability for a given set of control parameters. However, the tuning of the attitude control is limited by the inertia which means that a smaller and lighter multirotor generally allows more agile flight. Intuitively an increased inertia should be beneficial for rejecting moment disturbances, and this is also confirmed by the input sensitivity transfer function in (3.11). It is therefore surprising that the results doesn't show any correlation between the inertia and the maximum position error. One explanation for this could be that the translational velocities are constant along the quadrotor body which could potentially mean that the disturbance moments are relatively small compared to the translational forces. However, this explanation is contradicted by the influence of the vertical distance  $z_{CG}$  which causes a disturbance moment. After some additional testing it was concluded that the inertia does have an affect on  $e_{max}$ , but it's influence is either direct or inverse depending on the signs of  $z_{CG}$  and  $z_{PG}$ . It was therefore decided to further study these factors during the optimization.

The total drag of the airframe, which is determined by  $A_{xy}$ ,  $A_z$  and  $C_D$ , greatly affects the position error as well as the power for the chosen factor intervals. This doesn't come as a surprise, especially since the drag force on the airframe is proportional to the squared wind magnitude. It is desirable to minimize these three factors for both of the responses and they will therefore not be further investigated during the optimization since the optimal design can safely be assumed to be found when they are minimized.

The same logic can be applied to the time constant  $\tau$ . This factor has the biggest influence over the position error, but the performance will only be increased for a decreased time constant as long as the closed-loop system is stable. It was nevertheless interesting to see how much the software can improve the performance compared to the physical characteristics of the vehicle.

The total mass  $m_{tot}$  is also very significant for the performance of the multirotor. It is already clear that it will have a conflicting influence on the maximum position error and the mean power. It will therefore be further studied in the optimization.

## Optimization

During an optimization the aim is normally to find the optimal combination of factors which will give the best performance. Therefore one or more objectives have to be defined so that the solver knows if a response should be maximized or minimized. Often these objectives are in conflict with each other so that a compromise has to be made. The optimization requires a lot of runs per factor in contrast to the screening process where just a few simulations have to be conducted for a lot of factors. The aim of the optimization in this report isn't primarily about finding the exact value for each factor, but rather to further investigate the effect of the individual factors

and the relationship between the two response objectives.

**Factors** The influence of the different factors have been discussed during the screening phase and it was concluded that  $m_{tot}$ ,  $z_{CG}$ ,  $z_{PG}$  and  $I$  would be further investigated during this optimization. The optimization was run with a time constant setting of 0.8737 s, which is the slower setting. This setting is probably closer to what the time constant would be in a real implementation.  $A_{xy}$ ,  $A_z$  and  $C_D$  were locked at the minimum values which will give the optimal design combination within the specified factor intervals. The arm length  $l_a$  was locked to the center value of the interval, but this choice shouldn't have any significant effect on the results.

**Responses** The same responses as in the screening will be used during the optimization. It is desirable to minimize both of these responses, which means that two objectives have to be added to the responses during the optimization. The workspace in modeFRONTIER can be seen in Figure 4.13, where the optimization phase is modeled.

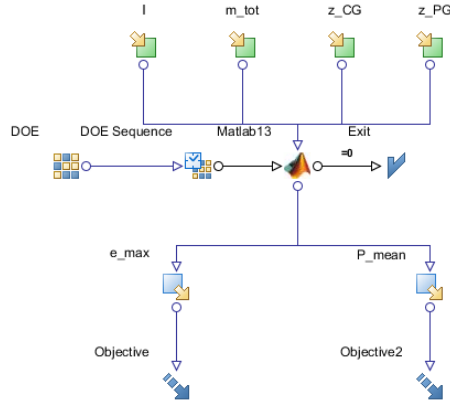


Figure 4.13: Workspace in modeFRONTIER.

**Selection of regression model and DOE design** It is very important to have a good model of the process during the optimization process so that the solver can converge to the real optimum. Therefore a quadratic regression model is commonly used, but sometimes even more complex models are necessary. In this report it was decided to use a central composite design since it is an intuitive extension of the factorial designs which also supports quadratic regression models. There are three basic central composite designs; circumscribed (CCC), face-centered (CCF) and inscribed (CCI) which are pictured in Figure 4.14 for two factors.

Only the CCI and the CCF designs are available in modeFRONTIER. The CCF

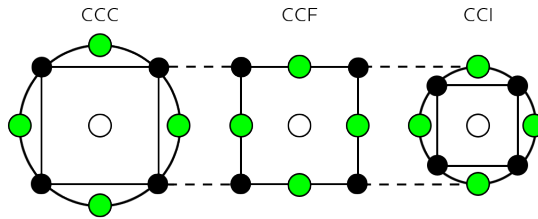


Figure 4.14: The three basic central composite designs visualized for two factors.

design covers all of the test range while the CCI design tests each factor at five different levels which potentially gives the CCI design slightly better possibilities to make an accurate quadratic model. In this case the authors decided to use the CCF design since some of the factors will ultimately tend towards either the maximum or the minimum setting during the optimization.

**Optimizer** It is necessary to choose an optimizer which will work towards the specified objectives. There are a number of different optimizers available in modeFRONTIER and they are suited for different tasks depending on things such as the number of objectives, the type of the objectives and the number of factors and responses. In this project it was decided to use MOGA-II which is one of the basic optimizer choices in modeFRONTIER. MOGA stands for multi objective genetic algorithm and it is designed for fast Pareto convergence according to the software guide. Pareto designs can be described by the following definitions [22]:

- A design point dominates another if it is superior with respect to one of the objectives while not being inferior with respect to any of the other objectives.
- Two design points are indifferent with respect to each other if neither point is dominating the other.
- A design point is a Pareto-optimal design if it is not dominated by any other design points.

The so called Pareto-frontier is a curve that is defined by all the Pareto-optimal design points. The optimal design lies somewhere along this curve, depending on the relative importance of the different objectives.

**Results** During the optimization phase, a total number of roughly 550 simulations were run including the center point and the ones that were generated by the central composite face-centered design. The RSM-tool was used to create a quadratic regression model whose coefficients can be seen in Figure 4.15 and 4.16.

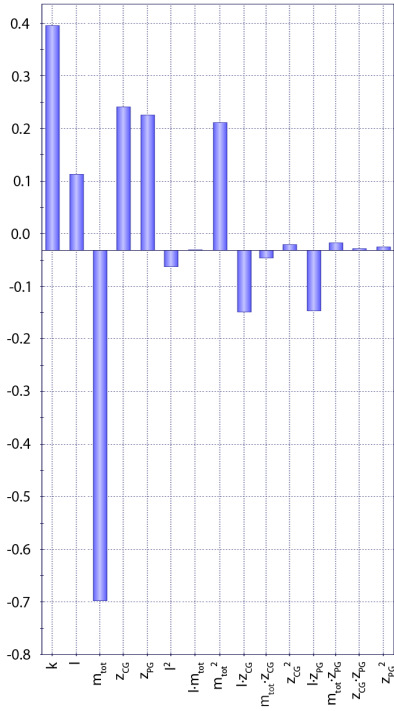


Figure 4.15: Quadratic regression coefficients for  $e_{max}$ .

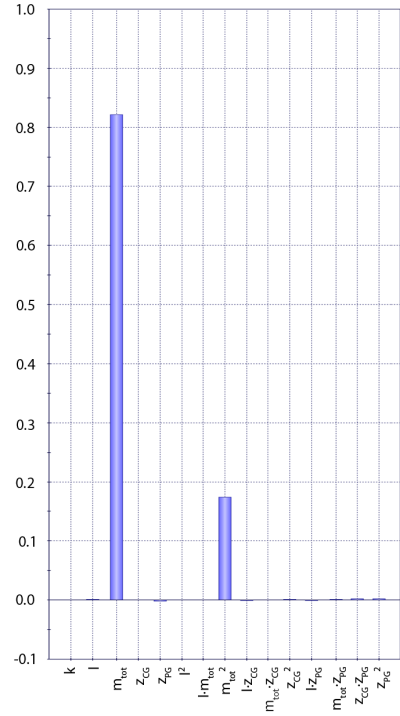


Figure 4.16: Quadratic regression coefficients for  $P_{mean}$ .

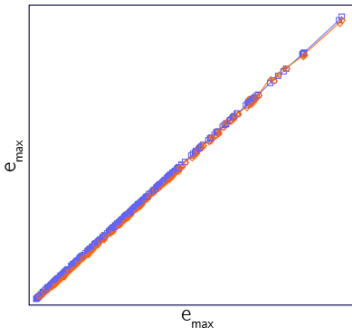


Figure 4.17: Quadratic regression validation for  $e_{max}$ .

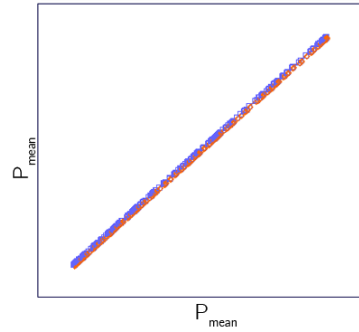


Figure 4.18: Quadratic regression validation for  $P_{mean}$ .

The regression model values are compared to the simulation results in Figure 4.17 and 4.18. This regression model is much better than the linear version that was used in the screening section. The average relative error was reduced to 0.409% for  $e_{max}$  and 0.0818% for  $P_{mean}$ .

The influence of each factor can also be seen in the student charts pictured in Figure 4.19 and 4.20.

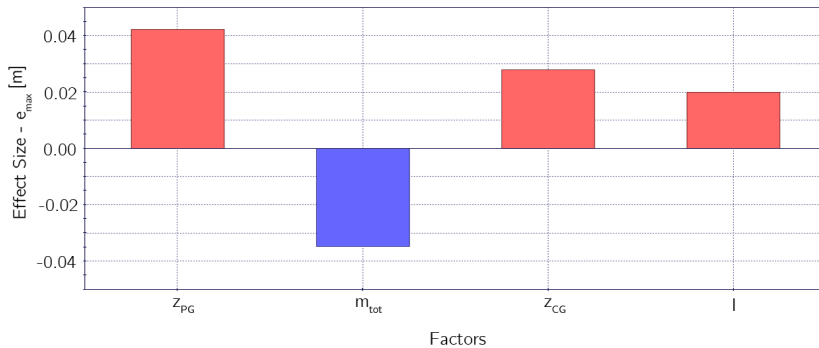


Figure 4.19: Student chart for  $e_{max}$ .

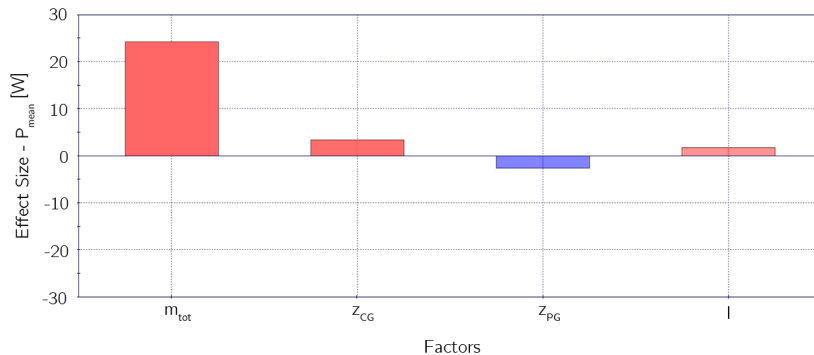


Figure 4.20: Student chart for  $P_{mean}$ .

The objectives for the optimizer were to minimize the mean power and the maximum position error. These objectives oppose each other for some of the parameters, so that there is not a single best design solution. The Pareto-frontier can be seen in the scatter plot in Figure 4.21 which contains all of the simulated designs. The highlighted dots are the Pareto-optimal designs.

The best factor combinations for  $e_{max}$  and  $P_{mean}$  can be seen in Figure 4.22 and 4.23 respectively.



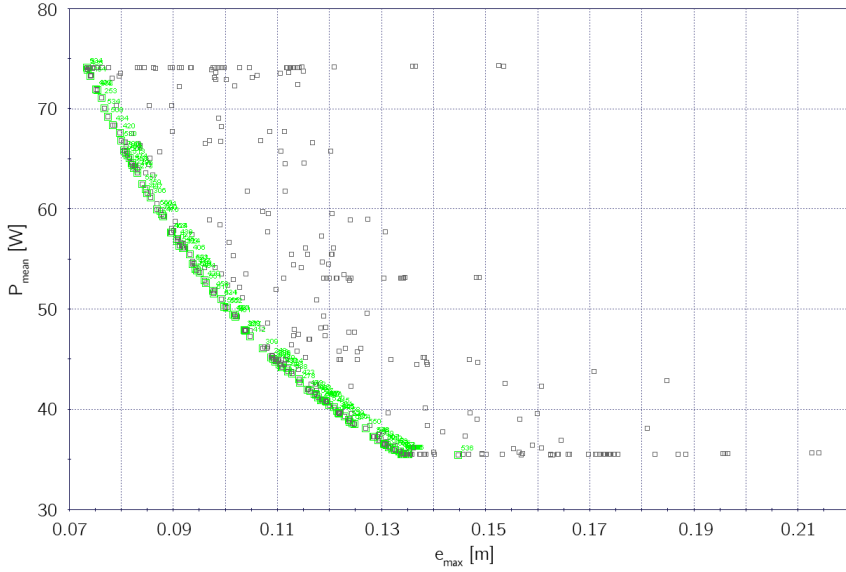


Figure 4.21: Pareto-frontier from the optimization run.

ID	M	CATEGORY	I	m_tot	z_CG	z_PG	P	e_max
5		CCD	4.8000E-2	1.5000E0	-1.0000E-1	-1.0000E-1	7.4107E1	7.3304E-2
334		MOGA2	4.8000E-2	1.5000E0	-1.0000E-1	-1.0000E-1	7.4106E1	7.3304E-2
435		MOGA2	4.8447E-2	1.4975E0	-1.0000E-1	-1.0000E-1	7.3880E1	7.3529E-2
464		MOGA2	4.8438E-2	1.4907E0	-9.9984E-2	-1.0000E-1	7.3269E1	7.4010E-2
492		MOGA2	4.8451E-2	1.4756E0	-9.9896E-2	-9.9652E-2	7.1920E1	7.5176E-2

Figure 4.22: The best designs with respect to wind resistance.

ID	M	CATEGORY	I	m_tot	z_CG	z_PG	P	e_max
536		MOGA2	4.8596E-2	1.0000E0	-9.9996E-2	-4.2604E-2	3.5494E1	1.4463E-1
156		MOGA2	4.8586E-2	1.0000E0	-1.0000E-1	-9.9392E-2	3.5500E1	1.3517E-1
9		CCD	4.8000E-2	1.0000E0	-1.0000E-1	-1.0000E-1	3.5500E1	1.3505E-1
321		MOGA2	4.8583E-2	1.0000E0	-1.0000E-1	-1.0000E-1	3.5501E1	1.3493E-1
366		MOGA2	4.9077E-2	1.0000E0	-9.9378E-2	-1.0000E-1	3.5505E1	1.3478E-1

Figure 4.23: The best designs with respect to efficiency.

**Conclusions** The regression model that was developed during the optimization provides a much better fit for the simulated data. Conclusions can therefore safely be made from the regression coefficients as well as from the student charts, where the transparency of the bars are now generally much lower.

The total mass  $m_{tot}$  should be maximized to achieve the highest possible wind resistance. If agile flight is not a necessary criteria, the thrust margin should therefore be kept relatively low. The rotational speeds of the rotors will generally decrease when

a wind disturbance is present. Saturation of the actuators should therefore not be a problem up until a certain limit for the rotor disk angle of attack where the thrust will start to decrease again. However, it is of utmost importance to minimize the mass if the power is going to be minimized. This is the main reason why there has to be a trade of between power and the maximum position error, which is also confirmed by the Pareto-frontier in Figure 4.21. It is clear that an eventual final design choice would depend on the relative importance of the objectives.

A common belief among hobbyists is that the rotor plane should be placed above the overall center of gravity to achieve the best stability. This belief originates from the intuitive comparison to an inverted pendulum. However, this parable is faulty since the thrust of a multirotor will always point through the CoG if properly balanced. Pounds *et al.* [32] shows that to achieve the best stability for the X-4 Flyer, the rotor plane should optimally be aligned with the CoG. It is also noted that a small error of this placement will lead to significant changes for the system dynamics, and hence the rotor plane is placed with a small offset relative to the CoG. The results in 4.19 shows that  $z_{PG}$  should be minimized i.e. the rotor plane should be placed under the center of gravity. One explanation for this could be that the moment caused by the horizontal force will support the actuated pitch/roll moment that is necessary to tilt the thrust force so that it can counter the translation drag force. The desirable minimization of  $z_{CG}$  can be explained similarly.

The inertia of the quadrotor does seem to have a relatively large influence on the position error, as opposed to the screening results. It is apparently desirable to minimize the moment of inertia with respect to the wind resistance, which is slightly surprising by keeping (3.11) in mind. However, note that this input sensitivity function is for the attitude while the response during this DOE has been focused on the position error. Also remember that the optimizer has minimized the vertical distances  $z_{PG}$  and  $z_{CG}$ , which means that the majority of the design combinations have a negative value for these factors. Therefore, as explained above, the disturbance moments caused by the wind will have a positive effect on the positional stability. The angular acceleration towards the wind is increased by minimizing the moment of inertia. If  $z_{PG}$  and  $z_{CG}$  would have been positive, the disturbance moments caused by the wind would instead have a negative effect on the positional stability. This is the reason why the inertia didn't seem to have any affect on  $e_{max}$  during the screening.

To summarize the multifactor analysis of the scalable quadrotor, the wind resistance and the efficiency are conflicting objectives for the quadrotor. This is mostly caused by the mass of the vehicle which should be maximized with respect to  $e_{max}$  and minimized with respect to  $P_{mean}$ ,  $A_{xy}$ ,  $A_z$  and  $C_d$ , which determines the total drag of the quadrotor airframe, should intuitively be minimized which is also supported by the results from the screening. The rest of the factors might not be quite as

influential, but if the airframe is designed in an aerodynamically favorable way, the tuning of these factors will have an increased influence on the performance. The vertical distances  $z_{PG}$  and  $z_{CG}$  should ideally be negative, but this can be hard to implement in a conventional multirotor design, especially if camera equipment is mounted below the body.

# 5

## Design development

The work presented in this chapter aims to propose a final multirotor concept suitable for windy conditions. Considering the limited time frame of this project, it was not deemed possible to construct fully functional models of every potential multirotor concept. Instead, it was decided to base the final concept choice on research, simplified simulations and engineering intuition. The chapter is mainly divided into two sections, listed below.

- Rotor and airframe assessment.
- Concept evaluation.

Concepts for rotor and airframe configurations will be assessed separately in regards to wind resistance and efficiency properties. Knowledge and conclusions drawn from this will then be used, together with the results from the multifactor analysis in Chapter 4, during the proceeding concept evaluation. During this, a number of potentially favorable multirotor concepts are generated and compared in a concept scoring process. The scoring is based on a number of specified criteria, which will determine the final design choice. Concept scoring is a frequently used method for comparing different concepts during a design development process. More information on design development can be found in Ulrich and Eppinger [44].

### 5.1 Rotor and airframe assessment

During this section, different rotor and airframe configurations are studied separately. By doing so, it was possible to exclude less advantageous solutions before combining rotor and airframe configurations into complete multirotor concepts. Thus, a decrease in the number of possible multirotor concept candidates is achieved.

## Rotor configurations

There are several different rotor types more or less suited to a specific task and/or design restrictions. The aim of this section is to determine which configurations that are most suited for a wind resistant multirotor, while also considering the influence they might have on power efficiency. The conclusions from this chapter are mostly based on available literature and logical reasoning, based on the experience gained when constructing the model as well as the results from the multifactor analysis in Section 4. In addition, a number of simplified rotor simulations have been conducted to verify some of the reasoning.

During these simulations, different rotor configurations were compared at certain rotational speeds, influenced by wind with varying magnitude  $V_\infty$  and inflow angle  $\alpha$ . The interval for  $V_\infty$  was decided based on the assumed limitations of the model. Also, only positive  $\alpha$  were evaluated since multirotors generally pitch down towards the incoming wind in order to compensate for the force applied by the wind. The upper limit of  $\alpha$  was decided based on that the pitch angle of the modeled quadrotor rarely exceeded this angle during high wind disturbances. It is important to keep in mind that these simulations only make use of the rotor models and doesn't take the dynamic movement of the multirotor into account. The responses that were used to evaluate the performance of the rotor configurations are listed below.

- Dynamic power loading  $PL_d = \frac{F_z}{P}$
- Equilibrium angle  $\theta_{eq} = \arctan\left(\frac{F_{xy}}{F_z}\right)$  where  $F_{xy} = \sqrt{F_x^2 + F_y^2}$

*Power loading* is an efficiency parameter frequently used for different types of rotorcraft. It is defined as the ratio between the thrust and power required to hover [19].

$$PL = \frac{W}{P} \quad (5.1)$$

However, the authors of this report were also interested to see how the thrust to power ratio changes for different flight conditions. This ratio was decided to be called dynamic power loading, but will henceforth simply be referred to as power loading  $PL$ .

In Figure 5.1, it can be seen that the expression in (5.2) holds when a force equilibrium along the horizontal plane is achieved.

$$\tan \theta_{eq} = \frac{F_{xy}}{F_z} \quad (5.2)$$

Note that the equilibrium angle is only an indication of how much the multirotor would have to pitch down to be able to compensate for the wind at a specific moment. In reality, or when running the full multirotor simulator, the angle of attack for the rotor disk will continuously change as the multirotor starts to pitch down towards the wind. There will also be a delay until the multirotor has actuated the pitch maneuver, during which the force will cause an acceleration that depends on the total mass of the vehicle. However, this delay is reduced by minimizing the equilibrium angle.

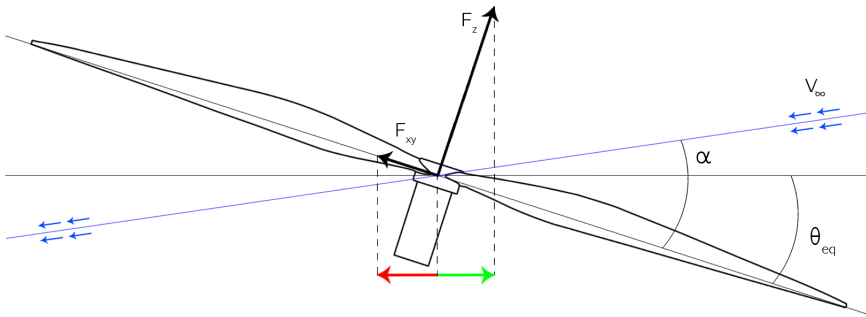


Figure 5.1: Equilibrium angle explanation.

### Propeller

There are a lot of different factors to consider when evaluating the performance of a rotor, even when only considering regular propellers. The propeller can have varying dimensions and operate at different speeds depending on the payload. Additionally, more complex solutions such as variable pitch propellers can be used. In this section, some of these factors will be investigated further to give a better understanding of how they may affect the performance of the multirotor. The two-bladed propeller is without a doubt the most commonly used rotor setup. Therefore it will be used as a reference throughout this section.

*Simulation* The *APC 10x4.7 Slowflyer* propeller, used during the quadrotor simulations, was used as the reference for the rotor simulations. The equilibrium angle  $\theta_{eq}$  and the power loading  $PL$  are plotted as functions of  $V_\infty$  and  $\alpha$  in Figure 5.2. These results can partially be predicted by the expressions for the nondimensional coefficients in C.23, and they are sources for control disturbances which are normally not taken into account.

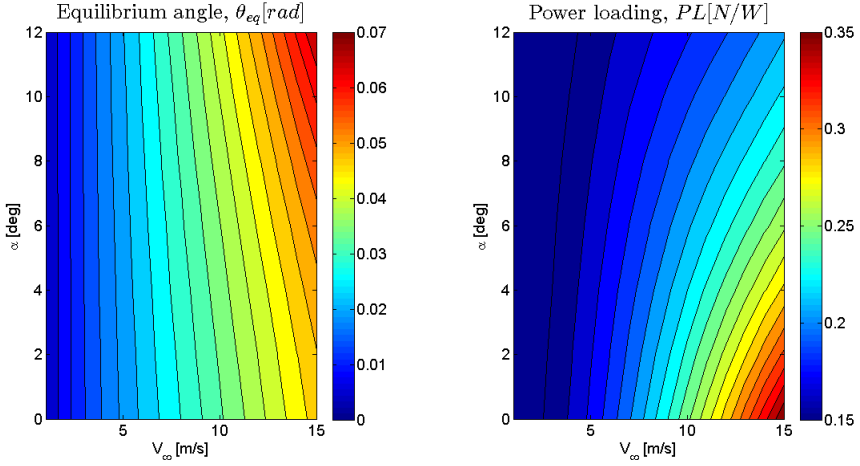


Figure 5.2: Equilibrium angle and power loading for the reference propeller, APC 10x4.7 sf, running at 425 rad/s.

**Propeller size and operating speed** It would be very time consuming to investigate all of the possible parameters that determine the performance of the propeller. For this reason, it was decided to focus on the influence of the propeller size and the rotational speed at which it operates. To this end, a factor  $K_s$  was introduced to scale the radius and the average chord length of the propeller, with mass and rotational inertia scaled accordingly.

**Simulation** Evaluating both the scaling factor  $K_s$  and the rotational speed  $\Omega$  simultaneously spoke in the favor of using another DOE design. Factor intervals for these two quantities are shown in Figure 5.3, where a two-level full factorial is depicted. Note that the center point is the mentioned reference whose results were presented in Figure 5.2.

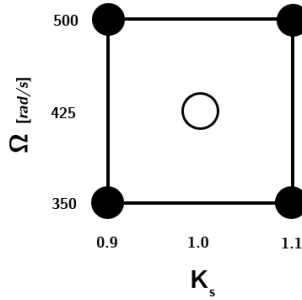


Figure 5.3: Design of experiments for the propeller simulations.

The factor  $K_s$  was kept quite close to one since even small changes to the radius and the average chord length have a relatively large impact on performance. Also, the authors didn't want to deviate too much from the original propeller dimensions, for which the model has been validated with real experimental results. The rotational speeds were determined with the aim of covering the most frequented operating ranges. Results from the simulations are shown in Figure 5.4 and 5.5 respectively. For an easier interpretation of the results,  $\theta_{eq}$  and  $PL$  have been normalized with the corresponding results from the center point.

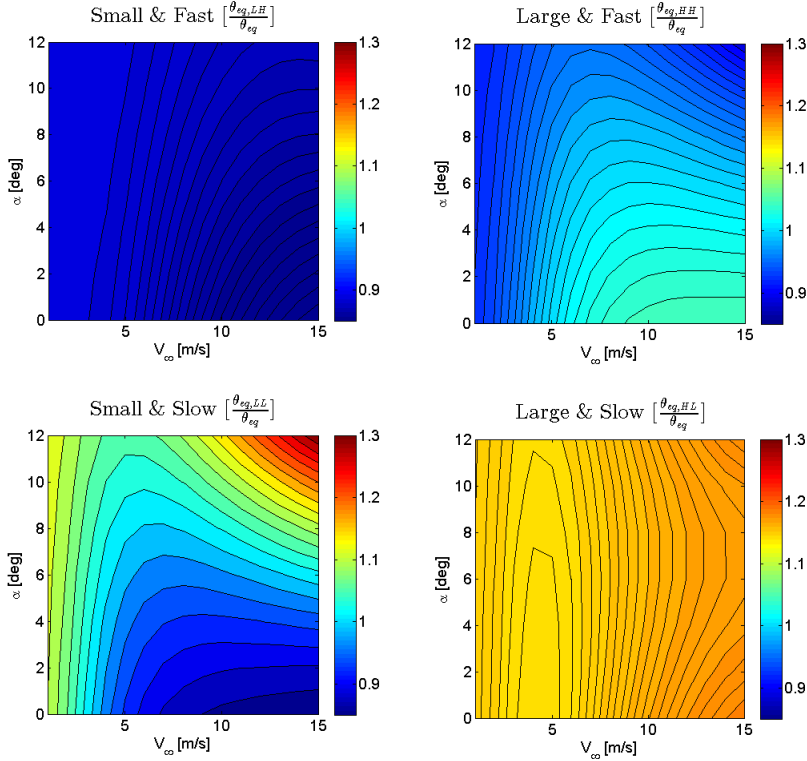
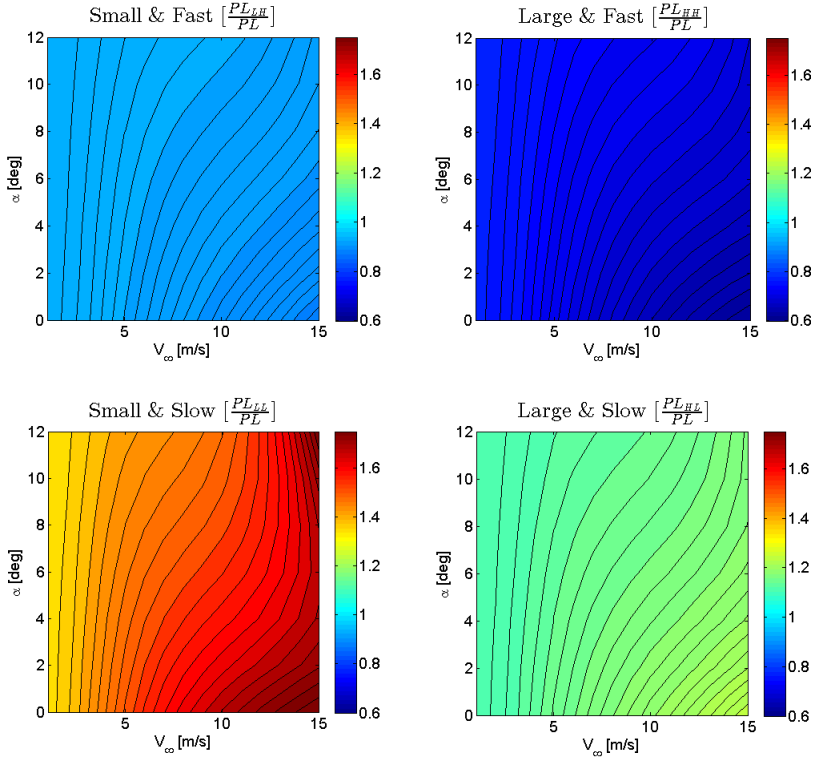


Figure 5.4: Design of experiments result:  $\theta_{eq}$

It is evident from the simulation results that, within the investigated intervals, it is desirable to use small and fast spinning propellers for minimum wind disturbance. In contrast, it is shown to be more efficient to use small and slow spinning propellers. These results are assumed to apply for all rotor configurations covered in this report.



Figure 5.5: Design of experiments result:  $PL$ 

**Conclusions** The results for the power loading can easily be predicted by considering the expressions derived by MT (C.5), where  $T \propto (\Omega R)^2$  and  $P \propto (\Omega R)^3$ . This confirms that small and slow spinning propellers are favorable. However, such propellers will not generate as much thrust. When designing helicopters, the choice is usually limited to either a small and faster spinning propeller, or a larger and slower spinning propeller. Choosing between these two options, the general opinion is that larger propellers are more energy efficient which is also confirmed by the results in Figure 5.5. Multirotors are not limited to a single rotor and could therefore potentially use multiple small and slow spinning propellers. However, propellers need to have some spacing between each other to avoid aerodynamic interference [16], which makes it difficult to implement a large number of propellers in practice. Furthermore, if a maximum footprint diameter is given as in [9], the conclusion will be that a large main rotor is favorable from an efficiency perspective.

The results for the equilibrium angle can not be predicted in a similar fashion. According to the results in Figure 5.4, a small and fast spinning propeller is favorable

for wind resistance. It is also worth noting that a smaller propeller can spin faster since the maximum allowed rotational speed is limited by the blade tip speed.

Larger propellers will have higher blade tip speeds, for a given rotational speed, which might cause compressibility effects and noise. In addition, smaller propellers have a smaller moment of inertia which will reduce the time constants of the motors.

### Multi-bladed propeller

Sometimes it is preferable to use more than two blades on a propeller. Usually, this is caused by limitations concerning available space, structural properties or actuator performance. There is, however, a limit to the number of blades that can be used since they will interfere with each other if placed too close together. This limit depends on a number of factors such as rotational speed and propeller dimensions, but the theory behind this will not be covered in this report.

*Simulation* It was decided to compare a three-bladed propeller with the reference propeller since this is the most common alternative. It has been assumed that any benefits or drawback obtained by using three blades will also apply to other multi-bladed propellers, only magnified. A comparison between propellers with a different number of blades might also depend on the size of the rotors and their rotational speed, but these effects have been neglected. The simulation for the three-bladed propeller has been conducted at the center point from Figure 5.3 to get the most representative comparison. Once again, it was decided to normalize  $\theta_{eq}$  and  $PL$  with the results for the reference rotor. The ratios for the three-bladed propeller can be viewed in Figure 5.6, where the used color scale will be applied for all of the the proceeding rotor comparison graphs.

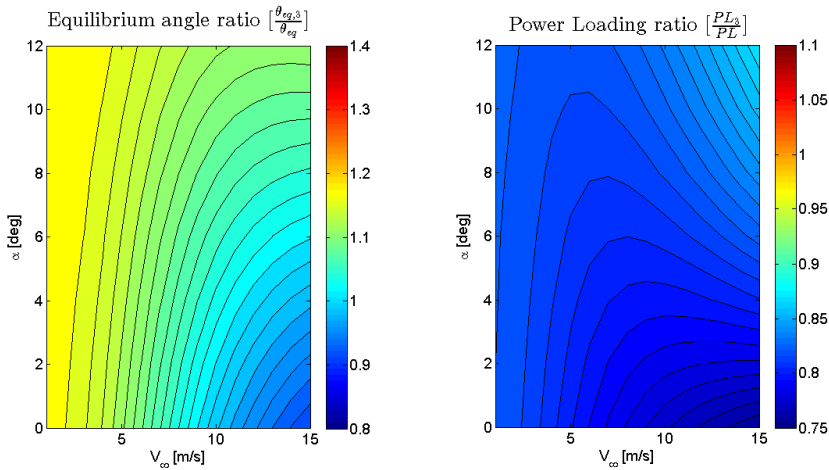


Figure 5.6:  $\theta_{eq}$  and  $PL$  ratios for an equally sized three-bladed propeller.

Using an equally sized propeller with three blades at the same rotational speed as the reference propeller will result in an increase of the aerodynamic forces and moments, including the thrust. A multirotor that uses propellers with three blades can therefore carry more weight, which is favorable for wind resistance and cannot be investigated in this simulation. Instead, it has to be investigated with the complete multirotor simulator.

Alternatively, a scaling factor  $K_s$  can be used so that both propellers have equal thrust margin  $\beta = T_{max}/(mg)$ . The maximum thrust was calculated at 6500 RPM  $\approx 680$  rad/s for each propeller. During this simulation, it was also decided to estimate the time constant for the motor. This was accomplished by using a linearization of the DC motor model presented in Section 2.2. Since the reference propeller's rotational speed was used for this comparison as well, the motor model was linearized around 425 rad/s. The resulting  $\theta_{eq}$  and  $PL$  ratios from the simulation can be seen in Figure 5.7. The time constant proved to be almost exclusively dependent on the rotational inertia of the propeller. The time constant for the motor with the scaled three-bladed propeller was therefore approximately 25 % longer than for the reference.

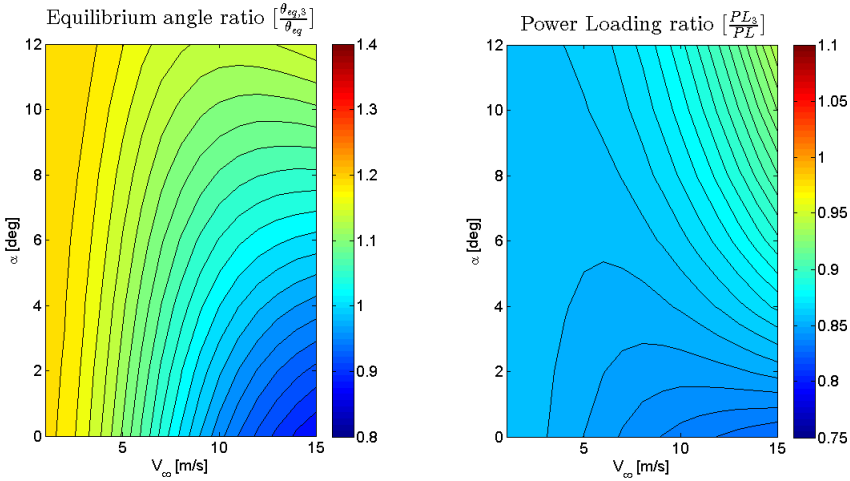


Figure 5.7:  $\theta_{eq}$  and  $PL$  ratios for a scaled three-bladed propeller. A scaling factor  $K_s = 0.952$  was used to obtain the same  $\beta$  as for the reference propeller.

**Conclusions** The results from the two simulations are fairly equal, where the scaled propeller showed slightly better efficiency and wind resistance performance. This was expected from results shown in Figures 5.4-5.5. The power loading is clearly lower than for the reference propeller, whereas a uniform result for the equi-

librium angle was not evident. The increased rotational inertia, caused by the extra blade, decreases the bandwidth of the motor, which is undesirable for the multirotors ability to deal with rapid wind variations.

Despite the disadvantages, there are certain implementation aspects which might swerve the choice in favor of the three bladed propeller. The thrust for a given propeller radius is higher for the three bladed propeller, enabling an increased aircraft payload without increasing the overall size of the vehicle. The possibility to carry additional mass will have a positive effect on the multirotor’s ability to counteract wind disturbance. Also, a three-bladed propeller might be favorable from a structural perspective. The reduced tip speeds and more evenly distributed inertia around the rotational axis could potentially reduce the vibrations translated to the multirotor.

To summarize, pros and cons of the multi-bladed propeller are listed in Table 5.1.

PROs	CONs
<ul style="list-style-type: none"><li>• The maximum possible payload is increased for a given rotor size.</li><li>• Allows a more compact airframe design.</li><li>• Potentially reduces vibrations.</li></ul>	<ul style="list-style-type: none"><li>• Increases the motor time constant.</li><li>• Inefficient.</li></ul>

Table 5.1: List of pros and cons of the three-bladed propeller.

**Variable pitch propellers** Using propellers that enable control of the blade pitch presents a more complex rotor solution. By using such rotors, perhaps the largest advantage with multirotors, mechanical simplicity, is somewhat neutralized. There are, however, some major advantages which can compensate for the increased complexity. An implemented variable pitch propeller can be seen in Figure 5.8.



Figure 5.8: Implementation of a variable pitch propeller for the Stingray 500 quadrotor [17].

**Conclusions** Variable pitch propellers is not a rotor concept that will be modeled during this project due to time constraints. However, it provides a decreased actuator time constant [8] which primarily increases the agility and responsiveness of the multirotor. It can potentially also improve wind resistance if a suitable control algorithm and allocation is applied. It is, however, hard to predict how a multirotor equipped with variable pitch propellers will be affected by wind disturbances because of the added degree of freedom. Therefore, a complete model has to be developed and controlled before any easily interpreted results can be achieved.

The added complexity of this rotor concept places the aircraft in a grey zone between helicopter and regular multirotor. Hence, a performance comparison with helicopters of similar size could also be relevant if variable pitch propellers are considered.

To summarize, pros and cons of the variable pitch rotor concept are listed in Table 5.2.

PROs	CONs
<ul style="list-style-type: none"> <li>• Decreases the actuator time constant.</li> <li>• Acceleration during descent flight can be greater than gravity.</li> <li>• More advanced acrobatic maneuvers are possible, including inverted flight.</li> </ul>	<ul style="list-style-type: none"> <li>• Increase complexity, both in terms of control and mechanical development.</li> </ul>

Table 5.2: List of pros and cons of the variable blade pitch propellers.

**Coaxial rotor** The coaxial rotor setup was introduced as an alternative to the conventional main and tail rotor setup on helicopters. It utilizes two contra-rotating propellers, with one placed above the other. Using a coaxial rotor makes it possible to control the yaw moment while still directing all thrust capacity upwards. The downside with coaxial rotors is that the lower propeller is working in the down-wash of the upper propeller, which results in an efficiency loss.

**Simulation** The two comparison alternatives that were used for the three-bladed propeller will also be used for the coaxial rotor configuration. To make this possible, some modifications to the rotor modeling had to be made to account for the down-wash of the upper rotor. A more detailed explanation of these modifications are included in Appendix C.4. During the first simulation, the propellers in the coaxial rotor configuration were of the same size as the reference propeller. As a result of

the down-wash from the upper propeller, the lower propeller usually operates at a higher rotational speed so that the drag moments from the propellers are balanced. Therefore, the rotational speeds for the coaxial propellers have been chosen so that they deviate an equal amount from the reference speed. The ratios from the first simulation can be seen in Figure 5.9

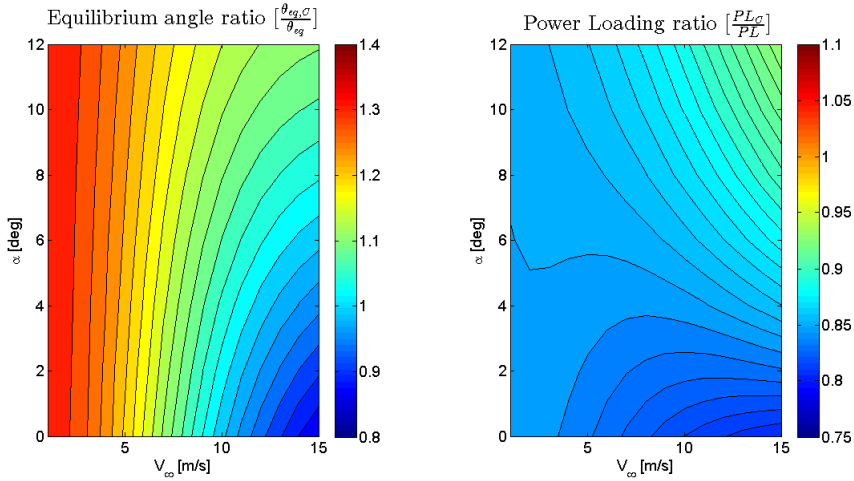


Figure 5.9:  $\theta_{eq}$  and  $PL$  ratio for a coaxial rotor, where the two propellers are of the same size as the reference propeller. The upper propeller is running at 410 rad/s and the lower at 440 rad/s.

For the second simulation, the scaling factor  $K_s$  was used to give the coaxial rotor the same thrust margin  $\beta$  as the reference rotor. Since it is usually the lower propeller that saturates first in a coaxial rotor, it was decided to calculate  $T_{max}$  while the lower rotor was running at the maximum rotational speed and the upper rotor at a speed of 640 rad/s. Thus, cancellation of the yaw moments was ensured. The equilibrium angle and the power loading from the simulation can be seen in Figure 5.10, where the propellers ran at the same rotational speeds as in the first coaxial simulation. The time constant of the coaxial rotor was approximately 50% smaller than the reference propeller.

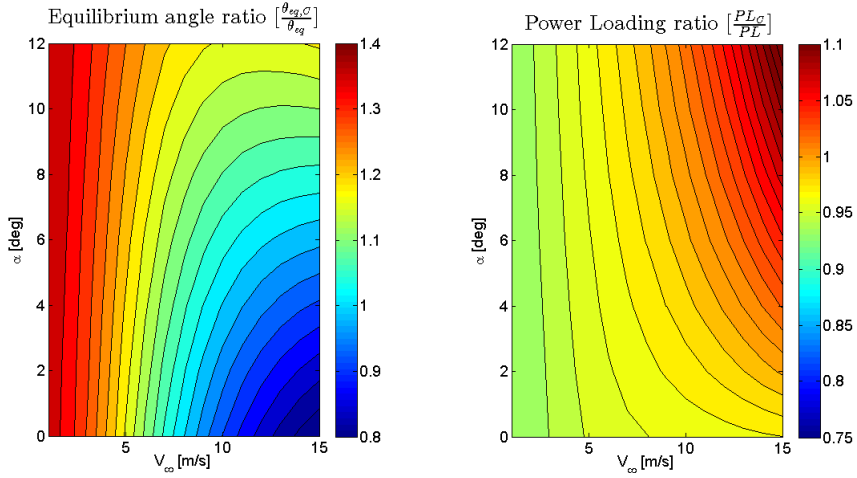


Figure 5.10:  $\theta_{eq}$  and  $PL$  ratio for a coaxial rotor. A scaling factor  $K_s = 0.906$  was used to obtain the same  $\beta$  as for the reference rotor.

**Conclusions** It was predicted that the coaxial rotor would be less efficient than a normal propeller, which was also confirmed by the results in Figure 5.9. However, if the rotor is scaled so that the thrust margin is equal to that of the reference propeller, the power loading is almost as good in hover and even surpasses the reference for high wind magnitudes acting at larger disk angle of attacks. There is not a uniform result for  $\theta_{eq}$ , but it can be seen that the coaxial rotor is less wind resistant for small wind magnitudes while it depends on  $\alpha$  for large magnitudes.

The coaxial rotor option offers a space-efficient way to generate more payload capacity which if utilized, is an advantage during challenging winds. If the radius of the coaxial rotor is instead scaled for an equal  $\beta$  to that of the reference rotor, the time constant of the motor is significantly decreased. This is a great benefit for a multirotor tasked with handling highly turbulent wind.

It is possible to improve the performance of a coaxial rotor by using different settings for top and bottom propellers [20]. However, this is a complicated task and will not be performed in this thesis work.

Coaxial rotors will make the design process a bit more challenging. The lower propellers will make it harder to integrate the landing gear and the camera equipment. They will also more easily interfere with the field of view of the camera.

A tandem propeller configuration is also a possible alternative where partly overlapping propellers will not be as inefficient as a coaxial rotor setup, but on the other

hand will require more space. Tandem propellers can be seen as a compromise between single and coaxial configurations.

To summarize, pros and cons of the coaxial rotor concept are listed in Table 5.3.

PROs	CONs
<ul style="list-style-type: none"><li>• The maximum possible payload is increased for a given rotor diameter.</li><li>• Or, the motor time constant is decreased for a given thrust margin.</li><li>• Allows a more compact airframe design.</li><li>• Doesn't necessarily need another rotor to counter the reaction moment on the airframe.</li></ul>	<ul style="list-style-type: none"><li>• Inefficient, especially in hover.</li><li>• Difficult to model accurately if new control algorithms are to be tested virtually.</li><li>• Difficult to optimize coaxial rotors.</li><li>• Requires a stiffer frame to handle the extra force and weight.</li><li>• More complex integration of landing gear and camera equipment.</li></ul>

Table 5.3: List of pros and cons of the coaxial rotor configuration.

**Ducted fan** A ducted fan is a special kind of propeller that is protected by a shroud. The ducted fans have been used since the 1950s when Alexander Lippisch designed the first prototype for the VTOL aircraft Aerodyne [36]. However, the principle has been used in marine applications for even longer. A quadrotor that utilizes ducted fans can be seen in Figure 5.11.



Figure 5.11: The cyberQuad developed by Cyber technology [41].

**Conclusions** The ducted fan rotor concept offers an interesting approach that may provide a steadier air stream through the rotor disk. However, BET predicts that airflow parallel to the rotor disk is beneficial to rotor efficiency. This effect may be reduced by using ducted fan rotors. On the other hand, the achievable thrust may not fluctuate as much, allowing steadier flight control. The shroud will most likely be a significant drag source at higher wind magnitudes, which will decrease the ability to resist wind.



To summarize, pros and cons of the ducted fan rotor concept are listed in Table 5.4 [36].

PROs	CONs
<ul style="list-style-type: none"> <li>• The maximum possible payload can be increased for a given rotor diameter under certain circumstances.</li> <li>• The shroud acts a structural barrier that protects the blades from the surroundings and vice versa.</li> </ul>	<ul style="list-style-type: none"> <li>• The duct will be a source of aerodynamic drag, which will be significant at higher wind magnitudes.</li> </ul>

Table 5.4: Ducted fan rotor list of pros and cons.

***Inverted propeller placement*** A slightly alternative configuration of a normal propeller is to mount the propeller and its motor beneath the multirotor arm. By doing so, the down-wash of the rotor will no longer be interfered by the DC motor and the arm, which it is mounted on.

***Conclusions*** The airframe and the motors disrupt the induced air flow passing down through the rotor. This effect has not been modeled in this thesis work, but realistically it should be beneficial from an efficiency perspective to place the propeller beneath the arm. The reasoning behind this assumption is that it would be advantageous to interfere with the rotor slipstream before it has passed through the rotor, where the airflow speed isn't as high or concentrated.

Also, by placing the propeller below the arm and the motor, the rotor plane is lowered relative to the CoG of the aircraft. According to the multifactor analysis in Chapter 4, this would be advantageous from a wind resistance perspective. A somewhat marginal side effect of placing a propeller below the motor is that the motor cooling, in the form of the induced airflow, is slightly reduced. Additionally, making an optimal design of the multirotor will be more challenging, considering landing gear and camera equipment integration.

To summarize, pros and cons of an inverted propeller placement are listed in Table 5.5.

PROs	CONs
<ul style="list-style-type: none"><li>• Potentially more efficient.</li><li>• Easier to place the rotor plane lower relative to the CoG.</li></ul>	<ul style="list-style-type: none"><li>• Less efficient motor cooling.</li><li>• More complex integration of landing gear and camera equipment.</li></ul>

Table 5.5: List of pros and cons of the inverted propeller rotor configuration.

**Tiltable rotor** Another possible rotor configuration is to implement a servo motor on the multirotor arm, enabling control of the rotor tilt angle. This will add additional degrees of freedom to the multirotor system. Commonly, this is used for one of the rotors on a tricopter since three normal rotors isn’t enough to fully control the required four degrees of freedom. Also, it is possible to implement an actuator system so that the rotor can tilt around two axes, which would further increase the control possibilities. However, this would require a very complex system design.

**Conclusions** If a multirotor were to use tiltable rotors for all of its arms, forward flight and wind compensation can be achieved without pitching or rolling the body. This has been implmented on a quadrotor prototype by Markus Ryll *et al.* [37], which lead to promising results. Not necessarily having to tilt the multirotor body is generally a very good thing concerning wind resistance, since the airframe drag can be minimized in the horizontal directions. It would most likely also reduce the fluctuation of the drag force acting on the airframe since the exposed area and its drag coefficient will be more or less constant. In addition, it should also be possible to increase the responsiveness of the multirotor while trying to compensate for an applied drag force, depending on the time constants of the servo motors. Tilting the rotors instead of the entire body should also provide a steadier platform for aerial video and photography.

To summarize, pros and cons of the tiltable rotor configuration are listed in Table 5.6.

PROs	CONs
<ul style="list-style-type: none"> <li>• Adds additional degrees of freedom.</li> <li>• Increased maneuverability.</li> <li>• Forward flight possible without rotation of the aircraft body.</li> </ul>	<ul style="list-style-type: none"> <li>• Servo motors add to the cost and complexity.</li> <li>• Multirotors with tilting rotors needs more complex control algorithms.</li> <li>• Difficult to model accurately if new control algorithms are to be tested virtually.</li> </ul>

Table 5.6: List of pros and cons of the tilting rotor configuration.

**Varying rotor sizes** Using propellers with varying dimensions is an unconventional approach to multirotor design. It has been successfully implemented by [9], where the aim was to increase the flight time for operations close to hover.

**Conclusions** Using differently sized rotors may prove beneficial depending on the purpose of the design. If theory predicts an improved performance with a large main rotor, as was the case in [9], then it can certainly be worth the added implementation difficulties. However, considering the aim of this thesis and the previously mentioned conclusion that smaller and faster spinning propellers are desirable, there is no evident reason to use anything but small propellers of the same size.

To summarize, pros and cons of utilizing differently sized rotors are listed in Table 5.7.

PROs	CONs
<ul style="list-style-type: none"> <li>• Greater design flexibility.</li> <li>• Can improve efficiency under certain circumstances.</li> </ul>	<ul style="list-style-type: none"> <li>• Harder to balance yaw moment and more "unknown" constants are introduced in the control algorithm.</li> <li>• Varying motor time constants further complicates the control algorithm implementation.</li> </ul>

Table 5.7: Varying sizes of rotor list of pros and cons.

## Airframe configurations

During this section, different airframe configurations will be discussed and compared. For simplicity, only one type of rotor will be considered during this study. The airframes will be sorted after their conventional number of rotors.

### Quadrotor

This part will cover multirotor airframes that normally utilizes four rotors.

**I4/X4 config.** The I4/X4 quadrotor configuration, shown in see Figures 5.12 and 5.13, is the most common airframe option for multirotors. It will here serve as an overall design reference to which other designs concepts will be compared. The quadrotor can be used either with an I configuration or a X configuration depending on how the arms are oriented relative to the front of the multirotor. The different configurations have slightly different flight characteristics for a given flight direction, but will not have any significant impact on the overall performance of the multirotor. The X configuration is better suited for aerial photography.

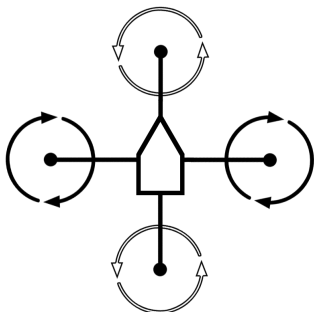


Figure 5.12: Quadrotor: I4 config.

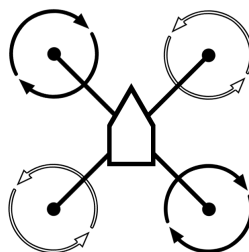


Figure 5.13: Quadrotor: X4 config.

**H4 config.** The H4 quadrotor is an alternative frame configuration and is shown in Figure 5.14. It can be seen that the arms do not coincide in a single point as for the standard quadrotor.

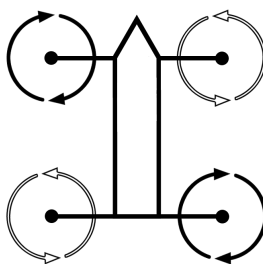


Figure 5.14: Quadrotor: H4 config.

**Conclusions** The H4 provides some benefits for specific applications such as aerial photography. However, it will be slightly harder to optimize the CoG placement which can reduce the stability of the vehicle. The H4 configuration will also have slightly different flight characteristics, but it is hard to predict how much of an impact this will have on the overall performance. Drag forces that are caused by the airframe in the x- and y-directions of the body frame will differ due to the rectangular design. Therefore, it might be worth implementing a yaw control which forces the front of the quadrotor to face the incoming wind in certain situations.

Pros and cons of the H4 configuration, compared to the standard quadrotor configuration, are listed in Table 5.8.

Pros	Cons
<ul style="list-style-type: none"> <li>• Better for aerial photography.</li> <li>• More space to place battery and equipment.</li> </ul>	<ul style="list-style-type: none"> <li>• Slightly more difficult to balance the center of gravity.</li> <li>• Behaves differently depending on the direction of the wind.</li> </ul>

Table 5.8: H4 list of pros and cons.

**V-Tail config.** The V-Tail is an unconventional quadrotor design with only three arms, as shown in Figure 5.15, which can potentially reduce the airframe drag. It utilizes a rear rotor configuration with two tilted rotors to achieve yaw control.

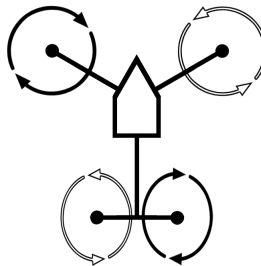


Figure 5.15: Quadrotor: V-Tail config.

**Conclusions** The V-Tail is a slightly more complex configuration than the regular quadrotor configurations. It is a good choice if more responsive yaw control is required, which is accomplished by the two rotors that are tilted with a fixed angle. This means that yaw control moment isn't limited to the reaction moments from the DC motors. The drawback of this solution is that it reduces the potential upward thrust of the multirotor. This issue may also be worsened by the interference of the rear rotors.

Pros and cons of the V-tail configuration, compared to the standard quadrotor configuration, are listed in Table 5.9.

Pros	Cons
<ul style="list-style-type: none"><li>• Improved yaw control.</li><li>• Potentially reduced airframe drag.</li></ul>	<ul style="list-style-type: none"><li>• Potential thrust is limited by the tilted rear rotors.</li><li>• Rear rotors will most likely interfere with each other which results in an efficiency loss.</li></ul>

Table 5.9: V-tail list of pros and cons.

**Trirotor**

This part will cover multirotor airframes that normally utilizes three rotors. However, this is not enough to provide the necessary means of control. For stable flight, at least four DoF is required which is commonly achieved by implementing a servo motor on one of the arms.

**Y3 config.** The Y3 tricopter is the standard configuration for trirotors. It can be viewed in Figure 5.10, where the arrow around the rear arm indicate the use of a servo that ensures yaw control.

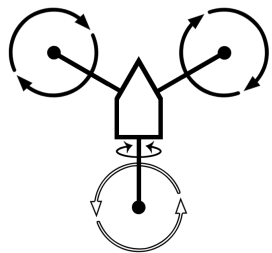


Figure 5.16: Tricopter: Y3 config.

**Conclusions** With only three arms there is a possibility to make the design more compact because of the increased spacing between the rotors. The drag force acting on the airframe can therefore be reduced. It is also predicted that the drag coefficient will be reduced as a result of fewer arms. Naturally, the trirotor can't handle much payload because of the limited amount of rotors. However it can be a suitable platform for small-scale camera equipment since the unobstructed field of view is increased. The trirotor is popular among hobbyists since it has a different "feel" while flying manually.

Pros and cons of the Y3 configuration, compared to the standard quadrotor configuration, are listed in Table 5.10.

Pros	Cons
<ul style="list-style-type: none"> <li>• Reduced airframe drag.</li> <li>• Less likelihood of rotors being affected by one another and by the airframe itself.</li> <li>• Only three arms leaves space for a wide camera angle.</li> </ul>	<ul style="list-style-type: none"> <li>• Either servo or additional rotors are necessary to obtain full controllability.</li> <li>• Less stabilization authority.</li> <li>• Poor payload capabilities.</li> </ul>

Table 5.10: Y3 list of pros and cons.

**T3 config.** The T3 tricopter is an alternative trirotor configuration, which is depicted in Figure 5.17. The arms doesn't coincide in the CoG as in the case of the Y3 configuration.

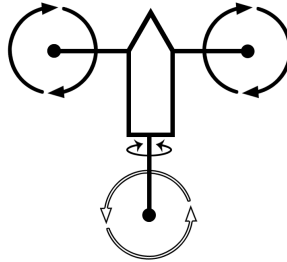


Figure 5.17: Tricopter: T3 config.

**Conclusions** Just as with the H4 configuration, this concept is mainly beneficial for special applications. The T3 configuration is for example advantageous if servo motors are implemented on all of the arms, since no rotors will counteract each other. In theory, however, this concept will be considered as slightly inferior to the standard Y configuration because of its unsymmetrical design.

Additional pros and cons to those of the standard trirotor Y3 configuration are listed in Table 5.11.

Pros	Cons
<ul style="list-style-type: none"><li>• Even wider camera angle during aerial photography.</li></ul>	<ul style="list-style-type: none"><li>• Slightly more difficult to balance the center of gravity.</li><li>• Behaves differently depending on the direction of the wind.</li></ul>

Table 5.11: T3 list of pros and cons.

**Hexacopter**

This part will cover multirotor airframes that normally utilizes six rotors.

**I6/X6 config.** As for the quadrotor, the hexacopter can also be designed with either an I or a X arm configuration, see Figure 5.18. Similarly, a slight difference in flight characteristics is present due to the arms' placement relative to the front of the aircraft. This difference is even more marginal for the hexacopter since the total thrust is distributed more evenly around the center of the multirotor.

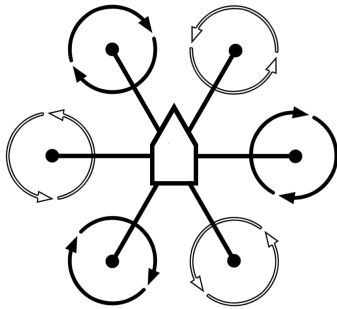


Figure 5.18: Hexacopter: X6 config.

**Conclusions** Hexacopters are generally used when quadrotors aren't strong enough or when some limited redundancy is required because of expensive equipment. The extra payload capacity comes at the price of increased drag forces on the airframe. The airframe can not be made as compact as those with fewer arms due to rotor spacing. The projected surface area will therefore increase and the effective drag coefficient will most likely also increase because of the increased number of arms that the wind has to bypass. It is, however, hard to analytically determine exactly how much the overall drag will increase. The additional motors and arms will increase the overall mass and inertia of the multirotor which will increase the translational and rotational stability, but somewhat limit the agility of the aircraft.

Pros and cons of the I6/X6 configuration, compared to the standard quadrotor configuration, are listed in Table 5.12.



Pros	Cons
<ul style="list-style-type: none"> <li>• Limited redundancy.</li> <li>• Larger payload capacity.</li> <li>• Generally more stable with respect to rotation and translation.</li> </ul>	<ul style="list-style-type: none"> <li>• Increased airframe drag.</li> <li>• Generally not as agile.</li> </ul>

Table 5.12: I6/X6 list of pros and cons.

### Octorotor

This part will cover multirotor airframes that normally utilize eight rotors.

**I8 config.** The I8 octorotor is the standard configuration for airframes with eight rotors and can be viewed in Figure 5.19. The octorotor is generally used when the requirement on payload capacity is highly demanding. The chances of a safe return in case of motor failure is also significantly increased. Pros and cons of the I8 configuration, compared to the standard quadrotor configuration, are basically the same as those for the hexacopter, only magnified. Hence, no new list and conclusion is included.

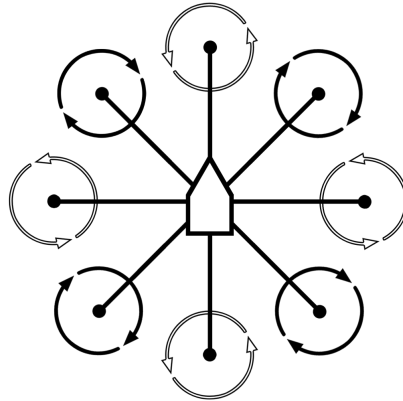


Figure 5.19: Octorotor: I8 config.

**V8 config.** The V8 configuration is an unconventional octorotor design where the rotors are distributed evenly on either side of the center, see Figure 5.20.

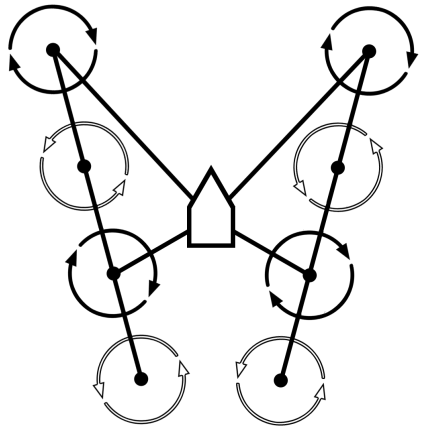


Figure 5.20: Octorotor: V8 config.

**Conclusions** The V8 is a slightly more complex design with some advantages for special applications. It is beneficial for larger camera equipment, thanks to the payload capabilities and the wider unobstructed field of view. As mentioned previously, the unsymmetrical design will make it slightly harder to balance the CoG properly. The vehicle will also react differently to wind from various directions.

Additional pros and cons to those of the standard octorotor configuration are listed in Table 5.13.

Pros	Cons
<ul style="list-style-type: none"><li>• Wide camera angle.</li></ul>	<ul style="list-style-type: none"><li>• Slightly more difficult to balance the center of gravity.</li><li>• Behaves differently depending on the direction of the wind.</li></ul>

Table 5.13: V8 list of pros and cons.

## 5.2 Concept evaluation

This section aims at presenting a favorable multirotor concept able to withstand wind. This is achieved by combining the previously presented rotor and airframe assessments, after which a concept generation and scoring process is performed. To this end, a number of chosen design criteria are given a relative weighting which are used to rate a number of concepts generated by the authors.

### Design criteria

Before any concepts are presented, a set of criteria is established for which each concept will be rated on a scale of 1 to 10. Each criteria is accompanied by a relative weight to signify its importance to the aims of this thesis. Apart from wind resistance, flight time was also considered an important factor for mission performance. This is reflected in the moderately high weighting of efficiency.

- **Cost and complexity [0.05]**

Rates the implementation simplicity and availability of the airframe design. Issues such as CoG balancing are considered as well as the required amount of material and components such as arms, motors and cabling. Along with these considerations, the modeling and control complexity is also taken into account. A low rating on this criteria indicates high levels of cost and complexity. Since it is assumed that any possible production of a proposed design will be small-scale, both cost and complexity will be given roughly equal significance.

- **Wind resistance [0.45]**

Considers how favorable a design is regarding its ability to withstand and minimize forces and moments caused by the onset of wind. Typically, the projected surface area, aerodynamic drag coefficient, number of rotors and payload capacity will have an influence on this criteria.

- **Maneuverability [0.10]**

The agility of the aircraft along the six degrees of freedom is rated by this criteria. Increased mass and moment of inertia will limit the ability to perform aggressive maneuvers. However, additional rotors around the CoG will increase the attainable thrust and actuated moments, improving maneuverability. Adding tilting rotor servos will open up further control possibilities not otherwise achievable.

- **Efficiency [0.25]**

Increased efficiency of the aircraft is pivotal to maximizing the flight time. Larger rotors operating at low speeds are generally more efficient, whereas

coaxial rotors will suffer from some efficiency loss. Other factors that influence this criteria are the unloaded aircraft weight and the drag exposure, including number of rotors and airframe design.

- **Redundancy [0.10]**

The ability to maneuver the aircraft in the case of motor or rotor malfunction is considered by this criteria. Redundancy may be achieved by use of additional rotors as well as placing them appropriately around the airframe. Designs with several rotors will not suffer as much thrust margin loss as those with fewer in case of rotor malfunction. Additionally, designs with fewer rotors may even suffer loss of control caused by an insufficient number of actuated degrees of freedom. It should, however, be kept in mind that an increase in rotors will also increase the likelihood of rotor failure.

- **Aerial photography [0.05]**

For photography and video capturing purposes, it is important that the propellers and arms do not interfere with the camera view. This criteria rates the ease of a satisfactory camera system implementation on the multirotor, as well as its ability to carry additional payload introduced by such systems.

To make the following concept comparison as fair as possible, a number of constraints have been introduced. These are listed below.

- All of the concepts will have the same thrust margin  $\beta = T_{max}/(mg)$ .
- The minimum horizontal distance between the tips of any two propellers are limited to  $R$  to avoid unwanted rotor wake interaction [16].
- All multirotor concepts, that use equally sized propellers, will have the same propeller dimensions.
- All concepts will use the same control algorithm. The response time of the control algorithm is determined by the size of the rotor so that a tuning factor  $N$  is achieved relative to the actuator response time (See Chapter 3).

With design criteria defined, the following sections will present the generated concepts. Each concept is described thoroughly and given a rating for each of the design criteria.

### X4 quadrotor [X4]

The quadrotor is the traditional multirotor configuration concept. It is mechanically simple and proven, and will serve as a reference concept during the concept scoring.

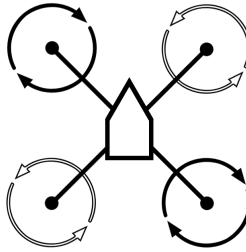


Figure 5.21: The X4 concept is a standard quadrotor configuration, used as a reference concept.

**Cost and complexity [10]** The quadrotor has had great success thanks to its relatively low cost and complexity. Four is the lowest amount of rotors needed for sufficient controllability, without adding additional complexity in the shape of servo motors. Since the quadrotor is the most common platform, it is easy to obtain various information regarding design considerations and control.

**Wind resistance [5]** The airframe of the quadrotor has four arms, yielding a compact design with moderate airframe drag. Four rotors provide sufficient thrust for a smaller payload, granting some stability and resistance to the onset of wind.

**Maneuverability [5]** The conventional quadrotor can be quite agile due to its relatively low inertia, while only using four rotors.

**Efficiency [7]** The quadrotor utilizes regular rotors, which provide good efficiency. It will have a rather low unloaded weight and unnecessary drag exposure thanks to few components such as arms and motors.

**Redundancy [1]** If a rotor is lost, crash is virtually unavoidable. A fourth of the total lifting force as well as control of both attitude and position is lost, highlighting the severity of such a situation. Therefore, the quadrotor is not considered a redundant system.

**Aerial photography [5]** The quadrotor is quite suitable for aerial video and photography. However, integrating heavier equipment in the total mass may require more payload capability.

## Y6 three-armed frame with coaxial rotors [Y6]

The Y6 concept features a three-armed airframe with coaxial rotors attached to each arm and is known among hobbyists for its wind robustness. The coaxial rotors provide means to achieve yaw control, which eliminates the need for a servo controlled rotor or tail rotor.

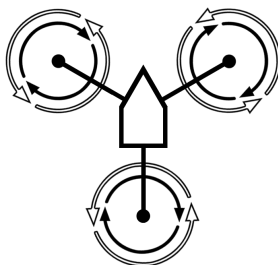


Figure 5.22: The Y6 concept has a three-armed airframe and coaxial rotors.

**Cost and complexity [5]** The coaxial rotors of this concept has some drawbacks when it comes to both cost and complexity. Since the upper and lower rotors provide different thrusts and drag moments, it may be slightly more difficult to optimize the control and design of the rotors. In addition, coaxial rotors are more difficult to model accurately in a simulation environment. The three-armed airframe requires less material, whereas the coaxial rotors will introduce additional motors and propellers. It should be noted that the airframe arms will have to be made slightly stiffer than otherwise and that the utilization of coaxial rotors will complicate the integration of landing gear.

**Wind resistance [9]** The airframe used in this concept will be of some benefit compared to the X4 reference. Due to fewer and shorter arms, it is possible to make it more compact and less susceptible to airframe drag. Utilizing coaxial rotors will enable additional payload capacity useful in wind, but it should be kept in mind that each added rotor is a source of additional drag.

**Maneuverability [5]** The Y6 suffers from a slight increase in inertia due to added motors, but this is somewhat compensated by a reduced arm length. Its ability to produce rolling and pitching moments is, however, increased by the presence of additional rotors. Thus, it is hard to arbitrarily determine how the maneuverability of the Y6 compares to the X4. Hence, it was concluded that this concept would receive the same rating as the X4 reference.

**Efficiency [3]** The unloaded weight of the Y6 will likely be slightly increased compared to the X4 reference, although the Y6 has one arm less. This is due to the

added motors and rotors. However, the main efficiency loss is caused by the coaxial rotors. Since the lower rotors operate in the wakes of the upper, more power is used per generated thrust. Additionally, the airframe is likely to be exposed by less drag, yielding some benefits in forward flight.

**Redundancy [7]** Losing a rotor will essentially result in a significant decrease in attitude control performance. Depending on the predetermined thrust margin and flight conditions, the aircraft may still be landed safely either manually or by an emergency control allocation routine. The lost thrust due to rotor failure will be limited to less than a sixth of the total thrust since three of the rotors will always operate without downwash disturbance.

**Aerial photography [6]** The three-armed airframe leaves a lot of space, which allows a wide field of view for the camera without interfering propellers. The coaxial rotors, although providing some additional payload capacity for heavier equipment, may cause some interference of the view depending on where the camera is directed.

### X6 hexacopter [X6]

This concept employs a six-armed frame configuration with a single rotor placed on each arm. It is similar to the design that Combine Control Systems currently use. The six rotors provide additional payload capacity, but placing them with sufficient spacing yields a larger airframe.

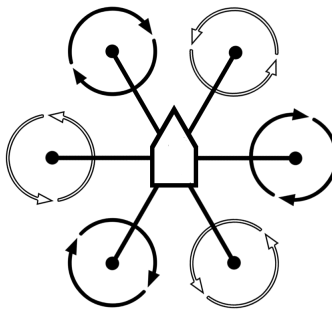


Figure 5.23: The X6 concept has a six-armed airframe with rotors placed beneath the arms.

**Cost and complexity [7]** The X6 suffers from high material cost. It has a large airframe due to additional arms, which have to be long enough to provide necessary rotor spacing. Additionally, the six rotors introduce an increased number of motors and propellers.

**Wind resistance [6]** Six rotors provide a larger payload capacity, which stabilizes flight in windy conditions. However, the airframe of the X6 will be significantly larger than those of the previous concepts, which in combination with added rotors, results in an increased overall drag.

**Maneuverability [5]** Similarly to the discussion on the Y6 maneuverability, the X6 will receive the same rating as the X4 reference. The concept does provide means to produce larger attitude moments, but also has a larger inertia an increased number of longer arms.

**Efficiency [6]** Since the regular single rotor configuration is employed, the X6 will be rather efficient. However, the unloaded weight of the X6 is increased due to the six-armed frame and the addition of extra components such as arms and motors. The large airframe of this concept will likely be a source of significant drag, requiring extra thrust to compensate for during forward flight.

**Redundancy [6]** Similarly to the Y6 concept, rotor loss will essentially result in a significant decrease in attitude control performance, but with some additional thrust loss.

**Aerial photography [4]** The presence of additional arms, which will generally be longer, and propellers will cause some obstruction of the camera view in forward flight. The added payload capacity will, however, enable integration of heavier equipment.

### **X4 quadrotor with servo-tiltable rotors [X4S]**

The last proposed concept has a simple quadrotor airframe, but with the added functionality of servo-tiltable rotors. The servos gives additional actuation options for a control algorithm and enables simultaneous control of all six degrees of freedom. An important aspect to consider for this concept is the increased complexity.

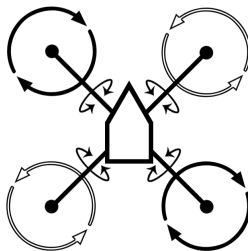


Figure 5.24: The X4S with tiltable rotors concept has a standard quadrotor frame but with rotors that can be tilted by DC servos.



**Cost and complexity [3]** Although the airframe itself is of the simple quadrotor design, the introduction of servo-tiltable rotors yields a considerable increase in both cost and complexity. The added servo motors themselves add to the material cost, whereas mechanical implementation add to the complexity. In addition, extending the multirotor model to include the servo functionality and developing a suitable control algorithm may prove difficult. With these considerations in mind, the X4S concept is rated rather low for this criteria.

**Wind resistance [8]** As for the regular quadrotor, this concept's airframe will result in moderate airframe drag during the onset of wind. Since servo-tiltable rotors are used, the airframe will mainly be exposed to wind in its horizontal plane. Utilizing this, the horizontal properties of the airframe can be aerodynamically optimized to decrease the overall drag. In addition, the tilting of the rotors can be actuated faster than rotation of the entire airframe, provided the servo motors are sufficiently powerful. This will therefore yield a faster response to rapidly varying wind conditions.

**Maneuverability [8]** Servo-tiltable rotors allow simultaneous control of all six degrees of freedom, enabling maneuvers not possible for regular multirotors. Also, as previously discussed, tilting just the rotors to achieve forward flight may be done faster than rotating the entire airframe like fixed-rotor concepts do. With these considerations in mind, the X4S concept is considered highly maneuverable.

**Efficiency [5]** Despite the presence of added unloaded weight from the servo motors, the X4S may still provide average efficiency thanks to its ability to tilt its rotors. Positive effects resulting from this ability are most evident in forward flight, where the airframe drag may be minimized and the need to rotate the entire airframe is eliminated. However, it should be kept in mind that the added servo actuators continually require power to control the attitude.

**Redundancy [1]** In the even of rotor failure, attitude control will likely be lost as well as a significant amount of the total thrust. Thus, the X4S is not considered to be redundant with crash being an inevitable outcome. In case of servo motor failure, the aircraft may still be operated safely although some emergency control routine reallocating servo actuation to rotor speed would be needed.

**Aerial photography [6]** The quadrotor frame is quite suitable for aerial video and photography, where the X4S draws further benefit by using its servo tiltable rotors. These will enable forward flight without rotation of the airframe, thus reducing obstruction from the arms as well as the required effort by a camera stabilizer. However, integrating heavier equipment in the total mass may require more payload capacity than the X4S can provide.

## Results

The results from the concept scoring are presented in Table 5.14. The criteria ratings for each generated concept are denoted as **R**, which are multiplied by a weighting factor to yield an overall weighted score **WS**.

Criteria	Weight	X4		Y6		X6		X4S	
		R	WS	R	WS	R	WS	R	WS
Cost & complexity	0.05	10	0.50	5	0.25	7	0.35	3	0.15
Wind resistance	0.45	5	2.25	9	4.05	6	2.70	8	3.60
Maneuverability	0.1	5	0.50	5	0.50	5	0.50	8	0.80
Efficiency	0.25	7	1.75	3	0.75	6	1.50	5	1.25
Redundancy	0.1	1	0.10	7	0.70	6	0.60	1	0.10
Aerial photography	0.05	5	0.25	6	0.30	4	0.20	6	0.30
<b>Total score</b>			5.35		6.55		5.85		6.20
<b>Rank</b>			<b>4</b>		<b>2</b>		<b>3</b>		<b>1</b>

Table 5.14: Concept scoring for the four generated design concepts.

## 5.3 Proposed design

From the concept scoring results in Table 5.14, it is clear that the Y6 is a preferred concept along with the X4S. It was concluded that the proposed design concept of this thesis will be a fusion of the Y6 and X4S concepts, combining the strengths of each concept to provide a preferable design. Such a fusion design may look like in Figure 5.25. Considering that the UAV will constantly be in forward flight for the suggested applications, adding a wing-like airframe structure granting additional lift might be a consideration to improve flight time. Since it was deemed too time-consuming to model and control the key features of both the Y6 and the X4S accurately it was, however, decided to move forward with just the Y6 in this thesis work.

The Y6 concept employs a coaxial rotor configuration. Although proving to be less power-efficient, such rotors enable a smaller airframe with fewer arms while also providing about 20 % extra payload capacity compared to a standard quadrotor. Since the three-armed airframe can be also made smaller than for the X4 and X6 concepts, a larger portion of the mass can be placed in the center. It can be argued that the center mass is the most "useful" mass, since it is typically where equipment such as onboard electronics and battery is carried.

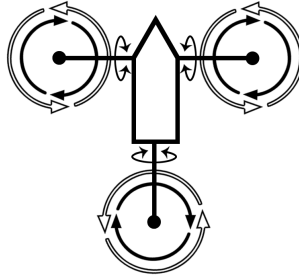


Figure 5.25: Combining the beneficial features of the Y6 and X4S concepts may yield a superior design.

The DOE multifactor analysis in Chapter 4 indicated that a reduced airframe size will have positive effects on both wind resistance capabilities and energy consumption. This suggests that a compact design is beneficial. However, the multirotor can not be made arbitrarily small since it needs a reasonable arm length to actuate moments for attitude control. Placing the rotors in too close proximity to each other will also cause interaction between the rotor slipstreams [16]. To stay clear of this unwanted effect, it was concluded that the arms must be long enough so that the distance between the blade tips of any two rotors is at least one rotor radius. For different frame configurations, this will lead to different lower limits of the arm lengths. Because of this, the three-armed frame of the final Y6 will have shorter arms than otherwise possible for the X4 or X6 designs, yielding reduced projected surface areas resulting in lower exposure to wind drag force.

Also, the DOE showed that the total mass had great significance to withstanding wind. The downside of a high mass was shown in regards to the power consumption and, obviously, the mass can not be made too large anyway since the thrust from the rotors must be enough to lift the aircraft and perform maneuvers while maintaining altitude. It was concluded that the total mass of the aircraft  $m_{tot}$  must respect a minimum thrust margin of  $\beta$ , so  $T_{max} \leq \beta m_{tot} g$ .

Lastly, another finding of the DOE analysis showed that the points at which the airframe drag and the rotor forces act are significant to minimizing the position error. Attempting to place them as close to the center of gravity as possible will minimize any moments, since the levers of these are reduced. But even more benefit can be achieved if these points are situated slightly below the center of gravity. The forces would then act to tip the aircraft slightly into the wind, directing a portion of the thrust against the wind forces without any controller action. To take advantage of these effect, the arms are attached as low as possible on the center.

To summarize, combining the final Y6 design concept with the findings from the DOE analysis yields a favorable design. The desired reduction of the airframe size

is clearly accommodated by the Y6's three-armed frame due to fewer and shorter arms. The six rotors, configured coaxially, enable some extra total mass although the extra motors and rotors will be sources of additional airframe and rotor drag forces. A possible final product may look like in Figure 5.26, which has been designed with CAD and imported into SimMechanics.

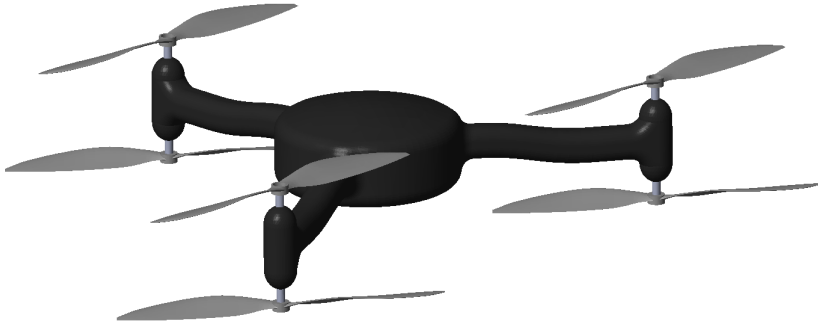


Figure 5.26: Y6 configuration shown in the graphical interface of SimMechanics.

# 6

## Performance comparison

In an attempt to demonstrate the advantages of the proposed Y6 design from Section 5.3, a Y6 and two X4 configurations have been assembled in the model simulator in order to compare their respective performance. In Table 6.1, these designs are listed with their most relevant specifications. The two X4 designs represent the parameter combinations that provided the best wind rejection (X4W) and power consumption (X4P) in the multifactor optimization from Section 4.1. They are compared to the Y6 design, which is configured to have the same thrust margin  $\beta$  as the wind resistant X4W. Along with this, a dimensioning principle has been applied to ensure equal rotor spacing. Thus, the Y6 and X4 will have different airframe projected surface areas where the same drag coefficient  $C$  has been assumed.

Specifications	Y6	X4W	X4P
Total mass	1.80 kg	1.50 kg	1.0 kg
Projected surface areas $A_x, A_y, A_z$	0.02, 0.02 0.03 m <sup>2</sup>	0.02, 0.02 0.04 m <sup>2</sup>	0.02, 0.02 0.04 m <sup>2</sup>
Thrust margin $\beta$	1.83	1.83	2.75

Table 6.1: Design specifications for Y6, X4W and X4P.

The designs listed in Table 6.1 are run in the simulator with a wind scenario designed to test each designs' ability to handle shorter and longer wind gusts, rotation of the horizontal wind angle and turbulence. The wind test is shown if Figure 6.1, where each line shows the wind in one of the inertial directions. When running the designs through the simulator, the cascaded PID controller has been tuned such that the positional control has a bandwidth  $\omega_{BW} \approx 1$  rad/s, enabling basic levels of turbulence and wind variation robustness.

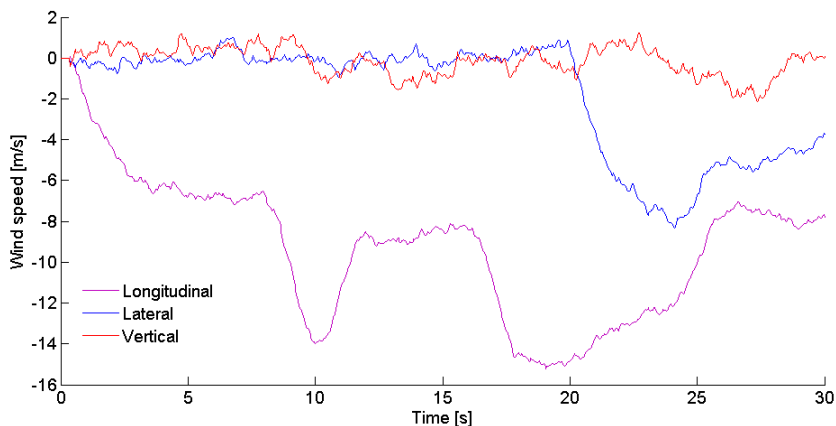


Figure 6.1: Wind test designed to test the performance of each multirotor design listed in Table 6.1. Note the legend showing which wind direction corresponds to which line color.

Resulting simulation performances for each design are summarized in Table 6.2 and in Figure 6.2. The simulations shows that the Y6 has an approximate performance increase of 10 % compared to the X4 optimized for wind resistance in regards to holding its position. This is put down to a number of factors. Firstly, its airframe is reduced, resulting in a smaller projected surface areas. With the same drag coefficients  $C$  assumed for the designs, this is clearly a favorable attribute. Secondly, the mass is increased, decreasing the acceleration due to the onset of forces. Due to the increased number of rotors of the Y6, there will be additional rotor disturbance forces, but this is what enables the added mass. Lastly, the effective levers to the centroid and resultant lever of the rotors is reduced greatly because of the construction with motors and rotors attached beneath the arms. Note that all of these effects were showed to be influential in the DOE analysis in Chapter 4 and discussed at length in Section 5.3.

Also worth noting from the performance comparison in Table 6.2 is the differences in both power consumption and mass lifting efficiency. The X4P design, which was shown to be optimal in regards to power-consumption, has superior efficiency performance. Thus, it is clear that resistance comes at a price of efficiency, where a suitable trade-off must be made.

Since the simulator doesn't accurately predict drag forces, as discussed in Section 2.4, and the fact that it would be difficult to achieve the same levels of control and sensor feedback as in this idealized simulator, the results will likely not be the same as if tested in reality. Especially the uncertainty that arises when comparing different airframes is a major drawback of the comparison performed in this section, as the

Performance	Y6	X4W	X4P
Max pos. error $e_{max}$	8.14 cm	9.30 cm	14.81 cm
Mean pos. error $e_{mean}$	3.34 cm	3.79 cm	5.61 cm
Mean power consumption $P_{mean}$	102 W	76 W	37 W
Power per mass $P_{mean}/m_{tot}$	57 W/kg	51 W/kg	37 W/kg

Table 6.2: Design performance comparison.

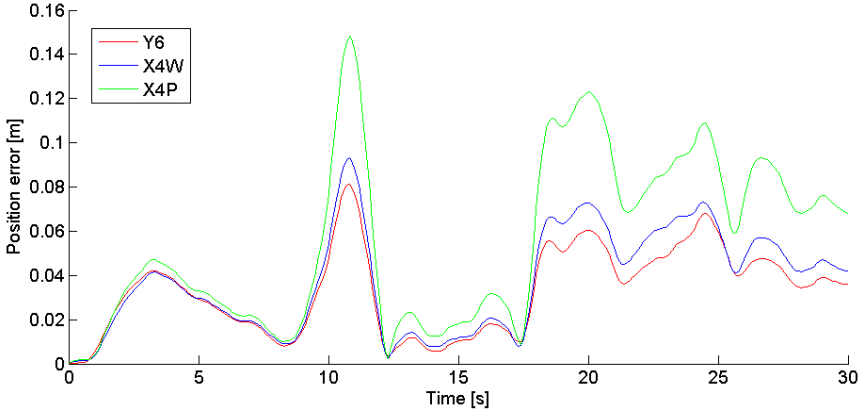


Figure 6.2: The position error norms for the proposed Y6, X4W and X4P designs during the wind performance test.

real drag coefficients were not possible to predict. Thus it is unclear how much of an advantage the smaller Y6 airframe has in regard to drag forces and how much the rotors' downwash affect this. Although it is dangerous to jump to conclusions on this issue, it is believed by the authors that that a smaller airframe with fewer arms will result in less drag force.

In order to achieve a more accurate comparison, tools not available to and methods out of the scope of this project must be applied. These could possibly include wind-tunnel testing and CFD analysis of the airframe especially, but also the rotors for horizontal airflow. Applying methods like these, further conclusions may be made about the advantages of each designs. Also, modeling of sensors, real-time implementation aspects and other non-ideal effects not investigated by this thesis work, will likely increase the realism of the results.

# 7

## Summary and conclusions

As discussed when formulating the aims of the thesis work, it has been attempted to provide a favorable multirotor UAV design for autonomous missions in challenging wind conditions. The goal was to be achieved using a model- and control-based design approach. The design of such an UAV is of great interest to the overall desire to design multirotors suitable for aiding in search and rescue missions. Attaching a thermal camera to the UAV would provide a powerful tool for such applications. During missions when, for instance, searching for a missing person in the woods, it is considered unacceptable that worsening weather conditions jeopardizes the ability to use the multirotor.

To these ends, an advanced aerodynamic multirotor model, based on theory normally used for modeling of helicopters [19, 35], has been assembled and implemented in a simulator environment. The model attempts to predict thrust and drag moment variations in different flight states (hovering, vertical and forward flight) by combining an air inflow model based on momentum theory with blade element theory, where thrust, horizontal force and drag moment is derived and integrated for each blade section. In addition, the blade flapping phenomena was modeled to account for the tilting of the rotor in both the longitudinal and lateral directions, deflecting the rotor forces.

Using data from the UIUC propeller database [4] some validation could be made for the axial and hover flight states, which, after some parameter tweaking, showed promising agreement. To validate the rotor model further, it is suggested that a series of wind tunnel tests are performed for forward flight. Without further validation, the model must still be considered sufficient since it is based on well regarded theory. It is anticipated by the authors that it at least captures the main flight dynamics of the rotor. The airframe model, used to apply drag forces, is, however, of low validity since it was not possible to decide the drag coefficient  $C_d$  for a complex multirotor body. Compared to the rotor forces, an aerodynamically favorable airframe will likely have a limited contribution to the total drag acting on the aircraft.

Along with the actual aerodynamical multirotor model, modeling of wind characteristics have been of central interest. Wind gusts and variations have been modeled



and implemented using the Dryden wind turbulence model and standardized mathematical gust representations. Using this to create suitable wind test scenarios, it was decided to not make the wind too strong since the rotor model validation indicated less data compliance for high rotor inflow speeds. Considering this as well as the low validity of the airframe model, it was decided to not conduct a maximum wind test to test the upper limits of a multirotor design. Instead, evaluating designs for moderately high winds was decided to be sufficient to draw conclusions regarding performance at even larger wind velocities. When dimensioning a final multirotor, the required wind tolerance must be decided, which includes choosing a suitable thrust margin and arm length to avoid motor saturation. To further prevent saturation, a more refined control algorithm may be implemented that, for example, temporarily allows some positional deviation during the most extreme wind gusts.

Finalizing the simulator, a PID cascaded controller was designed and tuned to control the position of the multirotor. The overall control architecture was designed such that an outer controller controls the position, sending references to the inner attitude controller. A control allocation scheme was then used to actuate the actual motors in the simulator. Analysis of the control performance was achieved by using a simplified and linearized model for control design. Disturbance analysis has then been made where the closed-loop responses of the linearized model are analyzed. The Bode plot bandwidths and response times of these responses were discussed in relation to the modeled wind turbulence, predicted by the Dryden wind turbulence model.

The modeled simulator was made such that dimensions and masses of various multirotor parts are scalable. Enabling this, an optimization software was used to access the simulator externally, running it with a specified wind test for different parameter setups. After a large number of simulations (using different setups determined by a design of experiments), each parameter's influence on position error and power consumption were determined by linear and quadratic regression models respectively. The results indicated a trade-off between these criteria.

Finally, a design development methodology has been applied to generate a suitable design concept. A wide variety of airframe and rotor configurations have been assessed from which a small set of multirotor concepts were generated with a pre-determined set of criteria in mind. It was concluded that the wind resistance criteria was of utmost importance, followed by power efficiency, when generating these concept. The generated concepts were compared through a concept scoring process where the final score was based on the results from the multifactor analysis, the rotor and airframe assessments, logical reasoning and inspiration from on-going research and community discussions. It was concluded that a three-armed multirotor with six propellers configured coaxially (Y6) would be the most beneficial, possibly with the modification of added servo-tiltable rotors. In the conducted simulations,

the different concepts modeled showed limited impact on performance and may in reality play a larger role, especially in regards to airframe drag. It will invariably be the physical properties of a multirotor that defines its flight behavior, whereas different concepts merely provide means to manipulate these properties. Choosing a specific concept introduces both possibilities and boundaries to how much the physical properties may be altered.

Because of the uncertainties in the model, the ability provide accurate performance data is limited. An attempt was however made, showing the superiority of the final design within the simulated environment. It should be stated that this project was performed on a conceptual level, not considering implementation aspects such as sensor readings and real-time constraints, which will likely be of significance in reality. It is, however, assumed that the evaluated designs in this report are affected similarly by these aspects, thus not affecting their relative performance.

# 8

## Future work

This project has touched on a number of different engineering principles such as control, mechanics, electronics, aerodynamics, design development and multi-objective optimization. Hence, there are also a lot of possible directions in which a succeeding project might proceed.

The multirotor model can be further enhanced by including additional effects such as feathering and tip losses. Perhaps the largest model improvement would be gained by further studies of how the total drag on the multirotor is affected by the interaction between the rotors and the airframe. This should realistically be made after a design concept has been chosen. Alternatively if a better estimation of the possible flight time is desired, a more detailed model of the battery would be needed.

Only the cascaded PID controller, which is probably not the most suitable for rejection of demanding disturbances and nonlinearities, has been covered in thesis work. Therefore it is recommended that an in-depth study of different control algorithms such as backstepping,  $\mathcal{L}_1$ -adaptive control, quaternion based control or feedback linearization is conducted. The proposed multirotor model would provide a suitable test platform for such an evaluation. It would also be interesting to investigate the possibilities of an online estimation of the drag and thrust coefficients, and the effects this would have on the wind resistance.

Another approach would be to further investigate the influence of propeller parameters such as blade twist and chord distribution. Optimizing the geometry of a propeller is no easy task. It gets even more complex when structural properties such as vibrations, which has been ignored during this report despite the evident effects it has on multirotor performance, are considered.

Moving forward with a multirotor design suitable for aiding in search and rescue missions, there are several implementation aspects worth considering for further project work. For instance, it would be interesting to model and evaluate the proposed Y6 multirotor with the added feature of servo-tiltable rotors. Also of high interest toward these applications would be the integration and control of an on-board thermal camera, attached to a motorized gimbal joint.

# Bibliography

- [1] *Aerospace; concepts, quantities and symbols for flight dynamics; aircraft motion relative to the air; ISO 1151-1:1988 modified*. Deutsches Institut für Normung, Berlin, Germany, 1990.
- [2] M. Bangura and R. Mahoney. “Nonlinear dynamic modeling for high performance control of a quadrotor, 3-5 december 2012”. In: *Australasian Conference on Robotics and Automation*. Victoria University of Wellington, New Zealand.
- [3] S. Bouabdallah. *Design and Control of Quadrotors with Application to Autonomous Flying*. Ecole Polytechnique Federale de Lausanne, Lausanne, Switzerland, 2007.
- [4] J. Brandt and M. Selig. *UIUC Propeller Database*. <http://aerospace.illinois.edu/m-selig/props/propDB.html>. Accessed: 2014-04-06.
- [5] J. B. Brandt and M. S. Selig. “Propeller performance data at low reynolds numbers”. In: *49th AIAA Aerospace Sciences Meeting, 4-7 January 2011*. Orlando, Florida, USA.
- [6] T. Bresciani. *Modelling, Identification and Control of a Quadrotor Helicopter*. Department of Automatic Control, Lund University, Lund, Sweden, 2008.
- [7] C. P. Coleman. *NASA Technical Paper 3675: A Survey of Theoretical and Experimental Coaxial Rotor Aerodynamic Research*. National Aeronautics and Space Administration (NASA), Moffett Field, California, USA, 1997.
- [8] M. J. Cutler. *Design and Control of an Autonomous Variable-Pitch Quadrotor Helicopter*. Department of Aeronautics and Astronautics, Massachusetts Institute of Technology, Boston, Massachusetts, USA, 2012.
- [9] S. Driessens and P. E. I. Pounds. “Towards a more efficient quadrotor configuration”. In: *2013 IEEE/RSJ International Conference on Intelligent Robots and Systems (IROS), 3-7 November 2013*. Tokyo, Japan.

- [10] G. J. J. Ducard and M.-D. Hua. "Discussion and practical aspects on control allocation for a multi-rotor helicopter". In: *Conference on Unmanned Aerial Vehicle in Geomatics (UAV-g 2011)*, 14-16 September 2011. ETH, Zürich, Switzerland.
- [11] L. Eriksson, E. Johansson, N. Kettaneh-Wold, C. Wikström, and S. Wold. *Design of Experiments*. 3rd ed. Umetrics Academy, Umeå, Sweden, 2008.
- [12] ESTECO. *Modefrontier*.  
<http://www.esteco.com/modelfrontier>.  
 Accessed: 2014-06-16.
- [13] J. Fogelberg. *Navigation and Autonomous Control of a Hexacopter in Indoor Environments*. Department of Automatic Control, Lund University, Lund, Sweden, 2013.
- [14] E. Fresk and G. Nikolakopoulos. "Full quaternion based attitude control for a quadrotor". In: *European Control Conference (ECC)*, 17-19 July 2006. Zürich, Switzerland.
- [15] T. Glad and L. Ljung. *Reglerteori - Flervariabla och olinjära metoder*. 2nd ed. Studentlitteratur AB, Lund, Sweden, 2011.
- [16] D. A. Griffiths and J. G. Leishman. "A study of dual-rotor interference and ground effect using a free-vortex wake model". In: *58th Annual Forum and Technology Display of the American Helicopter Society International*, 11-13 June 2002. Montréal, Quebec, Canada.
- [17] C. Y. E. Inc. *Stingray 500*.  
<http://curtisyoungbloodhobbies.curtisyoungblood.com/Stingray-500-Airframe-ND-YS5-K4001-9712.htm>.  
 Accessed: 2014-06-20.
- [18] N. Kau. *APC 10x4.7 Propeller CAD model*.  
<http://whenrobotsfly.tumblr.com/>.  
 Accessed: 2014-04-21.
- [19] J. G. Leishman. *Principles of Helicopter Aerodynamics*. 2nd ed. Cambridge University Press, New York City, New York, USA, 2002.
- [20] J. G. Leishman and S. Ananthan. "Aerodynamic optimization of a coaxial prorotor". In: *62th Annual Forum and Technology Display of the American Helicopter Society International*, 9-11 May 2006. Phoenix, Arizona, USA.
- [21] V. Martínez. *Modelling of the Flight Dynamics of a Quadrotor Helicopter*. Department of Aerospace Sciences, Cranfield University, Cranfield, Bedfordshire, United Kingdom, 2007.
- [22] P. Marwedel. *Pareto Points - Lecture slides*.  
 Accessed: 2014-06-05.

- [23] Mathworks. *Aerospace wind model*.  
<http://www.mathworks.se/help/aeroblks/wind.html>.  
Accessed: 2014-05-15.
- [24] Mathworks. *MATLAB Simulink*.  
<http://www.mathworks.se/products/simulink>.  
Accessed: 2014-06-16.
- [25] Advanced precision composites. *Model airplane propellers*.  
<http://www.apcprop.com/v/index.html>.  
Accessed: 2014-05-23.
- [26] Svenska Dagbladet. *Polisen vill använda drönare*.  
[http://www.svd.se/nyheter/inrikes/polisen-vill-anvanda-dronare\\_3571454.svd](http://www.svd.se/nyheter/inrikes/polisen-vill-anvanda-dronare_3571454.svd).  
Accessed: 2014-06-25.
- [27] Sydsvenska Dagbladet. *Polisen vill ha spionplan*.  
<http://www.sydsvenskan.se/skane/polisen-vill-ha-spionplan/>.  
Accessed: 2014-06-25.
- [28] Modde. *Modde - Design of Experiments*.  
<http://www.umetrics.com/products/modde>.  
Accessed: 2014-06-16.
- [29] J. R. Movellan. *DC Motors*. Machine Perception Laboratory, University of California, San Diego, California, USA, 2010.
- [30] NIST/SEMATECH. *E-handbook of statistical methods*.  
<http://www.itl.nist.gov/div898/handbook>.  
Accessed: 2014-06-02.
- [31] N. Ohlsson and M. Ståhl. *Model-Based Approach to Computer Vision and Automatic Control using Matlab Simulink for an Autonomous Indoor Multirotor System*. Department of Signals and Systems, Chalmers University of Technology, Gothenburg, Sweden, 2013.
- [32] P. Pounds, R. Mahoney, and P. Corke. “Modelling and control of a quadrotor robot”. In: *Australasian Conference on Robotics and Automation*, 6-8 December 2006. Auckland, New Zealand.
- [33] P. E. I. Pounds. *Design, Construction and Control of a Large Quadrotor Micro Air Vehicle*. Australian National University, Canberra, Australia, 2007.
- [34] J. Praceus. *Modellering av vind och turbulens för en High-Fidelity flygsimuleringsmodell*. Department of Automatic Control, Lund University, Lund, Sweden, 2013.
- [35] R. W. Prouty. *Helicopter Performance, Stability and Control*. Reprint edition with corrections. Krieger, Malabar, Florida, USA, 1990.
- [36] M. Rutkowski and W. Kruszi. *Design and analysis of ducted fan for multirotor VTOL UAV*. Polytechnika Gdansk, 2013.

- [37] M. Ryll, H. H. Bülthoff, and P. R. Giordano. *First Flight Tests for a Quadrotor UAV with Tilting Propellers*. Max Planck Institute for Biological Cybernetics, Tübingen, Germany, 2013.
- [38] K.-E. Årzén. *Real-Time Control Systems*. 2012 edition. Department of Automatic Control, Lund University, Lund, Sweden, 2012.
- [39] R. F. Stengel. *Aircraft Flight Dynamics MAE331 - Lecture slides*. <http://www.princeton.edu/~stengel/MAE331Lectures.html>. Accessed: 2014-02-25.
- [40] D. Systèmes. *Solidworks*. <http://www.solidworks.com/>. Accessed: 2014-06-16.
- [41] C. Technology. *Cyberquad*. <http://www.cybertechuav.com.au/>. Accessed: 2014-06-20.
- [42] The Engineering Toolbox. *Drag Coefficient*. [http://www.engineeringtoolbox.com/drag-coefficient-d\\_627.html](http://www.engineeringtoolbox.com/drag-coefficient-d_627.html). Accessed: 2014-06-02.
- [43] *Transportstyrelsens föreskrifter om obemannade luftfartyg (UAS) TSFS 2009:88*. Transportstyrelsen, Norrköping, Sweden, 2009.
- [44] K. Ulrich and S. Eppinger. *Product Design and Development*. 5th ed. McGraw-Hill/Irwin, New York City, New York, USA, 2012.
- [45] *U.S. Standard Atmosphere 1976*. National Aeronautics and Space Administration (NASA), Washington D.C., USA, 1976.
- [46] Q.-G. Wang, Z. Zhang, K. J. Åström, Y. Zhang, and Y. Zhang. “Guaranteed dominant pole placement with pid controllers”. In: *17th World Congress of the International Federation of Automatic Control, 6-11 July 2008*. Seoul, South Korea.

# A

## 6-DoF Kinematics

A rigid body mechanical systems, such as the flying multirotor, is typically described by motion with six degrees of freedom. These include translational motion along each coordinate axis as well as rotation around each of these axes. To simplify the system description, a body fixed coordinate system is often used where the coordinate axes follow the orientation of the body. Usage of such a coordinate frame is convenient in flight applications due to that applied forces and moments as well as sensor readings often are defined in relation to the vehicle orientation. Also, with the body frame origin placed in the center of gravity, the moment of inertia does not change with the orientation of the body.

A convenient way of transforming between body and inertial system descriptions is the application of rotation transformation matrices. In this section, these will be derived according to flight dynamics theory according to Robert F. Stengel [39]. In the simulator, the MATLAB toolbox SimMechanics has been employed to handle these transformations, but will nonetheless be described here.

Rotation angles around a set of axes are known as Euler angles. When studying flight dynamics, the angles  $\phi$ ,  $\theta$  and  $\psi$  are often referred to as roll, pitch and yaw angles, which represent the angle rotated around the  $x$ ,  $y$  and  $z$  axes respectively. These angles are used to transform between the inertial (I) and body frame (B) descriptions through a series of transformations, visiting two intermediate coordinate systems, (1) and (2). Step by step transformation for each rotation angle is described by the matrices in (A.1).

$$\begin{aligned} \mathbf{H}_1^1(\psi) &= \begin{bmatrix} \cos \psi & \sin \psi & 0 \\ -\sin \psi & \cos \psi & 0 \\ 0 & 0 & 1 \end{bmatrix} & \mathbf{H}_1^2(\theta) &= \begin{bmatrix} \cos \theta & 0 & -\sin \theta \\ 0 & 1 & 0 \\ \sin \theta & 0 & \cos \theta \end{bmatrix} \\ \mathbf{H}_2^B(\phi) &= \begin{bmatrix} 1 & 0 & 0 \\ 0 & \cos \phi & \sin \phi \\ 0 & -\sin \phi & \cos \phi \end{bmatrix} \end{aligned} \tag{A.1}$$



Combining each rotation, (A.1) yields the *direction cosine matrix* (DCM) (A.2), which transforms translational velocities and accelerations from the inertial frame to the body frame. The inverse of the DCM describes the transformation in the opposite direction. Because of the orthogonality of the DCM,  $(\mathbf{H}_1^B)^{-1} = (\mathbf{H}_1^B)^T$ .

$$\mathbf{H}_1^B(\phi, \theta, \psi) = \mathbf{H}_1^1 \mathbf{H}_1^2 \mathbf{H}_2^B = \quad (\text{A.2})$$

$$\begin{bmatrix} \cos \theta \cos \psi & \sin \phi \sin \theta \cos \psi - \sin \psi \cos \phi & \cos \phi \sin \theta \cos \psi + \sin \phi \sin \psi \\ \cos \theta \sin \psi & \sin \phi \sin \theta \sin \psi + \cos \phi \cos \psi & \cos \phi \sin \theta \sin \psi - \sin \phi \cos \psi \\ -\sin \theta & \sin \phi \cos \theta & \cos \phi \cos \theta \end{bmatrix}$$

To obtain a similar transformation for the rotational velocities and accelerations, the matrix formula in (A.3) is used, where  $p$ ,  $q$  and  $r$  are the rotational velocities around each of the body frame axes.

$$\begin{bmatrix} p \\ q \\ r \end{bmatrix} = \mathbf{I}_{3 \times 3} \begin{bmatrix} \dot{\phi} \\ 0 \\ 0 \end{bmatrix} + \mathbf{H}_2^B \begin{bmatrix} 0 \\ \dot{\theta} \\ 0 \end{bmatrix} + \mathbf{H}_2^B \mathbf{H}_1^2 \begin{bmatrix} 0 \\ 0 \\ \dot{\psi} \end{bmatrix} \quad (\text{A.3})$$

Rewriting (A.3), the transformation matrix  $\mathbf{L}_B^I$  (A.4) is obtained to transform rotational motion from the body to the inertial frame. Again, the inverse can be used to reverse the transformation, going from the inertial frame to the body frame coordinate systems. However, note that  $\mathbf{L}_B^I$  is not orthogonal.

$$\mathbf{L}_B^I(\phi, \theta, \psi) = \begin{bmatrix} 1 & \sin \phi \tan \theta & \cos \phi \tan \theta \\ 0 & \cos \phi & -\sin \phi \\ 0 & \sin \phi / \cos \theta & \cos \phi / \cos \theta \end{bmatrix} \quad (\text{A.4})$$

As seen in (A.4), the matrix  $\mathbf{L}_B^I$  becomes singular for angles  $\theta = \pm\pi/2$ . At these pitch angles, the transformation becomes undefined. Making use of a quaternion angle representation provides a remedy for this. However, further research into quaternions were not deemed necessary by the authors since such aggressive flight maneuvers are neither desired nor anticipated. Modeling and control with quaternions has, however, been performed by Fresk [14] with promising results.

# B

## Geometric and inertia calculations

Calculation of geometric dimensions and mass properties of the modeled multirotor UAV is the main topic of this appendix chapter. This is necessary to evaluate the relative influence of quantities such as total mass, moment of inertia and projected surface area of different multirotor setups in the simulator.

The main components of the simulated multirotor, summarized in Table B.1, are well described by two fundamental shapes for the airframe along with the propeller. These are the cylinder and the rectangular cuboid, for which standardized formulas exist to obtain the inertia and geometric properties. Using a rectangular cuboid and a cylinder, the arm geometry can be approximated. A pure cylinder shape represents the center, motors and propeller shafts. In addition to this, propellers modeled with CAD have been imported along with their geometric and inertia properties.

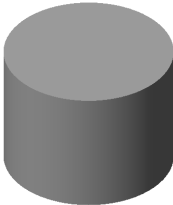
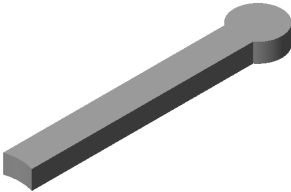

Cylinder	Arm	Propeller
		
Center, motor and shaft shapes.	Approximated to a rectangular cuboid and a cylinder in calculations.	Propeller properties are imported from a CAD model.

Table B.1: List of components.

## B.1 Mass

The combined mass of each part of the UAV add up to the total mass. The total mass  $m_{tot}$  of a multirotor configuration with  $n_a$  arms and  $n_r$  rotors is calculated by using Equation (B.1) below.

$$m_{tot} = m_c + n_a m_a + n_r m_m + n_r m_s + n_r m_p \quad (\text{B.1})$$

The symmetrical design of the multirotor aircrafts in this thesis means that the location of the center of gravity  $G$  will only vary vertically in the body frame. For arms attached to the middle of the cylindrical center part, the vertical location of the center of gravity is given by expression (B.2). Note that the distances to each part is measured from the middle of the center part to the part's local center of gravity.

$$G = \frac{1}{m_{tot}} n_r \left[ m_m \left( \frac{z_a}{2} + \frac{z_m}{2} \right) + m_s \left( \frac{z_a}{2} + z_m + \frac{z_s}{2} \right) + m_p \left( \frac{z_a}{2} + z_m + z_s \right) \right] \quad (\text{B.2})$$

## B.2 Moment of inertia

A body's moment of inertia describes the relation between angular acceleration and applied moment around a given axis. This relationship is given by (B.3), where  $\tau$  is the applied moment,  $\dot{\omega}$  the angular acceleration and  $I$  the moment of inertia. Hence, moment of inertia plays the same role for rotational motion as mass does for translational.

$$\tau = I \dot{\omega} \quad (\text{B.3})$$

However, calculating the moment of inertia is generally more cumbersome than mass. For an arbitrary body rotating around a given axis, the moment of inertia  $I$  is given by (B.4). In this equation,  $\rho$  is the body's density,  $\mathbf{r}$  a vector from the rotational axis to a point in the body and  $V$  the body's volume. Note that the  $\rho$  used here is not the air density.

$$\int_V \rho(\mathbf{r}) \mathbf{r}^2 dV \quad (\text{B.4})$$

For a three-dimensional body defined in a coordinate system with  $x$ -,  $y$ - and  $z$ -axes, the moment of inertia takes the form of a matrix called the *Inertia tensor* defined as (B.5). The tensor fully describes the rotational properties of a body rotating around any axis defined in the coordinate system. It is a symmetric matrix, which means that opposing terms mirrored in the diagonal are equal to each other (for instance  $I_{xy} = I_{yx}$ ). Using the inertia tensor, the relationship between a three-dimensional applied moment and angular acceleration is given by  $\tau = \mathbf{I}\dot{\omega}$ .

$$\mathbf{I} = \begin{bmatrix} I_{xx} & I_{xy} & I_{xz} \\ I_{yx} & I_{yy} & I_{yz} \\ I_{zx} & I_{zy} & I_{zz} \end{bmatrix} \quad (\text{B.5})$$

Since the multirotors studied in this thesis are of symmetric design, their arms are only placed around the vertical axis in the body frame. To align a locally defined inertia tensor, rotated an angle  $\theta$  with respect to the global body frame axes, the transformation in (B.6) is performed. In the equation,  $\mathbf{I}_L$  is the aligned local inertia tensor, whereas  $\mathbf{I}_{LR}$  is the rotated local inertia tensor.

$$\mathbf{I}_L = \mathbf{T}\mathbf{I}_{LR}\mathbf{T}^T \quad \mathbf{T} = \begin{bmatrix} \cos \theta & \sin \theta & 0 \\ -\sin \theta & \cos \theta & 0 \\ 0 & 0 & 1 \end{bmatrix} \quad (\text{B.6})$$

The local moment of inertia tensors may be calculated for each component using the formulas in Table B.2. To calculate the total moment of inertia tensor for the global body frame, the local moment of inertia tensors for each part must first be rotated accordingly so that their axes are aligned with those of the global body frame. Then, by making use of the parallel axis theorem (B.7), the total moment of inertia tensor for the entire body can be obtained. In the theorem,  $d$  is the distance between the rotation axes and  $m$  the component mass.

$$I_O = I_L + md^2 \quad (\text{B.7})$$

### B.3 Geometry

The projected surface area is the area which is seen from the perspective of the incoming airflow. This can easily be calculated for its body frame  $x$ ,  $y$  and  $z$  directions using knowledge of its setup and component dimensions. Proceeding with the quadrotor case, the following expressions in (B.8) gives the projected surface areas

Cylinder	Cuboid
$I_{XX} = \frac{1}{12}m(3r^2 + h^2)$	$I_{XX} = \frac{1}{12}(h^2 + w^2)$
$I_{YY} = \frac{1}{12}m(3r^2 + h^2)$	$I_{YY} = \frac{1}{12}(h^2 + l^2)$
$I_{ZZ} = \frac{1}{2}mr^2$	$I_{ZZ} = \frac{1}{12}(w^2 + l^2)$

Table B.2: Shapes local moment of inertia.

in the three main directions. The exposed surface area will shift depending on the direction of the incoming airflow. A discussion of this is given in Section 2.4.

$$\begin{aligned}
 A_x = A_y &= 2r_ch_c + 2(l_a - r_c)h_a + 4r_mh_m + 4r_sh_s \\
 A_z &= \pi r_c^2 + 4(l_a - r_c)w_a + 4\pi r_m^2
 \end{aligned} \tag{B.8}$$

Airframe drag force will, as discussed in Section 2.4, act in the airframe centroid. The centroid can be viewed as a center of geometry with area spread out evenly around it. For an arbitrary polygon body surface, it is calculated using its corner points. For a polygon with  $k$  corner points  $\mathbf{x}_i$ ,  $i = 1, \dots, k$ , the centroid  $\mathbf{C}$  is calculated according to (B.9).

$$\mathbf{C} = \frac{1}{k} \sum_i^k \mathbf{x}_i \tag{B.9}$$

# C

## Aerodynamic theory

In this appendix chapter, derivation of aerodynamic rotor theory is given. Since the model discussed in Section 2.3 makes use of both momentum theory and blade element theory, they are both described at length in the following sections. Momentum theory provides a basis for rotor performance evaluation and is used to deduce the rotor inflow velocity in the proposed model. Blade element theory gives a finer description of rotor forces and moment for each blade section. Applying integration along each blade and for a full rotor revolution, a much more accurate rotor model is obtained.

### C.1 Momentum theory

Momentum theory provides a coarse prediction of rotor flight performance. It treats the flow of air through a rotor disk as a tube of incompressible fluid, without any external interaction or variations across each rotor segment. The airflow itself is considered to be one-dimensional, i.e. its properties only vary perpendicular to the rotor plane. The rotor disk is assumed infinitesimally thin with an infinite amount of propeller blades, over which a pressure difference exists. The rotor work, introduced by an applied moment around the rotational axis, leads to added kinetic energy in the rotor slipstream. Due to the resulting airflow, an upward thrust is achieved. The momentum theory derivations presented in this section are made according to Leishman [19] and leads to equations for thrust force, applied moment and power in hover, axial and forward flight.

#### Hover flight

The momentum theory model for hovering flight is described by Figure C.1. In the figure, the numbers 1 and 2 indicate cross section planes just above and below the rotor disk with area  $A$ . Between these planes, a pressure difference exists. The speed  $v_i$  is the airflow velocity induced by the rotor. Sufficiently "far" upstream, the cross section plane indicated by a 0 is regarded as a boundary where the rotor no longer has an effect on the air velocity. In hover, this will mean that the air velocity is zero,  $V_0 = 0$ , in this region. The  $\infty$  sign indicates the "far" wake plane, also known as the

*vena contracta*. This is where it is assumed that the flow is fully developed with velocity  $V_\infty = w$ . Note that since the rotor "tube" contracts below the rotor and that mass is conserved, the air velocity is increased below the rotor.

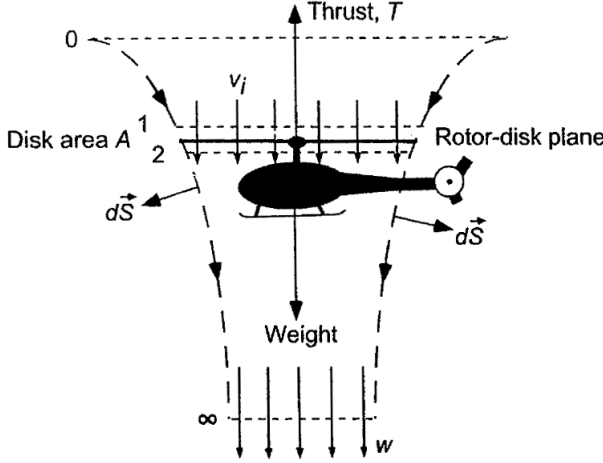


Figure C.1: Momentum theory for hovering flight [19].

Applying the principle of conservation of mass, the mass flow rate  $\dot{m}$  must be constant within the rotor wake. This yields Equation (C.1).

$$\dot{m} = \rho A_\infty w = \rho A v_i \quad (\text{C.1})$$

By using the principle of conservation of fluid momentum between the 0 and  $\infty$  planes, the resulting rotor thrust force  $T$  can be expressed as (C.2).

$$T = \dot{m} w \quad (\text{C.2})$$

Proceeding by applying conservation of energy between the 0 and  $\infty$  planes, the power  $P$ , i.e. work done per unit of time, is given by (C.3).

$$P = T v_i = \frac{1}{2} \dot{m} w^2 \quad (\text{C.3})$$

Combining the expressions (C.2) and (C.3), the relation  $w = 2v_i$  can be equated. Using this along with the mass flow (C.1), the expression for the rotor thrust and power can be re-written as  $T = 2\rho A v_i^2$  and  $P = 2\rho A v_i^3$ . Also, the contraction of the

rotor slipstream can be described by the relation  $A_\infty = \frac{1}{2}A$  between the rotor and the *vena contracta* areas.

The induced inflow velocity  $v_i$ , also denoted as  $v_h$  for hover, can be written as (C.4), where  $R$  is the rotor radius,  $\Omega$  the rotor rotational speed and  $\lambda_h$  is called the *induced inflow ratio* in hover. Again, using (C.4), the thrust, power and the applied rotor axis moment  $Q$  can be re-written as functions of  $\lambda_h$  and the rotor rotational speed  $\Omega$ . These expressions are shown in (C.5).

$$v_h \equiv v_i = \lambda_h \Omega R = \sqrt{\frac{T}{2\rho A}} \quad (\text{C.4})$$

$$T = 2\rho A \lambda_h^2 R^2 \Omega^2 \quad Q = 2\rho A \lambda_h^3 R^3 \Omega^2 \quad P = 2\rho A \lambda_h^3 R^3 \Omega^3 \quad (\text{C.5})$$

Introducing nondimensional coefficients to describe rotor thrust, applied moment and power is common practice in helicopter engineering and are defined according to (C.6). Note that since the applied moment  $Q$  and power are related as  $P = Q\Omega$ , their corresponding coefficients will have the same numerical values. Using the thrust coefficient  $C_T$ , the induced inflow ratio is described by  $\lambda_h = \sqrt{C_T}/2$  in hover.

$$C_T = \frac{T}{\rho A R^2 \Omega^2} \quad C_Q = \frac{Q}{\rho A R^3 \Omega^2} \quad C_P = \frac{P}{\rho A R^3 \Omega^3} \quad (\text{C.6})$$

## Axial flight

When modeling axial flight with MT, there are two subcases to consider — ascent and descent — where the net air flow has opposite directions. Starting with the ascent case, Figure C.2 describes the MT model. The situation is similar to that of hover, but with an added downward airflow speed resulting from the climb rate. As can be seen in the figure, the "far" upstream plane now has a flow speed relative to that of the ascending aircraft  $V_c$ , so  $V_0 = V_c$ . The flow speed at the rotor is  $v_i + V_c$  and at the vena contracta the slipstream speed is  $V_\infty = V_c + w$

Using the same procedure as for hover flight, the mass flow and resulting thrust and power can be calculated as (C.7). Note that the added terms for  $V_c$  cancel each other out for the thrust  $T$  at this stage, yielding the same thrust equation as for hover flight.



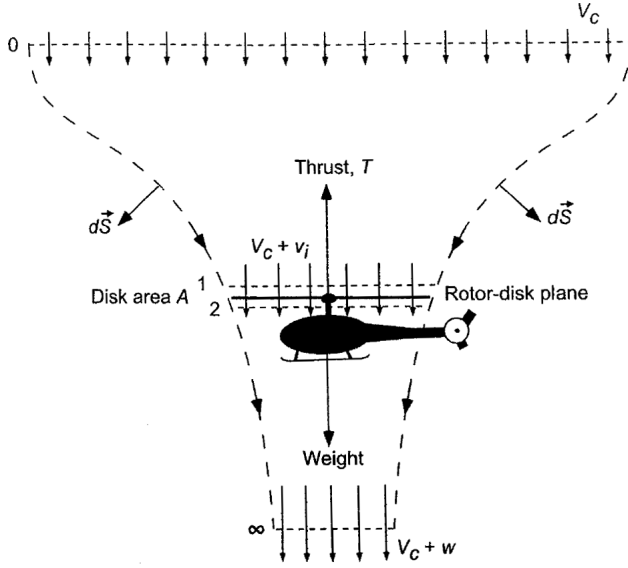


Figure C.2: Momentum theory for axial ascent flight [19].

$$\begin{aligned}
 \dot{m} &= \rho A_{\infty}(V_c + w) = \rho A(V_c + v_i) \\
 T &= \dot{m}(V_c + w) - \dot{m}V_c = \dot{m}w \\
 P &= T(V_c + v_i) = \frac{1}{2}\dot{m}(V_c + w)^2 - \frac{1}{2}\dot{m}V_c^2 = \frac{1}{2}\dot{m}w(2V_c + w)
 \end{aligned} \tag{C.7}$$

It is clear from (C.7) that  $w$  can again be calculated as  $w = 2v_i$ . This leads to that the thrust can be re-written as (C.8) for ascent flight.

$$T = \rho A(V_c + v_i)w = 2\rho A(V_c + v_i)v_i \tag{C.8}$$

Recalling the equation for  $v_h$  (C.4), inserting the ascent flight thrust equation (C.8) into (C.8) yields the quadratic expression  $v_h^2 = (V_c + v_i)v_i$  for the induced inflow velocity  $v_i$ . Hence, with prior knowledge of  $\lambda_h$ , MT can predict  $\lambda_i$  and  $v_i$  for ascent flight, making it possible to evaluate thrust, applied moment and power. Note that the positive solution of the quadratic function must be chosen.

For the descent axial flight case, the air is assumed to have a net flow in the upward direction. In Figure C.3, this is reflected by that the locations of the planes 0,  $\infty$ , 1 and 2 have been reversed.

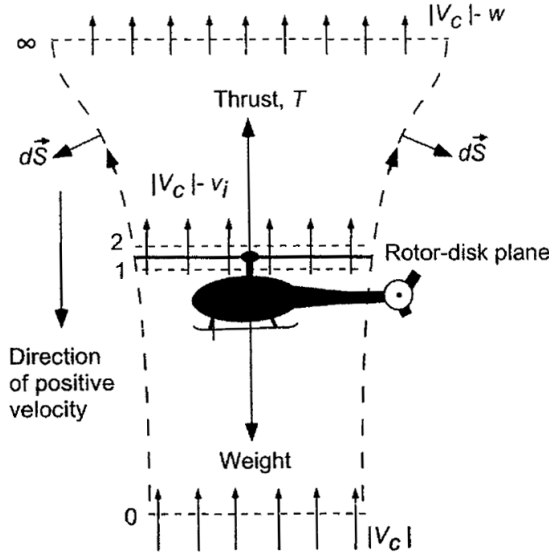


Figure C.3: Momentum theory for axial descent flight [19].

The mass flow  $\dot{m}$  is of the same magnitude as for ascent flight, but with a negative sign. In descent flight, the thrust  $T = -\dot{m}w$  will still be directed upwards, whereas the power  $P$  will be negative. This is the case since the rotor is now extracting power from the air, braking its speed as it passes the rotor disc. For this reason, the described flight condition is known as the *windmill brake state*.

The same method used to calculate the induced inflow ratio  $\lambda_i$  as for ascent flight can be applied for descent. The quadratic function  $v_h^2 = -(V_c + v_i)v_i$  is used, where the correct solution is the one that does not violate  $v_i/v_h > 1$ . The descent flight assumption that the net flow is directed upwards limits the MT model to a great extent. In the range  $-2v_h \leq V_c \leq 0$ , the flow can be either upward or downward, making the MT model invalid in this range of axial speed  $V_c$ .

## Forward flight

To achieve forward flight velocity, the rotor is tilted forward creating an angle of attack  $\alpha$  to the airflow. The flow model is described by Figure C.4, where it can be seen that the airflow has components both perpendicular and parallel to the rotor disk.

The air mass flow through the rotor is given by (C.9), where  $U$  is the resultant air flow speed at the rotor disk.

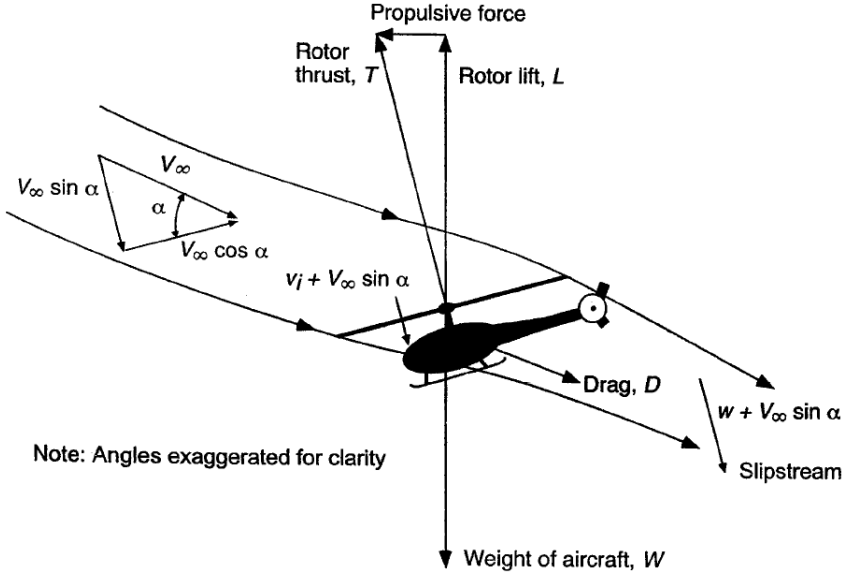


Figure C.4: Momentum theory for forward flight [19].

$$\dot{m} = \rho AU \quad U = \sqrt{(V_\infty \cos \alpha)^2 + (V_\infty \sin \alpha + v_i)^2} \quad (\text{C.9})$$

Applying the principle of conservation of momentum perpendicular to the rotor disk, the thrust  $T$  can be calculated as (C.10) for forward flight. Again, the thrust is described on the same form  $T = \dot{m}w$ , although with a different expression for  $\dot{m}$ .

$$T = \dot{m}(w + V_\infty \sin \alpha) - \dot{m}V_\infty \sin \alpha = \dot{m}w \quad (\text{C.10})$$

By yet again applying conservation of energy, the power can be expressed as C.11. As before, the power and thrust equations are used to obtain the relation  $w = 2v_i$ , which is the same for hover and axial flight.

$$P = T(v_i + V_\infty \sin \alpha) = \frac{1}{2} \dot{m}(2V_\infty w \sin \alpha + w^2) \quad (\text{C.11})$$

Proceeding with these findings, the thrust can finally be written as (C.12).

$$T = 2\rho A v_i \sqrt{(V_\infty \cos \alpha)^2 + (V_\infty \sin \alpha + v_i)^2} \quad (\text{C.12})$$

As in the axial flight case, the expression for the hover induced velocity  $v_h$  (C.4) is used to determine  $v_i$  for forward flight. Inserting the forward flight thrust equation (C.12) into (C.4),  $v_i$  can be expressed as (C.13).

$$v_i = \frac{v_h^2}{\sqrt{(V_\infty \cos \alpha)^2 + (V_\infty \sin \alpha + v_i)^2}} \quad (\text{C.13})$$

The advance ratio  $\mu$  is defined as the velocity parallel to the rotor disk,  $\mu = V_\infty \cos \alpha / (\Omega R)$ . Using this, the total inflow ratio  $\lambda$  can be expressed as (C.14), which includes the inflow induced by both the rotor and from the aircraft's relative airspeed.

$$\lambda = \frac{V_\infty \sin \alpha + v_i}{\Omega R} = \mu \tan \alpha + \lambda_i \quad (\text{C.14})$$

Using (C.13) and recalling  $\lambda_h = \sqrt{C_T/2}$ , the induced inflow ratio  $\lambda_i$  and the inflow ratio  $\lambda$  can be expressed as in (C.15).

$$\lambda_i = \frac{\lambda_h^2}{\sqrt{\mu^2 + \lambda^2}} = \frac{C_T}{2\sqrt{\mu^2 + \lambda^2}} \quad \lambda = \mu \tan \alpha + \frac{C_T}{2\sqrt{\mu^2 + \lambda^2}} \quad (\text{C.15})$$

The equations for  $\lambda_i$  and  $\lambda$  in (C.15) are applicable for all the flight modes where momentum theory is valid. They allow calculation of the MT predictions of thrust force, power and applied moment.

## C.2 Blade element theory

Blade element theory (BET) is a widely used method for calculating the aerodynamic forces and moments acting on a blade. BET assumes that each section of the blade is a quasi-2-D airfoil that produces aerodynamic forces and moments [19], which can be seen in Figure C.5. These infinitesimal forces and moments are then integrated over the length of the blade and averaged over one rotor revolution.

The infinitesimal lift force  $dL$  and the infinitesimal drag force  $dD$  is perpendicular and parallel to the local velocity resultant  $U$ . The expressions for these forces can be seen in Equation (C.16), where  $q = \frac{1}{2}\rho U^2$  is the dynamic pressure. In the equation,  $C_l$  and  $C_d$  are the local lift and drag coefficients while  $c dr$  is the reference area where  $c$  is the chord length.

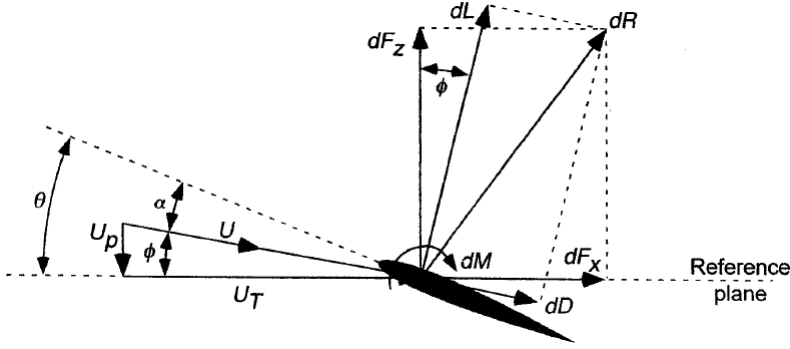


Figure C.5: Aerodynamic forces and moments acting at an infinitesimal blade element [19].

$$\begin{aligned} dL &= qC_l c dr \\ dD &= qC_d c dr \end{aligned} \quad (\text{C.16})$$

The determination of the moment  $dM$  around the aerodynamic center is neglected in this report because of the complexity, and since it was decided not to model the feathering motion.

A number of simplifications, listed below, are introduced to make the derivation of the aerodynamic forces and moments significantly easier.

- The local lift coefficient can be written as  $C_l = C_{l\alpha}(\theta - \phi)$  [19] where  $C_{l\alpha}$  can be approximated to  $2\pi$  according to the thin-airfoil theory.
- The local drag coefficient  $C_d$  is assumed to be constant and has been approximated in Section 2.3.
- The chord length is assumed to be constant.
- The pitch angle of the blade section is assumed to vary linearly along the length of the blade  $\theta = \theta_0 + \theta_{tw}r/R$
- The velocity component that is parallel to the reference plane  $U_T$  is assumed to be much bigger than the perpendicular component  $U_P$ . This leads to the following two simplifications:

1. The resulting velocity  $U = \sqrt{U_T^2 + U_P^2} \approx U_T$
2. The induced angle  $\phi = \arctan\left(\frac{U_P}{U_T}\right) \approx \frac{U_P}{U_T}$

By applying these simplifications, the following expressions (C.17) for the lift and drag forces are obtained.

$$\begin{aligned} dL &= \frac{1}{2} \rho c C_{l\alpha} \left( \left( \theta_0 + \theta_1 \frac{r}{R} \right) U_T^2 - U_P U_T \right) dr \\ dD &= \frac{1}{2} \rho U_T^2 c C_d dr \end{aligned} \quad (\text{C.17})$$

It is convenient to express the forces in the directions that are parallel and perpendicular to the hub plane. By once again using the simplification that the induced angle  $\phi$  is small and that the drag force is at least one magnitude smaller than the lift force, the following expressions (C.18) are obtained.

$$\begin{aligned} dF_z &= dL \cos \phi - dD \sin \phi \approx dL \\ dF_x &= dL \sin \phi - dD \cos \phi \approx \frac{U_P}{U_T} dL + dD \end{aligned} \quad (\text{C.18})$$

Multiplying the expressions in C.18 with the number of blades  $N_b$  yields the infinitesimal thrust, horizontal force and drag moment of the rotor (C.19).

$$\begin{aligned} dT &= N_b dF_z \\ dH &= N_b dF_x \\ dQ &= N_b y dF_x \end{aligned} \quad (\text{C.19})$$

In blade element theory, it is standard practice to introduce nondimensional coefficients according to (C.20), where the velocity components  $U_T$  and  $U_P$  are expressed in (C.21) [21].

$$\begin{aligned} dC_T &= \frac{dT}{\rho \pi R^4 \Omega^2} = \frac{N_b \frac{1}{2} \rho c C_{l\alpha} \left( \left( \theta_0 + \theta_1 \frac{r}{R} \right) U_T^2 - U_P U_T \right)}{\rho \pi R^4 \Omega^2} dr \\ dC_H &= \frac{dH}{\rho \pi R^4 \Omega^2} = \frac{N_b \left( \frac{U_P}{U_T} \frac{1}{2} \rho c C_{l\alpha} \left( \left( \theta_0 + \theta_1 \frac{r}{R} \right) U_T^2 - U_P U_T \right) + \frac{1}{2} \rho U_T^2 c C_d \right)}{\rho \pi R^4 \Omega^2} dr \\ dC_Q &= \frac{dQ}{\rho \pi R^5 \Omega^2} = \frac{N_b y \left( \frac{U_P}{U_T} \frac{1}{2} \rho c C_{l\alpha} \left( \left( \theta_0 + \theta_1 \frac{r}{R} \right) U_T^2 - U_P U_T \right) + \frac{1}{2} \rho U_T^2 c C_d \right)}{\rho \pi R^5 \Omega^2} dr \end{aligned} \quad (\text{C.20})$$

$$\begin{aligned}
U_T &= \Omega R \frac{r+e}{R} + \mu \sin \psi \\
U_P &= \Omega R \left( -\lambda_c - \lambda_i \left( 1 + K_c \frac{r}{R} \cos \Psi \right) - \frac{r}{R} (a_{1s} \sin \Psi - b_{1s} \cos \Psi) \right. \\
&\quad \left. - \mu (a_0 - a_{1s} \cos \Psi - b_{1s} \sin \Psi) \cos \Psi \right) + (r+e)(q_w \cos \Psi + p_w \sin \Psi)
\end{aligned} \tag{C.21}$$

The expressions in (C.21) include several variables which are listed below.

- $\lambda = \lambda_c + \lambda_i = \frac{V_\infty \sin \alpha + v_i}{\Omega R}$  is the inflow ratio.
- $\mu = \frac{V_\infty \cos \alpha}{\Omega R}$  is the advance ratio.
- $\alpha$  is the angle of attack of the rotor disk. Note that this is not the same angle of attack as the ones that each individual blade experiences.
- $V_\infty$  is the total magnitude of the free flow stream.
- $e$  is the hinge offset.
- $a_0$ ,  $a_{1s}$  and  $b_{1s}$  are angles that describe the blade flapping motion. The expressions for these angles are derived in Appendix C.3.

The aerodynamic coefficients are determined by integrating the expressions in Equation (C.20) over the length of the blade, i.e. from the root  $r_0$  to  $R$ . This integral is a function of the azimuth angle  $\Psi$  and the final result is calculated as the average value over a revolution. It is obtained by integrating over the azimuth angle from 0 to  $2\pi$  and dividing by the length of interval, resulting in Equation (C.22).

$$C_T = \frac{1}{2\pi} \int_0^{2\pi} \int_{r_0}^R dC_T d\Psi \quad C_H = \frac{1}{2\pi} \int_0^{2\pi} \int_{r_0}^R dC_H d\Psi \quad C_Q = \frac{1}{2\pi} \int_0^{2\pi} \int_{r_0}^R dC_Q d\Psi \tag{C.22}$$

Note that Prouty [35] assumes that the blade root  $r_0$  coincides with the hinge offset  $e$ . The same assumption has therefore been made in this report to avoid reformulation of the expressions. It has also been used that  $e \ll R$  to simplify the expressions

somewhat [21]. It is assumed that the rotational speed of the rotor is constant over the integrated revolution. This is true for conventional helicopters, but generally not for multirotors. However, testing has shown that the rotational speed change is typically less than 2 % during one revolution and the assumption is therefore considered to be reasonable. The final expressions for  $C_T$ ,  $C_H$  and  $C_Q$  can be seen in (C.23), where  $\sigma$  is the rotor solidity which is the total blade area divided by the disk area  $\sigma = N_b c R / \pi R^2 = N_b c / \pi R$ .

$$\begin{aligned}
 C_T &= \frac{C_{la}\sigma}{4} \left(1 - \frac{e}{R}\right) \left( \left(\frac{2}{3} + \mu^2\right) \theta_0 + \frac{1}{2}(1 + \mu^2) \theta_{tw} - \lambda \right) \\
 C_H &= \frac{C_{la}\sigma}{4} \left( \frac{C_d}{C_{la}} \mu - \frac{-\lambda + \mu a_{1s}}{1 + \frac{3}{2}\mu^2} \mu \left( \left(-\frac{1}{3} + \frac{3}{2}\mu^2\right) \theta_0 + \frac{1}{2} \left(-1 + \frac{3}{2}\mu^2\right) \theta_{tw} + \right. \right. \\
 &\quad \left. \left. \lambda - \mu a_{1s} \right) + \frac{\mu}{1 + \frac{1}{2}\mu^2} \left( \frac{a_0^2}{2} \left(\frac{1}{9} + \frac{\mu^2}{2}\right) + \frac{1}{3} \mu a_0 \lambda_i + \frac{1}{8} \lambda_i^2 \right) \right) \\
 C_Q &= \frac{C_{la}\sigma}{4} \left( \frac{1}{2} \frac{C_d}{C_{la}} (1 + \mu^2) - \frac{-\lambda + \mu a_{1s}}{1 + \frac{3}{2}\mu^2} \left( \frac{1}{3} (2 - \mu^2) \theta_0 + \frac{1}{2} \left(1 - \frac{\mu^2}{2}\right) \theta_{tw} + \right. \right. \\
 &\quad \left. \left. (-\lambda + \mu a_{1s}) (-\lambda + \mu a_{1s}) \right) - \frac{\mu^2}{1 + \frac{1}{2}\mu^2} \left( \frac{a_0^2}{2} \left(\frac{1}{9} + \frac{\mu^2}{2}\right) + \frac{1}{3} \mu a_0 \lambda_i + \frac{1}{8} \lambda_i^2 \right) \right)
 \end{aligned} \tag{C.23}$$

### C.3 Blade flapping

In forward flight, the rotor disk experiences an uneven lift distribution as the advancing and retreating blades experience different relative airspeeds. The advancing blade will generate additional lift whereas the retreating blade will generate less, resulting in a slight tilt of the rotor plane. This is known as blade flapping motion, where a blade's tilted angle will vary depending on its location around the propeller shaft. Even when not in forward flight, the blades undergoes a constant tilting known as coning. This effect is due to the lift force, which in axial flight is constant over a revolution, and hence doesn't tilt the rotor plane as a whole. The theory and mathematical modeling of this phenomena is well-described in the works of Leishman [19], Pounds [33] and Martínez [21], which have all inspired the blade flapping modeling performed in this thesis work.

As discussed in Section 2.3, a mechanical rotor model with an effective flapping hinge offset  $e$  and a torsional spring strength  $k_\beta$  is assumed. It is around this hinge offset that the balancing of forces and moments is calculated to deduce the flapping angle. The flapping angle  $\beta$  of a blade rotating around the shaft is calculated using a partial differential equation. The first-order solution to this equation, which is



sufficient to model the flapping behavior accurately, can be expressed as a function of the azimuthal angle  $\Psi$ , i.e. the blade position relative to the airflow, as (C.24). The variables  $a_{1s}$  and  $b_{1s}$  are the longitudinal and lateral flapping angles whereas  $a_0$  is the coning angle. These will be the angles of main interest when deducing the rotor tip path plane.

$$\beta = a_0 - a_{1s} \cos \Psi - b_{1s} \sin \Psi \quad (\text{C.24})$$

The three flapping angles,  $a_0$ ,  $a_{1s}$  and  $b_{1s}$ , are determined by balancing the lift force, centripetal force, gyroscopic moments and the weight of the propeller blades around the hinge offset  $e$ . Performing the balancing around the flapping hinge,  $a_0$ ,  $a_{1s}$  and  $b_{1s}$  may be calculated from (C.25).  $\mathbf{M}$ ,  $\mathbf{M}_{pq}$ ,  $\mathbf{F}$  and  $\mathbf{F}_{pq}$  are matrices containing expression for the various forces moments applied around the hinge listed in (C.27). The added gyroscopic terms  $\mathbf{M}_{pq}$  and  $\mathbf{F}_{pq}$  are added to account for the body's pitch and roll rotation.

$$(\mathbf{M} + \mathbf{M}_{pq}) \begin{bmatrix} a_0 \\ a_{1s} \\ b_{1s} \end{bmatrix} = \mathbf{F} + \mathbf{F}_{pq} \quad (\text{C.25})$$

The moments and forces matrices in (C.27) contain several variables that will be briefly explained here.

- $e$  is the effective blade hinge offset from the rotor shaft.
- $k_\beta$  is spring constant of the blade.
- $M_b$  is the moment due to weight force of the propeller.
- $I_{yb}$  blade moment of inertia around the flapping hinge.
- $\gamma = \frac{\rho C_l \alpha c R^4}{I_{yb}}$  is known as the Lock number.
- $p_w$  and  $q_w$  rotational velocities of the rotor around the rotor wind axes.

The effective hinge offset  $e$  was deduced in similar fashion to [21] and is shown in (C.26). The parameter  $r_0$  is the blade offset from the shaft joint, which was measured for the modeled propeller.

$$e = R \frac{\alpha_1 - 1}{\frac{M_b R}{g I_{yb}}} \quad \alpha_1 = 1.19 + 1.57 \frac{r_0}{R} \quad (\text{C.26})$$

$$\mathbf{M} = \begin{bmatrix} -\Omega^2 \left( I_{yb} + e \frac{M_b}{g} \right) - k_\beta & 0 & \frac{1}{2} \gamma_{yb} \Omega^2 \left( 1 - \frac{e}{R} \right)^2 \frac{\mu}{4} \frac{e}{R} \\ 0 & -\frac{1}{2} \gamma_{yb} \Omega^2 \left( 1 - \frac{e}{R} \right)^2 \left( \frac{1}{4} - \frac{\mu^2}{8} - \frac{1}{6} \frac{e}{R} - \frac{1}{12} \frac{e^2}{R^2} \right) & \Omega^2 e \frac{M_b}{g} + k_\beta \\ -\frac{1}{2} \gamma_{yb} \Omega^2 \left( 1 - \frac{e}{R} \right)^2 \left( \frac{1}{3} + \frac{1}{6} \frac{e}{R} \right) \mu & \Omega^2 e \frac{M_b}{g} + k_\beta & \frac{1}{2} \gamma_{yb} \Omega^2 \left( 1 - \frac{e}{R} \right)^2 \left( \frac{1}{4} - \frac{\mu^2}{8} - \frac{1}{6} \frac{e}{R} - \frac{1}{12} \frac{e^2}{R^2} \right) \end{bmatrix}$$

$$\mathbf{M}_{pq} = \begin{bmatrix} 0 & 0 & 0 \\ 0 & -\frac{1}{8} \gamma_{yb} \Omega^2 \left( 1 - \frac{e}{R} \right)^2 \left( 1 - \frac{\mu^2}{2} \right) & \Omega^2 e \frac{M_b}{g} + k_\beta \\ 0 & \Omega^2 e \frac{M_b}{g} + k_\beta & \frac{1}{8} \gamma_{yb} \Omega^2 \left( 1 - \frac{e}{R} \right)^2 \left( 1 - \frac{\mu^2}{2} \right) \end{bmatrix}$$

(C.27)

$$\mathbf{F} = \begin{bmatrix} -\frac{1}{2} \gamma_{yb} \Omega^2 \left( 1 - \frac{e}{R} \right)^2 \left( \frac{1}{4} \left( 1 + \mu^2 + \frac{2}{3} \frac{e}{R} \right) \theta_0 + \left( \frac{1}{5} + \frac{\mu^2}{6} \left( 1 - \frac{e}{R} \right) - \frac{1}{10} \frac{e}{R} - \frac{1}{15} \left( \frac{e}{R} \right)^2 - \frac{1}{30} \left( \frac{e}{R} \right)^3 \right) \theta_{tw} - \lambda \left( \frac{1}{3} + \frac{1}{6} \frac{e}{R} \right) \right) \\ -\frac{1}{2} \gamma_{yb} \Omega^2 \left( 1 - \frac{e}{R} \right)^2 \left( 2\mu \left( \frac{1}{3} + \frac{1}{6} \frac{e}{R} \right) \theta_0 + 2\mu \left( \frac{1}{4} - \frac{1}{6} \frac{e}{R} - \frac{1}{12} \left( \frac{e}{R} \right)^2 \right) \theta_{tw} - \frac{\mu}{2} \lambda \right) \\ 0 \end{bmatrix}$$

$$\mathbf{F}_{pq} = \begin{bmatrix} 0 \\ -\frac{1}{8} \gamma_{yb} \Omega^2 \left( 1 - \frac{e}{R} \right)^2 \frac{p_w}{R} + 2q_w \Omega I_{yb} \\ -\frac{1}{8} \gamma_{yb} \Omega^2 \left( 1 - \frac{e}{R} \right)^2 \frac{q_w}{R} + 2p_w \Omega I_{yb} \end{bmatrix}$$

## C.4 Coaxial rotors

Compared to a conventional single propeller rotor, there are some additional difficulties which has to be considered when a coaxial rotor is modeled. The lower rotor is affected by the induced inflow velocity generated by the upper rotor. This *downwash* will have a quite severe impact on the overall performance of the multirotor and it is therefore deemed necessary to include this phenomenon when modeling a coaxial rotor. The lower rotor will also affect the upper rotor, but this effect doesn't influence the overall performance as much [7] and will therefore be neglected in this report. The distance between the two propellers will not be considered either, since this distance only affects the distribution of the thrust between the two rotors according to Coleman [7].

The MT model for a coaxial rotor can be seen in Figure C.6. The slipstream of the upper propeller flows down through the inner part of the lower propeller. The slipstream typically contracts quickly (within  $0.25R$ ) according to Leishman [19] and Ananthan [20] and it is therefore assumed that the slipstream of the upper rotor is fully developed when it reaches the lower.

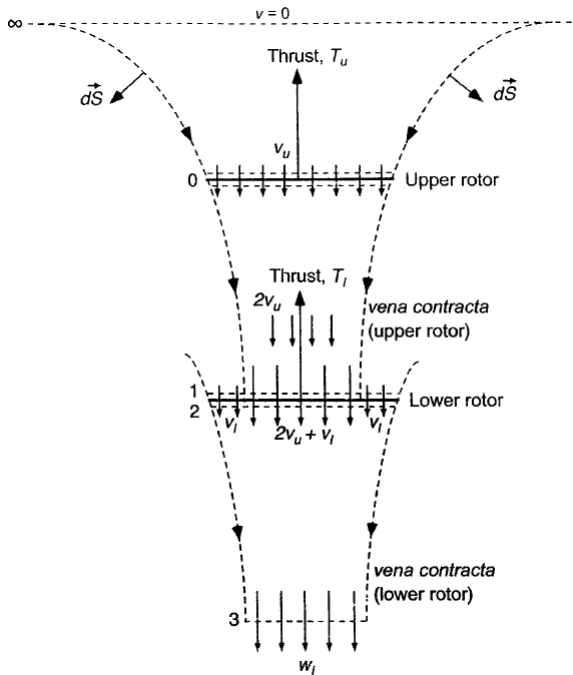


Figure C.6: Momentum theory model for a coaxial rotor in hover [19].

The contracted slipstream results in an uneven distribution of the inflow velocity across the lower rotor disk. To still be able to use the expressions in Equation (C.23), it was decided to use the ratio between the rotor disk area and the vena contracta area  $A_\infty = \frac{1}{2}A$ , which was described in C.1. By doing so it was possible to calculate an “average” inflow velocity according to Equation (C.28), where  $v_u$  and  $v_l$  are the induced velocities for the upper and lower rotor.

$$\dot{m} = \rho \frac{A}{2} (2v_u + v_l + V_c) + \rho \frac{A}{2} (v_l + V_c) = \rho A (v_u + v_l + V_c) \quad (\text{C.28})$$

The induced velocity of the upper rotor is therefore added to the inflow of the lower rotor while calculating the aerodynamic forces and moments. It should be noted that this is a simplification which had to be done because of the time constraints. The simplification will have some affect on the overall results, but the amount is hard to estimate. It was assumed that the error introduced by this simplification isn't any larger than those introduced by not modeling for example tip losses and feathering. It was also decided that an optimization of the performance of the coaxial rotor, where twist and chord length along the upper and lower blades are determined, would not be conducted.